Computational modeling of prefrontal cortex circuits

from neurons to networks

Jacinto José Fonseca Pereira

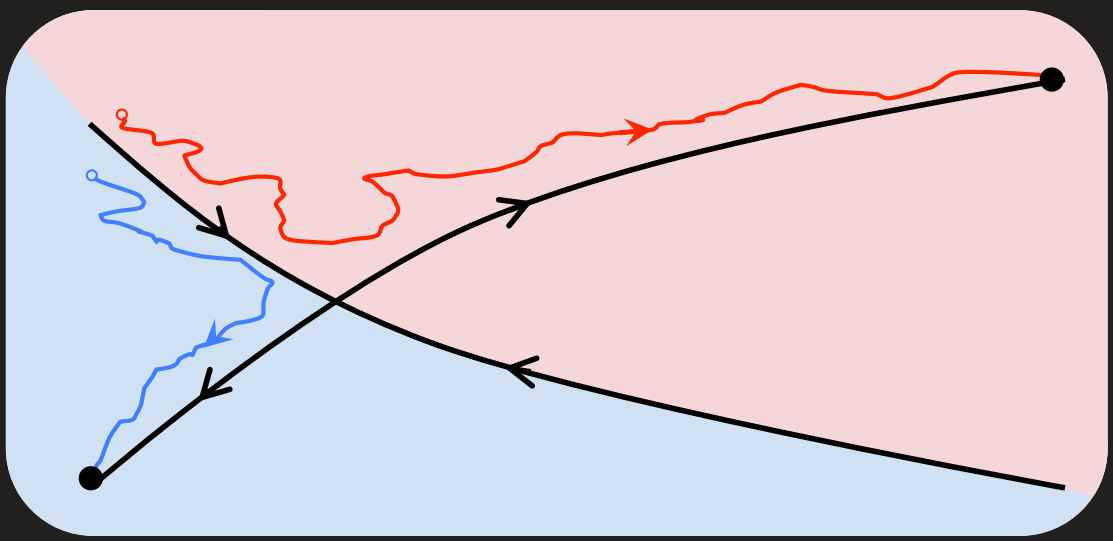

Dissertation presented to obtain the Ph.D degree in Biology

Instituto de Tecnologia Química e Biológica | Universidade Nova de Lisboa

Oeiras,
Jan, 2014

INSTITUTO
DE TECNOLOGIA
QUÍMICA E BIOLÓGICA
/UNL

Knowledge Creation

Computational modeling of prefrontal cortex circuits

from neurons to networks

Jacinto José Fonseca Pereira

Dissertation presented to obtain the Ph.D degree in Biology

Instituto de Tecnologia Química e Biológica | Universidade Nova de Lisboa

Research work coordinated by:

FUNDAÇÃO CALOUSTE GULBENKIAN
Instituto Gulbenkian de Ciência

Oeiras,
Jan, 2014

INSTITUTO
DE TECNOLOGIA
QUÍMICA E BIOLÓGICA
/UNL

Knowledge Creation

Computational modeling of prefrontal cortex circuits: from neurons to networks

A Dissertation Presented to
Instituto de Tecnologia Química e Biológica
Universidade Nova de Lisboa
to Obtain the Ph.D Degree in Biology

In Partial Fulfillment of the
Ph.D Program in Computational Biology
Instituto Gulbenkian de Ciência
Prof. José Pereira Leal, co-Advisor

With Scientific Work Developed at
Department of Neurobiology
Yale University School of Medicine
Prof. Xiao-Jing Wang, Advisor

by
Jacinto José Fonseca Pereira

January, 2014

The Preparation of this Dissertation was
Supported by:

PhD Program in Computational Biology

FUNDAÇÃO CALOUSTE GULBENKIAN

Instituto Gulbenkian de Ciência

Yale SCHOOL OF MEDICINE

FCT Fundação para a Ciência e a Tecnologia

MINISTÉRIO DA EDUCAÇÃO E CIÊNCIA

SFRH / BD / 32962 / 2006

NIH National Institutes of Health

Acknowledgements

I leave a note of appreciation to:
My advisor Xiao-Jing Wang for being an inspiration
and a model of scientific integrity;
My collaborators Amy Arnsten, Min Wang and David McCormick,
for challenging me with new ideas and for the overall great science;
All members of the Wang lab, past and present, for creating a
good work environment, especially Alireza Soltani,
Moran Furman, Alberto Bernacchia, Salva Ardid and my
semi-office-mate John Murray;
All my US and expat friends, especially
Catarina Nogueira, Sofia Fertuzinhos and Jon Arellano;
The "New Haven bike crew".
E agradecimentos igualmente para:
A organização do PDBC, em particular
Jorge Carneiro, Marie-France Sagot
e o meu co-orientador José Leal;
Os meus amigos em Portugal e pelo mundo fora;

Toda a minha família (alargada) que me recebe de braços abertos quando estou com eles e me faz sempre sentir "da casa";
As minhas manas, que me incentivaram a pesquisar desde pequeno o significado de conceitos abstractos (jibi).
Um muito obrigado aos meus pais Mário e Teresa, por me terem dado tudo o que sou e serem os melhores exemplos de vida a dois.
E finalmente um agradecimento especial para a Mafalda, a minha companheira desta aventura que é a vida. Se "cada um tem aquilo que merece", eu sou muita bom!

Abstract

The most outstanding feature of the human brain is its ability to perform highly complex cognitive tasks and one key region of the brain involved in these elaborated tasks is the prefrontal cortex. However, little is known about the basic neuronal processes that sustain these capacities. This dissertation describes the computational study of the biophysical properties of neurons in the prefrontal cortex that underlie complex cognitive processes with special emphasis in working memory, the ability to keep information online in the brain for a short period of time while processing incoming external stimuli. The goal of this study is to link basic mechanisms occurring at the cellular level with the activity of the neuronal network that generates the memory trace, and ultimately to understand the mechanisms underlying working memory function.

The current models built to simulate working memory are susceptible to drifts in the memory representation that contribute to deviate it from the original stimulus properties. To improve the stability of the working memory trace, we investigated three slow biophysical mechanisms that are activity-dependent and prominently present in neurons of the prefrontal cortex: depolarization-induced

suppression of inhibition, calcium-dependent nonspecific cationic current and short-term facilitation. We found that these processes on one hand enhance the memory accuracy by counteracting the impact created by noise on the mnemonic representation. On the other hand, they make it harder to erase a memory trace with short transient inputs. We characterize this trade-off between accuracy and flexibility and suggest that it can be adjusted according to behavioral demands.

The second part of this dissertation describes how the nonselective hyperpolarized-activated H-current (I_H) modulates prefrontal cortex functions. The pharmacological blockage of I_H in the prefrontal cortex has been reported to augment neural firing in pyramidal cells, induce stronger persistent activity of the network and improve working memory task performance. Additional studies in vitro have shown a similar increase in excitability when an I_H antagonist was applied to cortical slice preparations. We modeled these results in single cell compartment models and found that I_H alone could not account for these changes. We proved that I_H is a mostly depolarizing current and its blockage leads to a decrease in the generation of action potentials.

Lastly, we provide two alternative hypotheses that could account for the experimental results of the blockage of I_H. First, I_H may interact with an outward, hyperpolarizing current that is mediated by channels that are sensitive to the I_H antagonist. Second, we propose that the presence of I_H in local interneurons promotes the generation of action potentials in these inhibitory cells, leading to a

decrease of activity in pyramidal cells. Conversely, the blockage of I_H results in a reduced excitability of interneurons and an increased activity of pyramidal cells.

Sumário

A característica mais extraordinária do cérebro humano é a sua capacidade para realizar tarefas cognitivas de elevada complexidade, e uma região do cérebro essencial nestas tarefas é o córtex pré-frontal. No entanto, pouco se sabe acerca dos processos neuronais básicos que sustentam estas faculdades mentais. Esta dissertação descreve o estudo computacional das propriedades biofísicas de neurónios do córtex pré-frontal que definem os processos cognitivos complexos, com especial ênfase na memória de trabalho, ou seja, a capacidade de guardar informação on-line no cérebro por um curto período de tempo enquanto se faz o processamento de estímulos externos. O objetivo deste estudo é fazer a ligação entre mecanismos básicos que ocorrem ao nível celular com a atividade da rede neuronal que produz o sinal da memória e, em úlima análise, compreender os mecanismos que sustentam a memória de trabalho.

Os modelos atuais construídos para simular a memória de trabalho são suscetíveis de sofrer desvios na representação da memória o que contribui para distanciá-la das propriedades iniciais do estímulo. Para melhorar a estabilidade do sinal da memória de trabalho, investigámos três mecanismos biofísicos lentos que são dependentes

de actividade e que estão presentes em neurónios do córtex pré-frontal: supressão de inibição dependente de despolarização, corrente catiónica não específica dependente de cálcio e facilitação de curta duração. Descobrimos que estes processos, por um lado aumentam a exactidão da memória, neutralizando o impacto criado por ruído na representação mnemónica. Por outro lado, tornam mais difícil apagar o sinal da memória com estímulos transitórios breves. Caracterizámos este compromisso entre exactidão e flexibilidade e sugerimos que ele pode ser ajustado de acordo com as exigências comportamentais.

A segunda parte desta dissertação descreve como a corrente H (I_H), que é ativada por hiperpolarização e é não-seletiva, modula as funções do córtex pré-frontal. Tem sido descrito que o bloqueio farmacológico da I_H no córtex pré-frontal aumenta o disparo neuronal em células piramidais, induz uma forte atividade persistente da rede e melhora o desempenho em tarefas que testam a memória de trabalho. Estudos adicionais in vitro demonstraram um semelhante aumento na excitabilidade celular quando um antagonista da I_H foi administrado a preparações de tecido cortical. Simulámos estes resultados em modelos compartimentais de células únicas e descobrimos que a I_H sozinha não pode ser responsável por essas mudanças. Provámos que a I_H é uma corrente maioritariamente despolarizante e que o seu bloqueio leva a uma diminuição da geração de potenciais de acção.

Por último, sugerimos duas hipóteses alternativas que poderão explicar os resultados experimentais do bloqueio da I_H. Em primeiro

lugar, a I_H pode interagir com uma corrente hiperpolarizante, que promove o fluxo de catiões para o exterior da célula e que é mediada por canais sensíveis ao antagonista da I_H. Em segundo lugar, propomos que a presença da I_H em interneurónios vizinhos promove a geração de potenciais de acção nestas células inibitórias, levando a uma diminuição da atividade nas células piramidais. Por outro lado, o bloqueio da I_H resulta numa excitabilidade reduzida dos interneurónios e um aumento da atividade das células piramidais.

Contents

List of Figures

Chapter 1

Introduction

The scientific study of the brain is one of the most challenging tasks currently faced by humanity. The nervous system is not only our gateway to the external world and social interactions but also underlies our internal state of mind, thoughts, decisions and memories. Such a multifaceted system requires a variety of investigative approaches in order to be fully comprehended. While that goal is still a distant prospect, several significant contributions have been made to the field of Neuroscience.

Like all other systems in living beings, the nervous system is framed by the expression of genes coded in the DNA. However neural function is only partially explained by genetics and the same could be said about physical and chemical interactions, cellular mechanisms, synaptic communication, circuit dynamics and behav-

ioral responses. Each of these dimensions can, and should, be studied separately to attain their detailed components and mechanisms. Nevertheless, a more complete understanding of neural processes may only be achieved through a cross-examination and integration of the different levels of abstraction.

Neural circuits dynamics have a more immediate relationship with cognition, in a sense that it is the output of networks of neurons that drive such functions as motor response, memory storage, learning and decision-making. Notwithstanding, low-level synaptic and cellular mechanisms determine the properties and behavior of each of those neurons and provide invaluable substrates for the manipulation of the brain activity and treatment of psychiatric disorders, as proven by many compounds currently used in medicine, such as fluoxetine, valproic acid and guanfacine.

The neural functions are performed by the interplay between several brain regions. The prefrontal cortex (PFC), in the anterior part of the frontal lobes, plays a crucial role in supervising higher cognitive functions (Fuster 1997; Miller and Cohen 2001). It is vastly connected to other anatomical regions, which allows it to integrate information from several brain sources and exert top-down control over most processes in the central nervous system. A distinct property of the neural circuits of the PFC is the capacity to maintain persistent neural activity for several seconds without direct stimulation (Fuster and Alexander 1971; Funahashi et al. 1989; Miller et al. 1996; Romo et al. 1999). This duration is much longer than the timescale of synaptic connections between neurons and

therefore, it has been proposed that persistent activity is sustained by slow reverberatory dynamics within a neural circuit (Hebb 1949; Amit 1995; Goldman-Rakic 1995; Wang 2001). Studies in monkeys found evidence of this type of circuit in the superficial layers of the dorsolateral PFC (Levitt et al. 1993; Kritzer and Goldman-Rakic 1995). The theoretical modeling of persistent activity suggested that the driving force behind it lies in recurrent synaptic excitation that depends on the N-methyl-d-aspartate (NMDA) receptors (Wang 1999b). This prediction has recently garnered direct support from experimental results obtained in primates (Wang et al. 2013).

Persistent activity in the PFC has been hypothesized to be the basis of working memory (Hebb 1949; Fuster and Alexander 1971; Miyashita and Chang 1988; Amit 1995; Goldman-Rakic 1995; Wang 2001), which is the active maintenance of information during periods of a few seconds in the absence of direct external inputs. Working memory allows a variety of information, such as sensory stimulus or internal thoughts, to be stored and retrieved during planning and execution of behavioral tasks (Miller 1960).

A well-known paradigm to study working memory is the oculomotor delayed-response (ODR) task. In this experiment, a subject is required to retain information of a visual cue location (directional angle) throughout a delay period between the stimulus and memory-guided behavioral response (Fig. 1.1A). In a version of this experiment, previously-implanted electrodes in the dorsolateral prefrontal cortex record the activity of single neurons while the subject is performing the task (Funahashi et al. 1989; Chafee and Goldman-

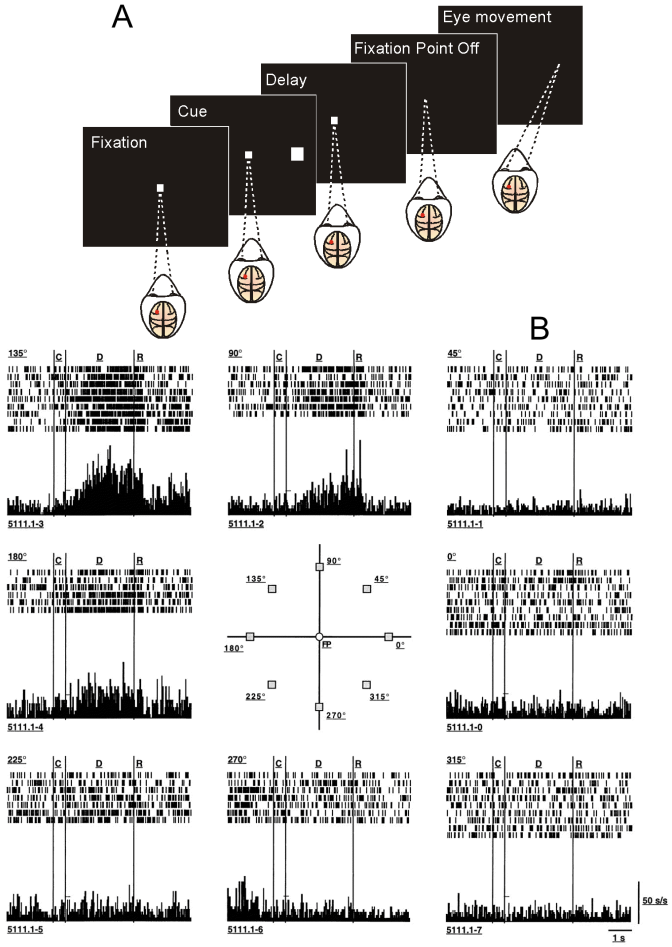

Figure 1.1. Sequence of events and neural responses in the oculomotor delayed-response task. **A**, trials begin with the appearance of a fixation point at the center of the screen, which the monkey is required to fixate throughout the trial. A spatial cue is subsequently presented, typically at one of eight locations (center diagram in **B**). After a delay period of a few seconds, the fixation point is turned off and the monkey is required to indicate the location of the cue by moving his eyes accordingly on the screen. **B**, directional delay period activity of a single PFC neuron during the oculomotor delayed-response task. The eight discharge patterns are arranged as to indicate the location of the cue. (Cont.)

Figure 1.1. (Cont.) This neuron exhibited the strongest directional delay period activity following presentation of the cue in the upper left quadrant (135 degrees). Adapted from Constantinidis and Wang (2004) and from Funahashi et al. (1989).

Rakic 1998; Constantinidis and Goldman-Rakic 2002; Constantinidis and Wang 2004). These recordings show that certain neurons produce high levels of persistent firing during the delay period only after the presentation of cues at a given angle (Fig. 1.1B). Assuming that different neurons are tuned to different locations, similarly to what happens in the primary visual cortex (Hubel and Wiesel 1968), it is believed that a circuit in the PFC is capable of representing the continuous 360 degree space.

Based on these observations, theoretical models of spatial working memory have been developed. A basic concept in some of these models is the representation of persistent activity as dynamical attractors (Amari 1977; Amit 1995; Wang 2001). The term attractor refers to a self-sustained and stable state of a dynamic system, such as a neural network (Wang 2013). A spatial working memory system can be either in the spontaneous state or in a continuum of location-selective memory states. Each of these states is considered an attractor and transitions between them can be achieved through transient inputs.

The theoretical simulation of working memory can take into account different levels of biophysical detail. The most basic properties incorporated in some models are the overall firing rates of populations of neurons (Amari 1977; Amit et al. 1994; Camperi

and Wang 1998; Durstewitz et al. 1999; Itskov et al. 2011). While these models can simulate the main input-output function of a circuit, they do not provide a clear link to physiological data. In order to unravel interdependencies between cellular properties and neural circuit dynamics, it is preferable to include more detailed biophysical properties and neural spiking dynamics (Amit and Brunel 1997; Durstewitz et al. 2000a; Compte et al. 2000; Tegnér et al. 2002; Renart et al. 2003; Machens et al. 2005; Carter and Wang 2007; Hansel and Mato 2013). These type of models, which are more relevant to the work described in this dissertation, allow the modeler to propose predictions that could be tested in electrophysiological experiments.

The model proposed by Compte et al. (2000) to simulate the ODR task has a population of excitatory pyramidal cells figuratively arranged in a ring-like fashion. Each of these neurons is selectively-tuned to a subsection of the 360-degrees space (like the neuron in Fig. 1.1B). A crucial feature is that neurons not only receive external inputs, but are also connected to each other with weights that are inversely dependent on their distance in the ring. When a cue at a certain angle is presented, the group of neurons tuned to that angle elevates their firing rates and stimulate each other reciprocally. This positive feedback through recurrent synaptic excitation is primarily mediated by NMDA receptors (Wang 1999b) and gives rise to a localized persistent activity, creating an attractor memory state. The overall activity of the network is kept from escalating uncontrollably through the nonspecific inhibition by a population

of GABAergic, inhibitory interneurons.

The hypothesis that explains working memory maintenance through states with stable activity is not consensual. A study proposed that persistent activity is a costly consumption of metabolical energy and is not required for working memory (Mongillo et al. 2008). According to their modeling analysis, neocortical networks encode and maintain information through slow calcium-mediated synaptic facilitation (Tsodyks and Markram 1997; Hempel et al. 2000). This mechanism consists in a state of increased neurotransmitter release that will allow the memory to be reactivated. However, this reactivation requires either an unrealistic readout stimulus or an artificial increase in the background input that effectively results in persistent activity. Another study proposed that memory maintenance relies on positive feedforward instead of feedback between neurons, even in anatomically recurrent networks (Goldman 2009). This idea can explain some experimental data observations but, on the other hand, the proof of its biological realism is still tenuous. Barak et al. (2013) recently compared three parametric working memory models of a delayed vibrotactile discrimination task. The models were comprised of neurons with different degrees of tuning and dynamics: ranging from a system with predetermined connectivity and stable neural representations (Machens et al. 2005) to a random network that evolves according to the readout. They found that an intermediate model was the one that best simulated the data at their disposal.

In this work, we employ a model that exhibits stable persistent

activity (in line with Compte et al. (2000)) because it relies on biophysically-realistic parameters, it can explain relevant electrophysiological data of working memory tasks, and allows to formulate testable predictions at both cellular and circuit level. We also analyze simpler models of pyramidal cells to determine more basic properties of these neurons. As a result, a recurring theme in this dissertation is the attempt to connect several levels of abstraction within the PFC.

Chapter 2 deals with the robustness of the above mentioned spatial working memory model. A characteristic of this type of networks, in its current state of description, is the accumulation of small deviations to the memory trace over time, which can result in a final memory representation that is distant from the original cue stimulus. The cellular and synaptic properties of these networks are mostly homogeneous. The presence of heterogeneous properties can disrupt the continuous family of attractors, i.e. the network is no longer able to encode all 360 degrees and quickly drifts to one of just a few privileged locations (Ben-Yishai et al. 1995; Tsodyks and Sejnowski 1995; Zhang 1996; Renart et al. 2003; Itskov et al. 2011). Finally, if a distractor signal is presented while the nework is encoding a previous stimulus, the remembered cue location may move towards the distractor. All these phenomena can have negative implications on the accuracy of the memory trace.

As stated before, the stability of the persistent activity during de delay period of working memory is sustained by slow reverberatory processes. But is the slower the better? To address

this question, we tested how three cellular and synaptic biophysical mechanisms affect the memory representation: short-term facilitation, depolarization-induced suppression of inhibition and calcium-activated inward currents. Briefly, short-term facilitation (STF) is the increase in neurotransmitter release and postsynaptic response after repetitive stimulation of a synapse (Tsodyks and Markram 1997; Hempel et al. 2000). Depolarization-induced suppression of inhibition (DSI) is a mechanisms that decreases the inhibition received by pyramidal cells when they are very active (Ohno-Shosaku et al. 2001; Wilson et al. 2001; Wilson and Nicoll 2001). A calcium-activated inward current (I_{CAN}) is independent of the membrane potential and depolarize cells after calcium influx. All three mechanisms were found in the PFC, are activity-dependent, provide positive feedback and operate under a slow time course of activation.

The incorporation of these mechanisms in the network increased the memory robustness and decreased the variability observed across trials. On the other hand, their slow nature resulted in costlier transitions between memory and resting state, which decreased the flexibility of the overall system. We were able to explain these observations through a detailed analysis of the network model.

The project described in chapter 3 was done in collaboration with experimentalists. One group carried out electrophysiological recordings in monkeys, who were performing ODR tasks. At the same time, they applied pharmacological compounds that block or activate receptors and cellular machinery in specific regions of the PFC of these monkeys. The results from these experiments allowed

them to associate aspects of the monkey behavior with firing activity of neurons and molecular pathways (Wang et al. 2007). A second group studied the modulation of slow oscillations by ionic currents (Shu et al. unpublished observations). Both studies observed that the blockage of the channels that mediate H-current (I_H) increases the excitability of pyramidal cells. This current is activated by hyperpolarized membrane potentials and is inward (depolarizing) at sub-threshold potentials. In order to understand the basic mechanism of I_H, we incorporated it in compartment neural models. We demonstrate that the inactivation of this current alone was not enough to produce the results observed with the pharmacological blocking of I_H channels in experiments. We also tested the properties of a second potassium current (I_M) in the single cell and working memory models.

Finally, in chapter 3 we propose two alternative hypotheses that can explain the effects of blocking the I_H channels. The first consists of the interplay of I_H with an outward (hyperpolarizing) current (Migliore and Migliore 2012). In the second, I_H is present not only in excitatory pyramidal cells as currently assumed, but also in inhibitory cells as reported in some studies (Maccaferri and McBain 1996; Kawaguchi and Kubota 1997; Lupica et al. 2001; Notomi and Shigemoto 2004; Aponte et al. 2006; Hughes et al. 2013). We demonstrate how these two hypotheses are compatible with the experimental procedures and observations.

A main goal of this work is to contribute for the understanding of working memory. The adopted research approach focus on find-

ing links between the cellular properties and the circuit dynamics relevant to this cognitive process.

Chapter 2

A trade-off between accuracy and flexibility in a working memory circuit endowed with slow feedback mechanisms

2.1 Abstract

Recent studies have led to the recognition that reverberation underlying mnemonic persistent activity must be slow, in order to ensure the stability of a working memory system and to give rise to long neural transients capable of accumulation of information over time. Is the slower the underlying process, the better? To address this question, we investigated three biophysical mechanisms operating on slow timescales, all are activity-dependent and prominently present in neurons of the prefrontal cortex: depolarization-induced suppression of inhibition (DSI), calcium-dependent non-specific cationic current (I_{CAN}) and short-term facilitation (STF). Using a spiking network model for spatial working memory, we found that these slow biophysical processes enhance the accuracy of memory representation by counteracting noise-induced drifts of a memory trace, heterogeneity-induced systematic loss of stored information and distractors. Furthermore, the incorporation of DSI and I_{CAN} enlarges the range of network's properties required for memory states. However, when a progressively slower process dominates the network, it becomes increasingly more difficult to erase a memory trace and reset the network by brief external inputs, which is required for proper function of a working memory circuit. We demonstrate this basic trade-off between accuracy and flexibility quantitatively and provide an explanation of it using a state-space analysis. Our results support the scenario in which the NMDA-receptor dependent recurrent excitation is the workhorse for the maintenance of persistent activity, whereas very slow synaptic or

cellular processes contribute to the robustness of mnemonic function in a trade-off that potentially can be adjusted according to behavioral demands.

2.2 Introduction

Working memory is thought to be represented by persistent activity (Fuster and Alexander 1971; Gnadt and Andersen 1988; Funahashi et al. 1989; Amit 1995; Goldman-Rakic 1995; Miller et al. 1996; Romo et al. 1999; Wang 2001; Major and Tank 2004). Such activity patterns are likely sustained by positive feedback processes in a neural circuit, but the precise mechanisms remain unresolved. Computational models stressed the role of recurrent synaptic excitation (Amit 1995; Camperi and Wang 1998; Amit and Brunel 1997; Brunel and Wang 2001; Durstewitz et al. 2000b) that depends on the NMDA receptors (Wang 1999b; Compte et al. 2000; Lim and Goldman 2013), a prediction supported by findings from a recent experiment (Wang et al. 2013).

Other synaptic and cellular process, present in the prefrontal cortex (PFC), are likely involved in mnemonic persistent activity, including short-term facilitation (STF) (Hempel et al. 2000; Wang et al. 2006; Mongillo et al. 2008; Szatmary and Izhikevich 2010; Hansel and Mato 2013), depolarization-induced suppression of inhibition (DSI) (Carter and Wang 2007) and calcium-activated inward currents (I_{CAN}) (Tegnér et al. 2002; Egorov et al. 2002; Fransén et al. 2006; Yoshida and Hasselmo 2009; Kulkarni et al. 2011; Kalmbach et al. 2013). STF and I_{CAN} provide feedback excitation, whereas DSI is a disinhibition process. All are activity-dependent, thus become selective for neurons that show elevated persistent activity. Furthermore, these mechanisms operate with biophysical time constants much slower than the NMDA receptor mediated

synaptic excitation. Therefore, the long-standing question (Major and Tank 2004) has gained urgency: what may be the relative contributions to working memory function of these slow synaptic and cellular processes versus the recurrent network mechanism?

We analyzed the role of slow biophysical processes in mnemonic persistent activity, using a biologically-based continuous spiking circuit model for spatial working memory. This model system is endowed with a resting state and a continuum of spatially tuned persistent activity patterns ("bump attractors") for memory storage of an analog quantity such as spatial location (Camperi and Wang 1998; Compte et al. 2000; Gutkin et al. 2001; Laing and Chow 2001; Renart et al. 2003; Carter and Wang 2007; Wei et al. 2012; Murray et al. 2012). During a mnemonic delay period, a bump attractor drifts over time (Compte et al. 2000; Carter and Wang 2007; Murray et al. 2012), resulting in random deviations of the memory away from the to-be-remembered sensory cue. Additionally, heterogeneity in single neurons disrupts the continuous family of attractors (Ben-Yishai et al. 1995; Tsodyks and Sejnowski 1995; Zhang 1996), leading to systematic drifts of memory trace (Renart et al. 2003; Itskov et al. 2011). Furthermore, the system may be perturbed by external distractor stimuli. Interestingly, we found that while STF, DSI and I_{CAN} enhance the accuracy of a memory trace, they hinder rapid memory erasure and network reset. The latter is not functionally desirable, since behavior demands that brief transient inputs should be sufficient to switch a working memory system from its resting state to a memory state or vice versa

(Compte et al. 2000; Gutkin et al. 2001). Therefore, our study reveals a fundamental trade-off between robustness and flexibility of working memory function instantiated by slow neurobiological mechanisms in a recurrent network.

2.3 Materials and Methods

In an oculomotor delayed-response (ODR) task, the sensory stimulus is a visual cue and the motor response is a saccade to the cued location. A subject is briefly shown a visual cue that must be remembered during a delay period of a few seconds. This memory is subsequently used to perform a memory-guided behavioral response (the saccade). During the delay period, many neurons in the dorsolateral PFC show high persistent activity that is spatially selective (Funahashi et al. 1989). The present work uses a spiking network model for the ODR task that has been tested thoroughly (Compte et al. 2000; Carter and Wang 2007; Wei et al. 2012; Murray et al. 2012). The parameters were modified starting with the original "control parameter set" in Compte et al. (2000). The model consists of a population of excitatory pyramidal cells and a population of inhibitory interneurons. Pyramidal cells are arranged in a ring-like fashion and labeled by their preferred cue direction, from 0 to 360 degrees. A schematic of the network structure is shown in Fig. 2.1A.

2.3.1 Single neuron model

Both pyramidal cells and interneurons are modeled as leaky integrate and fire units (Tuckwell 1988). Each type of cell is characterized by total capacitance C_m, total leak conductance g_L, leak reversal potential V_L, threshold potential V_{th}, reset potential V_{res} and refractory time τ_{ref}. The values that we use in the simulations

are $C_m = 0.5$ nF, $g_L = 25$ nS, $V_L = -70$ mV, $V_{th} = -50$ mV, $V_{res} = -60$ mV, and $\tau_{ref} = 2$ ms for pyramidal cells; and $C_m = 0.2$ nF, $g_L = 20$ nS, $V_L = -70$ mV, $V_{th} = -50$ mV, $V_{res} = -60$ mV, and $\tau_{ref} = 1$ ms for interneurons. The subthreshold membrane potential, V(t), follows:

$$C_m \frac{dV(t)}{dt} = -g_L(V(t) - V_L) - I_{syn}(t)$$

where $I_{syn}(t)$ is the total synaptic current to the cell.

2.3.2 Synaptic interactions

The network consists of $N_E = 2048$ pyramidal cells and $N_I = 512$ inhibitory interneurons. Neurons receive recurrent, background, and external inputs. Excitatory synaptic currents are mediated by 2-amino-3-(3-hydroxy-5-methyl-isoxazol-4-yl) propanoic acid receptors (AMPARs) and NMDARs, and inhibitory synaptic currents are mediated by γ-aminobutyric acid type A receptors ($GABA_A$Rs). The total synaptic current to each neuron is

$$I_{syn} = I_{NMDA} + I_{AMPA} + I_{GABA} + I_{ext}$$

where I_{ext} delivers stimulus input to pyramidal cells. The dynamics of synaptic currents for neuron i follow:

$$I_{i,AMPA} = (V_i - V_E) \sum_j g_{ji,AMPA}\ s_{j,AMPA}$$

$$I_{i,NMDA} = (V_i - V_E)\frac{\sum_j g_{ji,NMDA}\ s_{j,NMDA}}{1 + [Mg^{2+}]exp(-0.062V_i/mV)/3.57}$$

$$I_{i,GABA} = (V_i - V_I)\sum_j g_{ji,GABA}\ s_{j,GABA}$$

where $\mathrm{V_E} = 0$ mV and $\mathrm{V_I} = -70$ mV and $\mathrm{g_{ji,syn}}$ denotes the synaptic conductance strength on neuron i from neuron j. NMDAR-mediated currents exhibit voltage dependence controlled by the extracellular magnesium concentration $[\mathrm{Mg^{2+}}] = 1$ mM (Jahr and Stevens 1990).

Given a spike train $\{\mathrm{t_k}\}$ in the presynaptic neuron j, the gating variables $\mathrm{s_{j,AMPA}}$ and $\mathrm{s_{j,GABA}}$ for AMPAR- and GABAR-mediated currents, respectively, are modeled as:

$$\frac{ds}{dt} = \sum_k \delta(t - t_k) - \frac{s}{\tau_s}$$

The gating variable $\mathrm{s_{j,NMDA}}$ for NMDAR-mediated current is modeled as:

$$\frac{dx}{dt} = \alpha_x \sum_k \delta(t - t_k) - \frac{x}{\tau_x}$$

$$\frac{ds}{dt} = \alpha_s x(1 - s) - \frac{s}{\tau_S}$$

with $\alpha_\mathrm{x} = 1$ (dimensionless), $\tau_\mathrm{x} = 2$ ms and $\alpha_\mathrm{s} = 0.5$ kHz. The

decay time constant τ_s is 2 ms for AMPA, 10 ms for GABA, and 100 ms for NMDA. For simplicity, background inputs are mediated entirely by AMPARs, and recurrent excitatory inputs are mediated entirely by NMDARs, as they are critical for the stability of persistent activity (Wang 1999b; Compte et al. 2000; Wang et al. 2013). All cells receive background excitatory inputs from other cortical areas. This overall external input is modeled as uncorrelated Poisson spike trains to each neuron at a rate of $\nu_{ext} = 1800$ Hz per cell, with AMPAR maximal conductances of 3.1 nS on pyramidal cells and 2.38 nS on interneurons.

2.3.3 Network connectivity

As stated above, pyramidal cells are organized in a ring architecture and are tuned to the angular location on a circle (0–360°, Fig. 2.1A), with uniform distribution of their preferred angles. The network structure follows a columnar architecture, such that pyramidal cells with similar stimulus selectivity are preferentially connected to each other. The synaptic conductance on neuron i from neuron j, $g_{ji,syn} = W(\theta_j - \theta_i)G_{syn}$, where θ_i is the preferred angle of neuron i, and $W(\theta_j - \theta_i)$ is the connectivity profile normalized such that:

$$\frac{1}{360^\circ}\int_{0^\circ}^{360^\circ} W(\theta)d\theta = 1$$

For pyramidal-to-pyramidal connections, $W(\theta_j - \theta_i) = J^- + J^+ \exp[-(\theta_j - \theta_i)^2/2\sigma^2]$. We use $J^+ = 1.62$ and $\sigma = 14.4^\circ$. All other synaptic connection profiles are unstructured. Synaptic conduc-

tance strengths are given by G_{EE} = 0.381 nS, G_{EI} = 0.292 nS, G_{IE} = 1.336 nS, G_{II} = 1.024 nS.

2.3.4 Stimulus

Inputs are modeled as injected current with a Gaussian profile, $I(\theta) = I_0 \exp[-(\theta - \theta_c)^2/2\sigma_I^2]$, where the maximum current I_0 = 200 pA, except otherwise noted. θ_c is the stimulus location, and the width parameter $\sigma_I = 18°$.

2.3.5 Slow calcium-dependent nonspecific cationic current

I_{CAN} can trigger a sustained depolarization outlasting the stimulus for several seconds (Haj-Dahmane and Andrade 1998; Strübing et al. 2001; Egorov et al. 2002; Tegnér et al. 2002). The activation of this current requires a rise in intracellular calcium. In some simulations (results in Fig. 2.2, 2.4, 2.5), I_{CAN} was added to the network model (described above) according to the following:

$$I_{CAN} = -g_{CAN} m_{CAN}^2 (V - E_{CAN})$$

$$\frac{dm_{CAN}}{dt} = \phi_{CAN} \times \left(\frac{m_\infty([Ca^{2+}]) - m_{CAN}}{\tau_{CAN}([Ca^{2+}])} \right)$$

$$m_\infty([Ca^{2+}]) = \frac{\alpha[Ca^{2+}]^2}{\alpha[Ca^{2+}]^2 + \beta}$$

$$\tau_{CAN}([Ca^{2+}]) = \frac{1}{\alpha[Ca^{2+}]^2 + \beta}$$

with $g_{CAN} = 1.5$ nS, $E_{CAN} = -20$ mV, $\beta = 0.002$ ms^{-1}, $\alpha = 0.0056$ $[(\text{ms}(\mu\text{M})^2]^{-1}$. ϕ_{CAN} is used to adjust the effective time constant of I_{CAN}, without changing the steady state levels of activity.

Calcium influx to pyramidal cells is triggered by spikes and obeys first-order kinetics as follows (Liu and Wang 2001):

$$\frac{d[Ca^{2+}]}{dt} = \alpha_{Ca} \sum_i \delta(t - t_i) - \frac{[Ca^{2+}]}{\tau_{Ca}}$$

When an action potential fires (at time t_i), $[Ca^{2+}]$ is incremented by α_{Ca} (0.2 μM). The calcium concentration decays back to zero exponentially, with a time constant τ_{Ca} (240 ms).

2.3.6 Depolarization-induced suppression of inhibition

Depolarization-induced suppression of inhibition is detected in various regions of the brain (Llano et al. 1991; Pitler and Alger 1992; Trettel and Levine 2003). DSI is dependent on endocannabinoids that are released by active pyramidal cells, triggered by calcium influx (Ohno-Shosaku et al. 2001; Wilson et al. 2001; Wilson and Nicoll 2001). These endogenous cannabinoids retrogradely activate type 1 cannabinoid receptors (CB1R) located on the axon terminals of interneurons that coexpress GABA and cholecystokinin

(CCK) (Marsicano and Lutz 1999; Katona et al. 1999). The activation of CB1R results in the suppression of transmitter release to postsynaptic pyramidal cells.

DSI was added to the network model (Fig. 2.3, 2.4, 2.5, 2.9) as previously described in Carter and Wang (2007) and the same parameters were used, unless noted otherwise. Briefly, the inhibitory synaptic conductance g_{GABA} to a pyramidal cell is multiplied by a factor D, which is proportional to the fraction of inhibitory synapses that are sensitive to cannabinoid and their presynaptic release probability. D varies between 0 and 1. There is no DSI effect if D is set to 1. DSI is the fractional reduction in inhibitory event size or frequency. The dynamics of D are described by the following equation:

$$\frac{dD}{dt} = \phi_D \times \left(\frac{1 - D}{\tau_D} - \beta_D \times [Ca^{2+}] \times (D - D_{min}) \right)$$

where $[Ca^{2+}]$ represents the intracellular calcium concentration in the pyramidal cell and has the same kinetics as I_{CAN}. When $[Ca^{2+}]$ accumulates, D decreases with a rate controlled by β_D (1.66×10^{-5} $(\mu M \text{ ms})^{-1}$), leading to disinhibition. D is bounded below at D_{min}, which determines the maximum disinhibition and biophysically corresponds to the maximum number of synapses that are cannabinoid sensitive multiplied by the maximal reduction in release probability at each synapse due to DSI. Unless stated otherwise, D_{min} was set to 0.96, corresponding to a maximum DSI of 4%. When the pyramidal cell ceases to be active, D recovers back to maximal value 1 with a

time constant τ_{D} (16.7 s). The factor ϕ_{D} accounts for temperature sensitivity and was used to adjust the effective time constant of DSI without changing the steady state levels of activity.

2.3.7 Short-term facilitation

In simulations where we incorporated short-term facilitation (results in Fig. 2.6, 2.7, 2.8), only the recurrent excitatory synapses are facilitatory. To implement short-term facilitation, the parameter α_{x} is multiplied by F, which is the facilitation factor and obeys the following dynamical equation (Matveev and Wang 2000):

$$\frac{dF}{dt} = \alpha_F \sum_i \delta(t - t_i)(1 - F) - \frac{F}{\tau_F}$$

The parameter α_{F} controls the facilitation potency and was set at 0.6. Starting a paired-pulse facilitation simulation with $\mathrm{F}_0 = 0$, it is possible to demonstrate that, for the first two spikes, with an inter-spike interval 1/r:

$$F_1 = 1 - e^{-\alpha_F} \;\; ; \;\; F_2 = 1 - (1 - F^-)e^{-\alpha_F} \;\; ; \;\; \frac{F_2}{F_1} = 1 + e^{\frac{-1}{r\tau_F} - \alpha_F}$$

2.3.8 Parameter change

A key manipulation in our study is to gradually change the timescale of a biophysical process. For $\mathrm{I}_{\mathrm{CAN}}$, we varied the parameter ϕ_{CAN}, which scales the speed of the channel kinetics without affecting the averaged steady-state level of the activity variable

m_{CAN}. Similarly, we varied the parameter ϕ_{D} to systematically change the time constant of DSI while preserving the average level of the activity variable D. Unlike $\mathrm{I_{CAN}}$ or DSI, for STF the activity variable F undergoes discrete jumps in time and what matters is its value immediately after each jump due to a presynaptic spike, rather than the temporal average. For this reason, we varied τ_{F} directly (see Results for more details).

When a slow mechanism is added to a network model, the overall level of activity of the excitatory population changes significantly, to a degree correlated to the nature and strength of the mechanism. This changes the shape of a population activity pattern and may even disrupt its stability. For this reason, when $\mathrm{I_{CAN}}$, DSI or STF, were present in the model, $\mathrm{G_{EE}}$ was adjusted from 0.381 to 0.378, 0.379 or 0.383 nS, respectively. This way, the network maintained consistently a fixed steady-state activity across all simulations, allowing a fair comparison between scenarios.

2.3.9 Analysis of simulation data

To determine the remembered cue location at any given time, we used the population vector, which is a simple readout of the peak location of a spatially tuned persistent activity pattern (Georgopoulos et al. 1982).

The minimum time to shutdown ($\mathrm{t_{SHUT,MIN}}$), in Figs. 2E, 3E and 6A was determined as follows. For each time constant (τ), a range of shutdown pulse durations ($\mathrm{t_{SHUT}}$) was considered. For each τ and $\mathrm{t_{SHUT}}$, a set of model simulations was run, where an

inhibitory input current lasting for t_{SHUT} was applied when the network was in a bump attractor state. At the end of each simulated trial (seconds after pulse offset), whether the bump state was still present or not was judged through the maximum of the firing rate profile. If more than 95% of simulations of a set yielded successful shutdowns, the corresponding pulse duration was accepted. Finally, for each τ, $t_{SHUT,MIN}$ was chosen as the minimum of those accepted pulse durations.

2.3.10 Bistability analysis and bifurcation diagrams

To plot the bifurcation diagrams in Fig. 2.4 and Fig. 2.7B, we ran simulations across a range of values for the varied parameter (G_{EE} and F profile, respectively) with and without cue input and measured the firing rate during the delay. The maximum firing rate across the network indicated whether the system had evolved to the memory state (typically > 20 Hz) or remained at the baseline state (< 5 Hz).

2.3.11 Simulation method

The model was implemented in python in the Brian simulator (Goodman and Brette 2009). The equations were integrated using a second-order Runge-Kutta algorithm (timestep = 0.02 ms). The simulations were carried out in the cluster facilities of the Yale University Biomedical High Performance Computing Center.

2.4 Results

Our working memory model was designed for an ODR task, which proceeds from cue (angle) presentation, to a delay period and memory-guided behavioral response. The cue stimulus activates a group of pyramidal neurons with preferred directions around the sensory cue (first step current, lower panel of Fig. 2.1B). If the firing rate of this subpopulation of neurons is sufficiently elevated and mutual excitation among them is strong enough, reverberation can give rise to self-sustained persistent activity after the stimulus offset (plateau in Fig. 2.1B, upper panel) (Wang 2001). At the end of the delay, a negative input is applied to all excitatory neurons in the network (Fig. 2.1B, lower panel, second step current). This shutdown pulse should be sufficient long to switch the network back to the baseline resting state.

The spatiotemporal activity pattern of the network model is shown in Fig. 2.1C (left panel). The memory trace is encoded as a population activity pattern that persists during the delay period. The spatial profile of the bump state, corresponding to the activity during the delay period, has a typical Gaussian shape (Fig. 2.1C, right panel). The population vector (shown in yellow) quantifies the peak location of the bump attractor as the internal representation of the sensory cue at any instant. In this example, the remembered cue location fluctuates slightly around the initial cue (180°) and remains reasonably close to it at the end of the delay period. Consequently, in this trial, the PFC circuit model successfully encodes and maintains a spatial memory trace, leading to an accurate

readout.

2.4.1 Dominant time constant determines memory accuracy

The analysis of simulations across trials reveals that the remembered cue (the population vector) as encoded by the network activity pattern displays random drifts over time (Fig. 2.1D). This is because the system is endowed with a continuous family of bump attractors, each for a directional angle as an analog quantity. During a delay period, irregular neural activity leads to random shifting of the network state among those bump states. At the end of a trial, if the drifts have grown over time greatly, the remembered cue location could be located significantly away from the sensory cue angle. This is shown in some trials of Fig. 2.1D, with deviations of more than 20 degrees. These simulations therefore show a relatively low accuracy of memory representation, which implies poor performance. Note that, across trials, the average of random drifts is zero (i.e. there is no systematic drift), whereas the variance increases roughly linearly over time (Camperi and Wang 1998; Compte et al. 2000; Renart et al. 2003; Carter and Wang 2007). This variance of population vector (VPV) quantifies the magnitude of random drifts, which we used as a measure to assess the network's function: the smaller is the VPV, the more accurate is the representation of a memory trace and the better is the behavioral performance.

A key ingredient in our working memory model is that persistent

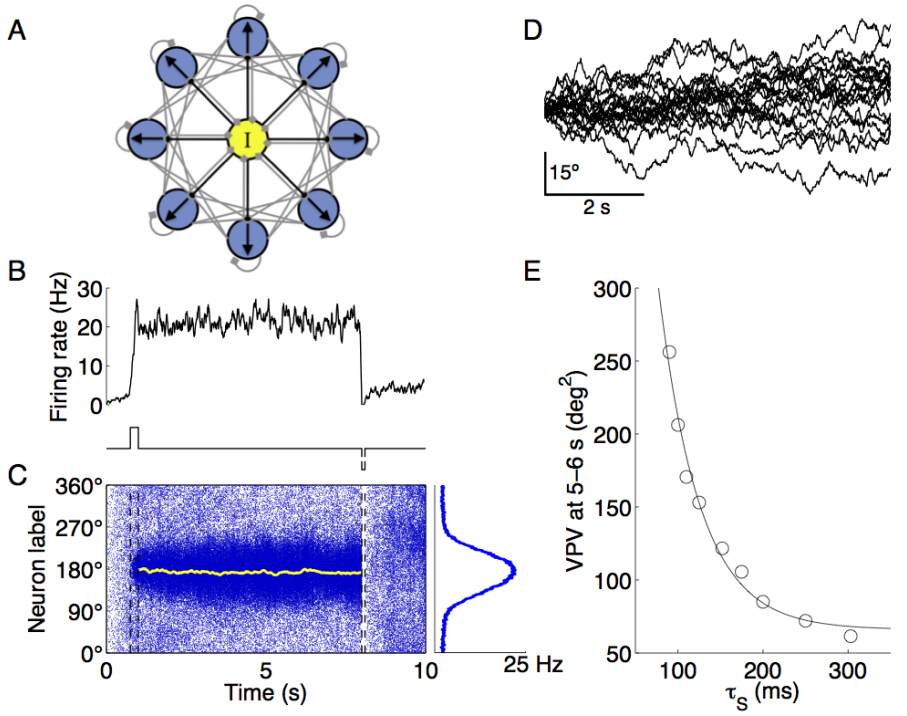

Figure 2.1. Persistent activity and random drifts of a memory trace in a spiking network model for spatial working memory. **A**, schematic of the network connectivity (all-to-all) between the excitatory (blue circles) and inhibitory (yellow circle) neurons. Light gray and black connectors indicate, respectively, excitatory and inhibitory synapses. Each excitatory cell is selective for a direction (black arrows), and the strength of connection between two excitatory cells is a decreasing function of the difference in their preferred directions. **B**, lower panel: applied current to excitatory cells. The first positive step current corresponds to cue presentation. The second negative current represents a shutdown signal. Upper panel: average firing rate of a group of 200 neurons (with preferred directions around cue location) during a trial. The activity ramps up during cue presentation, persists during delay and is reset to a spontaneous baseline by the shutdown pulse. **C**, left panel: spatiotemporal pattern of excitatory cells of the same simulation as in **A** (cue presented at 180 degrees). Each dot represents a spike. (Cont.)

Figure 2.1. (Cont.) The yellow line is the population vector, which traces the peak of the bell-shaped persistent activity pattern (bump attractor) as the internal representation of the cue location. Right panel: population firing profile, averaged over the delay period. **D**, remembered cue as measured by the population vector from 20 sample trials with the same cue location. The memory traces drift away from the initial cue during the delay, the variance of population vector (VPV) across trials quantifies this deviation so that the smaller is the VPV, the more accurate is the memory readout. **E**, drift magnitude at 5–7 s of the delay period, as measured by VPV (N = 500 trials), is plotted as a function of the time constant of the NMDA receptor mediated synaptic excitation τ_S. The VPV decreases steeply with increasing τ_S; the fitting line is an exponential function for ease of eye inspection.

activity is stabilized by slow reverberation mediated by the NMDA receptors at the recurrent excitatory synapses (Wang 1999b). The NMDA receptor dependent synaptic current has a time constant τ_S on the order of 50–100 milliseconds. We hypothesized that, the longer is τ_S, the more robust will be the memory trace. To test this possibility, we gradually varied the value of the NMDAR decay time constant, and measured the variance of the remembered cue location during a delay interval across hundreds of trials. The VPV decreases inversely with increasing τ_S (Fig. 2.1E). The VPV is 206.2 deg^2 with τ_S equal to 100 ms. A substantial reduction in the VPV is observed when τ_S is increased three-fold (300 ms, $\sigma^2 = 61.5$ deg^2). This result serves as a proof-of-principle of the idea that extending the dominant time constants decreases random drifts of persistent activity and improves the accuracy of memory representation. In the following, we will consider three slow, biophysically-plausible mechanisms that are present in the PFC and may improve working

memory function.

2.4.2 I_{CAN} increases memory stability but decreases system flexibility

Fig. 2.2A shows the spiking activity of an integrate-and-fire single neuron model endowed with the slow inward current I_{CAN}. An external current results in action potentials that induce calcium influx, which in turn activates I_{CAN}. After the stimulus offset, the activation of I_{CAN} decays slowly, which allows it to provide positive feedback that is enough to trigger a few additional spikes (afterdischarges). It is worth noting that we assumed that I_{CAN} is not sufficiently strong to produce stable persistent activity in an isolated neuron (Fig. 2.2A), and we were interested in examining the contribution of the activity-dependent I_{CAN} in single neurons to the maintenance of a persistent firing pattern in a recurrent working memory circuit.

We ran simulations with I_{CAN} present in excitatory cells and measured the VPV of the delay-period memory trace across trials. We tested two different values of max τ_{CAN} that lie within the experimentally measured range (Partridge and Valenzuela 1999; Faber et al. 2006; Gross et al. 2009; Sidiropoulou et al. 2009). With a shorter max τ_{CAN} (1 second), the VPV increases quasi-linearly with time (Fig. 2.2B, black curve). By contrast, with max $\tau_{CAN} = 3$ seconds, the VPV shows a pronounced increase during the first second of the delay period and then plateaus in the range 10–15 deg^2 (Fig.

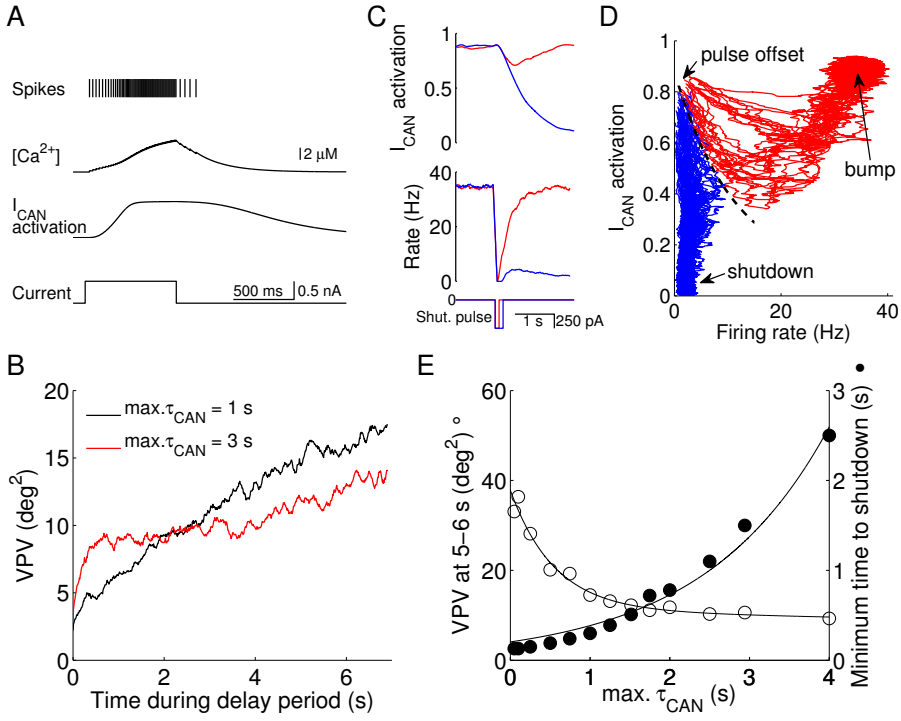

Figure 2.2. Trade-off between memory accuracy and flexibility with I_{CAN}. **A**, an integrate-and-fire neuron model endowed with I_{CAN}. A step current (bottom panel) induces initial firing activity (upper panel). Each spike triggers a small calcium influx (middle upper panel), which leads to a slow activation of I_{CAN} (middle lower panel). When the applied current stops, the high level of I_{CAN} activation is sufficient to induce afterdischarge of spikes. **B**, variance of the remembered cue location (VPV) during the delay period with max τ_{CAN} of 1 (black trace) and 3 (red trace) seconds (N = 500 trials). A longer time constant leads to smaller random drifts after an initial time needed for the mechanism to take effect. **C**, with max τ_{CAN} = 500 ms, a negative pulse of 200 ms to excitatory cells is required in order to shutdown the bump state at the end of delay. Lower panel shows applied current with 2 negative pulses of lasting 100 (red) and 200 (blue) ms. Middle and upper panels: the average population firing rates and I_{CAN} activation, respectively, of 200 cells in the bump state around the initial cue location, under (Cont.)

Figure 2.2. (Cont.) the two conditions (the same color scheme, N = 10 trials). With 100 ms, I_{CAN} activation decays by a small amount but immediately increases after the shutdown input is over, providing the necessary positive feedback for the return of the high-firing memory state. After a longer shutdown pulse (200 ms) the activation decays to such an extent that ultimately leads to the resting state. **D**, state space analysis with the population rate and the I_{CAN} activation shown in **C** plotted against each other in phase space. Each trajectory corresponds to a trial and starts immediately at the shutdown pulse offset. Red trajectories evolve to the bump attractor; blue proceed to shutdown (resting state). There is a clear diagonal boundary that separates the two attractors (dashed black curve), suggesting the presence of an unstable manifold. **E**, trade-off between decrease in variance of remembered cue location (VPV) and minimum time to shutdown ($t_{SHUT,MIN}$), with increasing max τ_{CAN}. Open circles were determined as in **Fig. 2.1E**, with max τ_{CAN} between 50 ms and 4 s. Filled circles express $t_{SHUT,MIN}$ (see Methods) (N = 500 trials). The two data sets are fitted as a sum of two exponentials (VPV) or as a simple exponential ($t_{SHUT,MIN}$). A compromise corresponds to an optimal value of max $\tau_{CAN} \simeq 1.5$ sec.

2.2B, red curve). A possible explanation for the initial rise in drifts (which is not visible for max $\tau_{CAN} = 1$ s) is that with a slower time constant, the I_{CAN} takes longer to be activated and does not provide robustness against drifts as promptly. The crossover between the two time courses shows that shorter τ_{CAN} is more advantageous for shorter delay periods, whereas slower τ_{CAN} increases memory accuracy in longer delays.

The increase in memory robustness provided by I_{CAN}, however, is just one of the effects this current has in the working memory model; the incorporation of a slow mechanism also makes it harder to erase memory. At the end of a delay period, memory erasure was simulated using a negative current input to all excitatory cells,

which completely silences the network. If this pulse is not sufficiently long, the network returns to the memory state, with high I_{CAN} activation and elevated neural firing (Fig. 2.2C, red traces, 100 ms pulse). With a longer shutdown pulse, in contrast, I_{CAN} deactivates to a sufficiently low level that does not allow the return of the high spiking activity and the network is switched off from a bump attractor state (Fig. 2.2C, blue traces, 200 ms pulse).

To further demonstrate the role of I_{CAN} in the memory erasure process, we recorded simultaneously the activation variable of this current and the firing rate of the network and plotted them in a state space, for several trials (Fig. 2.2D). We only recorded neurons around the cue location and in simulations that successfully maintained a memory during the delay. All trajectories initiate immediately after the shutdown ("pulse offset"). There is a clear divergence between two kinds of traces: in a given trial the system's trajectory either revert back to the memory state (red traces, "bump") or decays to the resting state (blue traces, "shutdown"). A boundary (dashed line) separates the regions of attraction of the two states. This result shows that even though a relative weak I_{CAN} (which by itself does not yield persistent activity in a single neuron (Fig. 2.2A)) does not determine whether a network generates persistent activity per se, it can have a remarkably significant impact on the network's behavior.

Therefore, I_{CAN} stabilizes the memory trace by reducing memory drifts over time; at the same time it renders the network less flexible, i.e., it may be harder to load inputs and discard old memories.

This accuracy-flexibility trade-off was demonstrated more explicitly when we varied max τ_{CAN} parametrically (Fig. 2.2E). The increase in max τ_{CAN} decreases the variance of the remembered cue location (the VPV, open circles) but increases the minimum time required to shutdown the network (filled circles). A "sweet spot" corresponds to the crossover point of the two curves (max $\tau_{\mathrm{CAN}} = 1$–2 s), where the VPV is close to the minimum while $t_{\mathrm{SHUT,MIN}}$ is reasonably short (a few hundreds of milliseconds). However, an optimal compromise for a working memory circuit could be different depending on the functional demand that may emphasize either accuracy or flexibility.

2.4.3 DSI shows trade-off between accuracy and flexibility

DSI is a cannabinoid-dependent process through which synaptic inhibition to excitatory neurons is reduced by the magnitude of DSI, which in turn is controlled by the activity of the same E cells (Fig. 2.3A). Thus, for each neuron, a higher level of excitation leads to a weaker inhibition, resulting in an effective positive feedback.

The cells that are most active during an ODR task are those around the peak of the bump activity pattern (Fig. 2.3B, cue location at 180 deg). Therefore, due to its activity-dependence, DSI is the strongest in this group as well. This is depicted in the blue region of the spatiotemporal activity pattern in Fig. 2.3C (note the inverted scale, with hotter colors representing less DSI activation). This creates a favorable bias for the network at the location

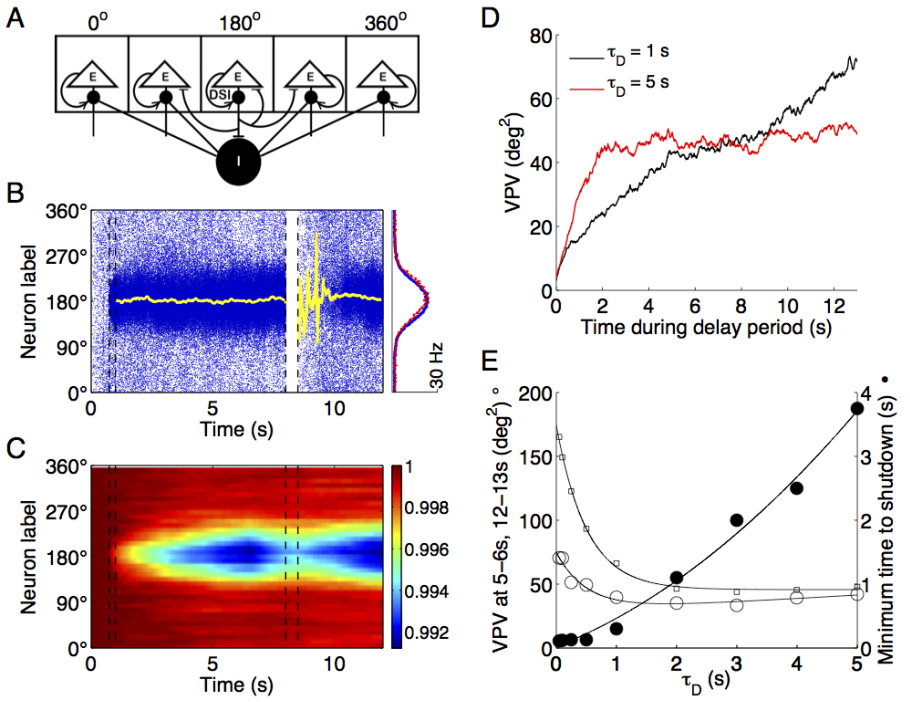

Figure 2.3. Trade-off between memory accuracy and flexibility with DSI. **A**, schematic of network model of spatial working memory endowed with DSI. This mechanism is implemented as a cell-specific reduction in inhibitory input conductance. Adapted from Carter and Wang (2007). **B**, left panel: spatiotemporal pattern of excitatory cells endowed with DSI ($\tau_D = 5$ s). Cue was presented at 180 degrees during the 0.75–1 s interval. A shutdown pulse of 500 ms was applied at 8 s. The yellow lines represent the remembered cue location during delay and after shutdown pulse. Right panel: population firing profiles, averaged over the delay period (blue) or over the last second of the simulation (red), showing that the bump state survives the shutdown input and the memory trace is not erased. **C**, spatiotemporal representation of the activation variable D of DSI (inverted scale, 1 means no DSI) of the same trial. Only the D value of 41 cells (recorded equidistantly in the network) is plotted. The lingering DSI trace, visible after the shutdown pulse, is sufficient to induce the re-emergence of the bump state (in **B**). (Cont.)

Figure 2.3. (Cont.) **D**, the accuracy-flexibility trade-off with DSI. The variance of the remembered cue location (VPV) during the delay period with effective τ_D of 1 (black trace) and 5 (red trace) seconds (N = 500 trials). In the former scenario, the VPV keeps increasing almost linearly. By contrast, in the latter, it stabilizes after an initial period of 2 seconds. **E**, trade-off between decrease in the VPV (open symbols) and $t_{SHUT,MIN}$ (closed circles), as τ_D is increased from 50 ms to 5 s (N = 500 trials). The VPV was determined during two intervals of the delay period: 5–6 s (open circles, same as **Fig. 2.1E** and **Fig. 2.2E**) or 12–13 s (open squares). The data sets were fitted by solid curves for eye inspection.

of the sensory cue, thereby reducing spontaneous drift and stabilizing the neural representation of the remembered cue (Carter and Wang 2007).

In order to quantify this DSI-induced effect, we determined the variance of the remembered cue location (the VPV). We proceeded in a similar way as described above, and the results are remarkably similar. When DSI is controlled by a long time constant (5 s), there is an initial period of rise in drifts (Fig. 2.3D, red trace, first 2 seconds of delay), similar to a network without DSI. However, once the mechanism is fully activated (with a longer delay), the VPV does not grow any longer, reaching a plateau instead. For the shorter time constant (1 s), the variance increases almost monotonically (Fig. 2.3D, black trace).

Another notable feature in the particular sample trial of Fig, 3B-C is the persistence of the inhibition suppression. Given the slow nature of its decay (τ_D = 5 s), DSI does not have sufficient time to fade away during a negative pulse lasting 0.5 s (compare with Fig. 2.1C). The remaining trace of disinhibition is strong enough to

restart the memory bump at approximately the same angle, without a new cue presentation (Fig. 2.3B, right panel, red profile).

As shown in Fig. 2.3E (open symbols), the duration of a step current required to reset the network increases dramatically with τ_{D} (0.5 s: $t_{\mathrm{SHUT,MIN}}$ = 130 ms; 5 s: $t_{\mathrm{SHUT,MIN}}$ = 3.75 s). On the other hand, the variance of the remembered cue location, the VPV, is larger in simulations with short τ_{D} and decreases for progressively longer τ_D, reaching a low plateau for τ_D larger than 1 s. Compared to the control (Fig. 2.1E with τ_{S} = 100 ms, VPV = 206 deg^2) with the same delay period duration of 5–6 seconds, a circuit endowed with DSI displays a smaller variance of drifts overall (VPV = 70.5 deg^2 with τ_{D} = 50 ms, 42.1 deg^2 with τ_{D} = 5 s) (Fig. 2.3E, open circles). With larger delays (12–13 s), the simulations show higher variance due to the accumulation of drifts over a longer time (Fig. 2.3E, open squares). However, in agreement with the traces in Fig. 2.3D, this relative increase of VPV due to longer delays is mostly observed for shorter τ_{D} and is minimal for longer ones. Therefore, our analysis shows a trade-off between the ease of shutdown and memory accuracy which is the same with DSI as that observed with I_{CAN}.

2.4.4 I_{CAN} and DSI enhance the robustness of working memory

We next examined the network behavior when the model system is endowed with a combination of both DSI and I_{CAN}. Specifically,

we quantified the network states in a bifurcation diagram (Fig.4). The desirable behavior corresponds to multistability (the coexistence of a resting state with a low rate and memory states with a high rate), which is realized only in a range of the strength for the recurrent connection between excitatory neurons (G_{EE}). When DSI and I_{CAN} are not present, the multistability range (bounded by two dashed lines) is restricted to a narrow range around $G_{EE} = 0.38$ nS (Fig. 2.4A). If either DSI or I_{CAN} is incorporated (same as in previous simulations: 4% DSI or $g_{CAN} = 1.5$ nS), the lower boundary of the range is extended to smaller G_{EE} values (Fig. 2.4B-C). The maximum broadening effect occurs when both slow mechanisms are present (Fig. 2.4D). This is readily understood: with the help of DSI and I_{CAN}, less recurrent excitation is required to generate persistent activity.

A second noteworthy feature of Fig. 2.4 is that the slow biophysical mechanisms increase the firing rate of memory states while that of the resting state remains roughly the same. This is because DSI and I_{CAN} are activity-dependent, therefore minimal in the low-firing spontaneous activity but significant in the high-rate memory states. This leads to a larger separation between the resting and memory states. Consequently, a random fluctuation in spontaneous spiking activity will be less prone to give rise to a "false" memory, and the network function is more reliable.

To conclude, I_{CAN} and DSI are beneficiary to the system by making it less sensitive to variations of the network properties (such as G_{EE}), and less prone to spontaneous transitions by noise between

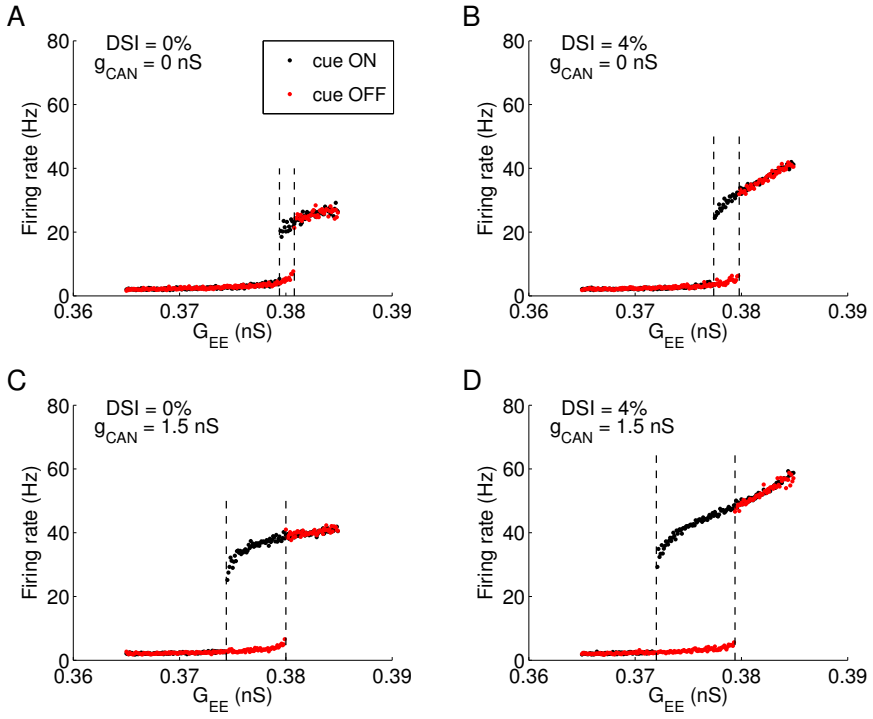

Figure 2.4. Multistability analysis of the working memory model as a dynamical system reveals that I_{CAN} and DSI increase the robustness of memory function. Simulations were ran with (black dots) or without (red dots) cue presentation, for a range of recurrent excitatory conductance (G_{EE}) values. The maximum firing rate among all excitatory cells, at the end of the delay period, is either low (2–6 Hz) corresponding to the resting state or higher than 20 Hz corresponding to a memory sate. The resulting state diagram is shown for the control network without slow mechanisms (**A**), with only DSI (**B**) or I_{CAN} (**C**) or both (**D**). The range of G_{EE} values for multi stability is delimited by 2 vertical dashed lines. The presence of DSI (**B**) and I_{CAN} (**C**) alone increased the multistability range and also the firing rate separation between memory and resting states. These effects are larger when both mechanisms are combined (**D**).

the resting state and memory states. Both effects enhance the robustness of working memory behavior.

2.4.5 I_{CAN} and DSI counteract heterogeneity

Network models endowed with a continuum of attractor states require that its constituent neurons have identical properties (Ben-Yishai et al. 1995). Under this condition, if a localized pattern of activity is spatially displaced, it will lead to another identical pattern centered at the new location. However, any neural network shows a certain degree of variability across cells (Marder and Goaillard 2006). Can DSI and I_{CAN} remedy the system's vulnerability to heterogeneity, by virtue of creating a privileged location in the network in an activity-dependent manner? To investigate this question, we implemented a modest amount of heterogeneity, by assuming that the leak potential V_L varies from cell to cell according to a Gaussian distribution (mean $V_L = -70$ mV and standard deviation $SD(V_L) = 1$ mV).

Across a large number of trials, the input cues are presented at 20 angle locations equally distributed along the 360 degrees of a circle. When both mechanisms are absent, the remembered cue locations display systematic drifts and, as previously reported (Renart et al. 2003), tend to converge to a few privileged locations (Fig. 2.5A, $\theta = 180$ and 320 deg). These locations are determined by the heterogeneous distribution of the cellular excitability across the network, which disrupts the continuous family of bump attractors. The mean drift from the cue location is minimal in networks with DSI and I_{CAN} (8.9 $\pm$ 6.9 deg) and significantly different (2-sample t-test, $p = 5\times10^{-110}$) from that of the control network (46.7 $\pm$ 32.5 deg) (Fig. 2.5C).

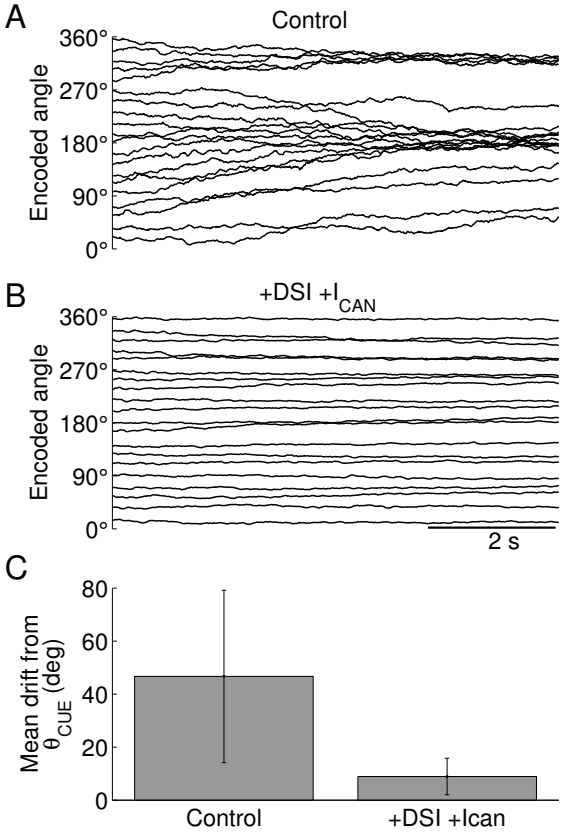

Figure 2.5. DSI and I_{CAN} stabilize the memory trace in the presence of heterogeneity across neurons in the network. Simulations were carried out where the cue was applied at 20 evenly spaced locations along the 360 degrees space. The maintenance and retrieval of memory require that the remembered location at any given point in time should closely match that of the to-be-remembered cue. **A**, the remembered cue locations of the simulations with the control parameter set systematically drift to a few privileged locations. **B**, when DSI (4% maximum effect) and I_{CAN} (g_{CAN} = 1.5 nS) were incorporated in the network, the internal representation of the cue location becomes much better (the population vector is nearly stable across time). **C**, the mean drift from the original cue location (at the end of a 9 s delay) is greatly reduced with DSI and I_{CAN} compared to the control (N = 500 trials).

Intuitively, when DSI and I_{CAN} are included, the remembered cue locations show much smaller drifts (Fig. 2.5B). Both mechanisms are activity-dependent, so they create a privileged location in the network that "traps" a bump attractor encoding the sensory cue. These slow mechanisms are powerful enough to overcome the disrupting effect of heterogeneity.

2.4.6 Short-term facilitation increases memory accuracy

Finally, we considered the effect of short-term facilitation (STF) in our working memory model. STF shares similar features with I_{CAN} and DSI, namely activity-dependence, positive feedback and slow time course of activation (Zucker 1989; Tsodyks and Markram 1997; Fisher et al. 1997; Abbott and Regehr 2004). It is especially prevalent in excitatory synapses between pyramidal cells in the frontal cortex (Hempel et al. 2000; Wang et al. 2006).

The implementation of STF in the model reduced random drifts of the memory trace during the delay. Compared to the control network (Fig. 2.1E, $\tau_S = 100$ ms, VPV = 206 deg^2) the variance of the remembered cue location was lower for any τ_F (Fig. 2.6A, open circles, VPV ranges 71–126 deg^2). However, contrary to DSI and I_{CAN}, the VPV increased rather than decreases with longer τ_F. This unexpected result is elucidated by the analysis of a profile of the peak value of the facilitation variable F, for a bump attractor. For each cell in the network, every time there is a spike, F is increased

by a discrete jump and the resulting value F^+ is used to update the synaptic conductance. Between spikes, F decayed until the next spike takes place. Thus, neurons in the bump that had elevated firing rates also show higher F^+ (profile in Fig. 2.6B). For longer τ_{F}, the decay is very slow, resulting in more temporal summation and, eventually, in a saturation of F^+ (Fig. 2.6B, gray dashed double arrow). A wide steady state F^+ profile effectively removed the facilitation effect in that spatial region and selective enhancement created by the activity-dependent positive feedback. For this reason, augmenting the STF time constant increased memory drifts and, consequently, increased the variance of the remembered cue location (Fig. 2.6A, open circles).

This saturating feature was not observed with the other two slow mechanisms because of the following differences between the biological processes. The magnitudes of $\mathrm{I_{CAN}}$ and DSI vary quasi-continuously over time through their dependence on intracellular calcium, which accumulates and declines slowly. Furthermore, they influence the excitability of the cell at almost any point in time. Therefore, the spatial profile of the activity variable (m_{CAN} or D, respectively) can be fixed and remains not saturating, when the time constant is varied through a scaling factor (ϕ_{CAN} or ϕ_{D}). On the other hand, STF is not a continuous process but acts only during synaptic events. This means that the value of the variable F is only used at times of spikes (F^+) and ignored when it decays away between spikes. For this reason, a scaling method is not appropriate because it would only preserve the time-averaged steady state of F

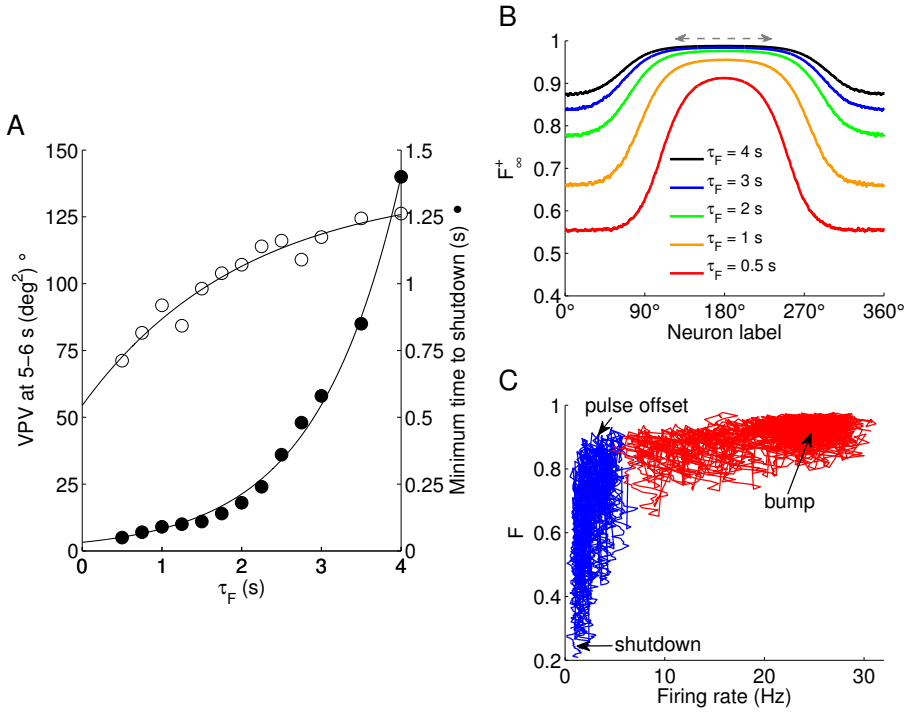

Figure 2.6. Short-term facilitation of recurrent excitatory synapses reduces random drifts. **A**, $t_{SHUT,MIN}$ (filled circles) increases with τ_F (fitted with an exponential equation). Likewise, the variance of the remembered cue location (VPV) also increases with slower STF (exponential fit), but remains much smaller than that in the absence of short-term facilitation (VPV = 206 deg^2 in **Fig. 2.1E**, τ_S = 100 ms) (N = 500). **B**, steady-state profiles of F^+ (the facilitation variable, F, after a spike) for 5 different τ_F (7 s after delay start, N = 400). For longer time constants, the peak of the profile broadens (dashed gray double-arrow), resulting in a region effectively without facilitation. This explains increased drifts with longer τ_F. **C**, phase space plot of F and the population firing rate. Each trajectory corresponds to a trial and starts immediately at the shutdown pulse offset. The network either revert back to the mnemonic bump state (trials in red) or rest to the resting state (trials in blue), depending on the stochastic network dynamics. The F variable (Cont.)

Figure 2.6. (Cont.) fluctuates from trial to trial and is significantly larger in red trajectories than blue ones (see Results). Note that, at the pulse offset, the population of excitatory cells was silent. However, due to the temporal sliding window (50 ms) used to calculate firing rates, the trajectories depicted start at > 0 Hz.

but not the steady state of F^+.

Similarly to what is observed for I_{CAN} and DSI, prolonged STF time constant makes it more difficult to reset the network (Fig. 2.6A, filled circles). When τ_F is 0.5 s, the required time to shutdown is just 50 ms. At the other end of the tested range, a τ_F of 4 s requires a negative input pulse lasting for at least 1.4 s to erase a memory trace.

The minimum shutdown time is determined by the decay for F during the inhibitory input. At the end of the shutdown phase, the magnitude of F for neurons in the bump attractor reaches a level that depends on the pulse duration and τ_F. This level fluctuates from trial to trial, and has a large influence on whether the bump reappears or not in any given trial. In Fig. 2.6C are shown the system trajectory in the state space of F and firing rate, for 40 trials with $\tau_F = 1$ s, which corresponds to a minimum time to shutdown of 90 ms (Fig. 2.6A). The red traces ($t_{SHUT,MIN} = 50$ ms, leading to return of the bump state) start at an average of $F = 0.89 \pm 0.02$, while the blue ones ($t_{SHUT,MIN} = 100$ ms, leading to shutdown) begin at $F = 0.84 \pm 0.04$ - a significant difference (2-sample t-test, $p = 8.58\times10^{-6}$). Longer τ_F require longer shutdown pulses in order for F to decay to a low enough level, so that the recurrent excitation

is too weak to enable the bump to reemerge.

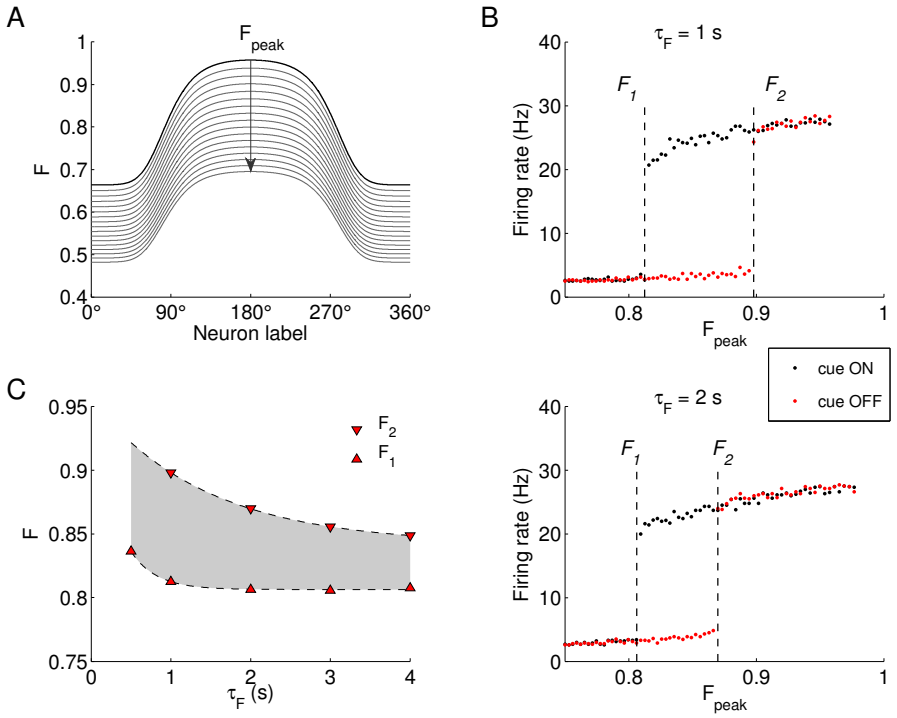

Figure 2.7. A simplified model with fixed F profile shows that the network is multistable within a range of STF values. **A**, the black curve corresponds to the orange profile ($\tau_F = 1$ s) in **Fig. 2.6B**, and the other curves were obtained by assuming an exponential decay in time of the black profile, during different temporal intervals (see Results). **B**, bifurcation diagram for $\tau_F = 1$ and 2 seconds (upper and lower panels, respectively). Simulations were run with (black dots) or without (red dots) cue presentation, and plotted is the maximum firing rate among all excitatory cells, at the end of the delay period. In these simulations, F did not change dynamically but was set as a parameter and given spatial profiles as those shown in **A**. The peaks of the corresponding F profiles are shown in the abscissa. Below F_1, the network was always in the resting state. Above F_2, no cue was necessary to initiate a bump. **C**, F_1 and F_2 as a function of $\tau_F = 0.5$, 1, 2, 3, 4 s (fit with single exponentials). The shaded area represents the presence of multistability.

To shed further insights into how the STF variable F determines the fate of the system after a shutdown input, we performed a bifurcation analysis of the system as a function of the F spatial profile. Specifically, we started with the spatial profile of F at the onset of a shutdown input (Fig. 2.7A, black curve), averaged over a number of trials from simulations with $\tau_{\mathrm{F}} = 1$ s (N = 400 trials). During the shutdown period, there is no spiking activity, therefore F simply decays exponentially with τ_{F}, which is depicted by gray profiles in Fig. 2.7A for periods of 4 to 328 ms, in 4 ms steps (only 16 examples are shown, downward arrow). This replicates the decay of F during the shutdown phase, with different pulse durations. Then, a new set of simulations were carried out, in which F is no longer time-varying, but is fixed as one of the spatial profiles shown in Fig. 2.7A, each with a particular maximum $\mathrm{F_{peak}}$, and the possible network states are plotted as a function of $\mathrm{F_{peak}}$ (Fig. 2.7B). For each profile, a pair of simulations was carried out, with and without cue stimulus. At the end of the delay, the maximum firing rate of the overall network indicated whether the network was in the resting state (< 5 Hz) or in the memory state (> 20 Hz). In principle, the profiles that resulted from decays longer than $\mathrm{t_{SHUT,MIN}}$ should not be able to sustain a bump without cue. A similar method was applied to $\tau_{\mathrm{F}} = 0.5$, 2 (Fig. 2.7B, lower panel), 3 and 4 s. The main difference between different values of τ_{F} was the shape of the spatial F profiles, which are broader for longer τ_{F} as seen in Fig. 2.6B. For each τ_{F}, the values of $\mathrm{F_{peak}}$ at which the system would cross between memory state and resting state were determined (Fig. 2.7B, $\mathrm{F_1}$ and

F_2). The shaded area in Fig. 2.7C represents the bistability range in the parameter space. With longer STF time constants, it was necessary to reach a lower F_{peak} such that simulations without cue input would remain in the resting state (below F_2). This behavior roughly corresponds to the increase in $t_{SHUT,MIN}$ for longer τ_F, in simulations where F changes dynamically.

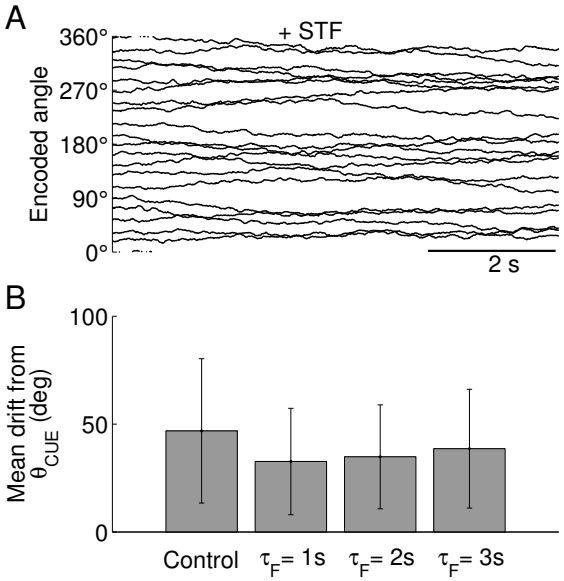

Figure 2.8. Short-term facilitation stabilizes the remembered cue locations in the presence of heterogeneity across neurons in the network. In stimulations, the cue location was applied at 20 evenly spaced locations along the 360 degrees space. **A**, the remembered cue locations with STF (τ_F = 1 s) show visibly less drifts than the control (**Fig. 2.5A**). **B**, the mean heterogeneity-induced systematic drifts (at the end of a 9 s delay) for the network model without STF (control) or with STF operating at 3 different time constants (N = 400).

As was shown in a recent study using a firing-rate model, systematic drifts of memory trace due to heterogeneity could be dra-

matically reduced by STF (Itskov et al. 2011). We checked the effect of STF in our spiking network model in the presence of cellular heterogeneity ($< V_L > = -70$ mV and $SD(V_L) = 1$ mV). It is evident by visual inspection that with STF the memory storage of the sensory cue is more stable over time (Fig. 2.8A), compared to those under the control condition without STF (Fig. 2.5A). This impression is confirmed statistically (Fig. 2.8B). There is a significant (2-sample t-test) decrease in the mean drifts between the control network (without STF, 46.9 ± 33.4 deg) and each of the three scenarios with a different τ_F (1 s, 32.7 ± 24.7 deg, $p = 2\times10^{-11}$; 2 s, 34.8 ± 24.1 deg, $p = 8\times10^{-9}$; 3 s, 38.6 ± 27.5 deg, $p = 1\times10^{-4}$).

In summary, like I_{CAN} and DSI, STF reduces noise-induced random drifts or heterogeneity-induced systematic drifts of memory traces, thereby rendering working memory function more robust. In contrast to the other two slow mechanisms, a longer time constant of STF leads to larger drifts of a memory trace, but drifts remain smaller than those in the control network without STF.

2.4.7 Slow mechanisms protect memory against distractors

A cortical circuit assigned to store a particular stimulus in memory may receive, at any point in time, additional external signals with the potential to transform its performance and output. Depending on the nature of the new, distractor signal, the circuit may respond within a range of possible behaviors. It can erase the previ-

ous memory and encode a new one. It can also let the second stimulus influence the configuration of the established memory. Finally, the circuit may discard the distraction. Considering the influence that slow mechanisms have on memory robustness and flexibility, they may also play a crucial role in this process.

In our network model, if we apply a particular distractor stimulus during the delay period, the new remembered cue location will shift towards its location and away from the cue stimulus angle. The deviation of the bump peak location is clearly visible for a network with the control parameter set (Fig. 2.9A, upper panel, $\theta_1 = 178$ deg, $\theta_2 = 244$ deg). The magnitude of this deviation ($\theta_2 - \theta_1$) depends on the angular difference between the cue stimulus (θ_S) and the distractor (θ_D). The distraction increases with $\theta_D - \theta_S$ before reaching a maximum. Beyond this point, the influence of the distractor decreases abruptly and the final location of the bump is much closer to the cue angle. Longer distractor durations result in significantly larger deviations of the final memory trace (Fig. 2.9B, 500 ms).

When DSI is incorporated in the network, the deviation of the bump induced by a distractor is visibly smaller (Fig. 2.9A, lower panel, $\theta_1 = 185$ deg, $\theta_2 = 196$ deg) than in the control network. This outcome is observed across the range $\theta_D - \theta_S$ and for all distractor durations (Fig. 2.9C). Consequently, the maximum distraction (Fig. 2.9D, upper panel) with DSI is smaller and grows slower with distractor duration (150 ms, 11.5 ± 3.7 deg; 500 ms, 29.0 ± 4.8 deg) than in control conditions (150 ms, 41.6 ± 12.3 deg; 500 ms, 135.0

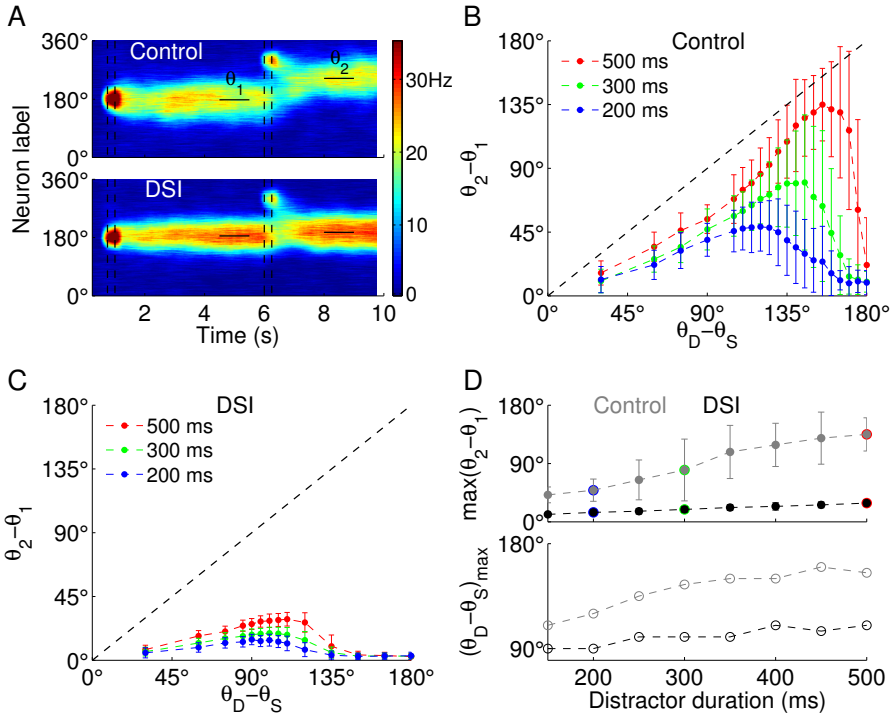

Figure 2.9. Slow mechanisms preserve cue representation and decrease the influence of long distractor stimuli. **A**, smoothed spatiotemporal activity pattern of the network's excitatory cells under control conditions (upper panel) or with DSI (lower panel), in the presence of a distractor. An initial cue stimulus (peak angle $\theta_S = 180°$, 750 ms – 1 s, first pair of vertical dashed lines) drives the network to the memory state. The application of a distractor during the delay period (peak angle $\theta_D = 300°$, 100 pA, 6 s – 6.25 s, second pair of dashed lines) pulls the location of the bump closer to it. In these two example trials, the deviation of the bump, measured as the difference between the remembered cue location after the distractor (θ_2, 8 s – 9 s) and before (θ_1, 4.5 s – 5.5 s), is larger in the control network than with DSI. **B**, the average difference between θ_2 and θ_1 as a function of the difference in peak angles of distractor (θ_D) and cue stimulus (θ_S), for 3 distractor durations (N = 150). The deviation increases and approaches the perfect distraction (diagonal dashed line) before declining for more distant distractors. (Cont.)

Figure 2.9. (Cont.) Longer durations produce generally larger deviations that have a maximum at larger distractor angles. **C**, same as in **B** but for network with DSI. The differences in remembered cue locations are visibly smaller than with the control network for all three distractor durations (N = 150). **D**, distraction indicators for sets of trials with different distractor durations, under control network (gray symbols) or with DSI (black symbols). Upper panel: the maximum distraction is small and increases almost linearly in a network with DSI. Under control conditions, this measure is larger throughout the whole range and has a more prominent increase. The edge-colored data points were taken from **B** and **C** with the same color scheme. Lower panel: similarly, the distraction angle ($\theta_D - \theta_S$) at which the maximum deviation of the bump is observed is wide and increases with duration in the control network, but is narrower and almost stable when DSI is present. This slow mechanism limits the effects of closer distractors and protects the memory against farther ones almost independently of their duration.

$\pm$ 25.6 deg,). The angle difference between distractor and cue that originated those maximum distractions ($(\theta_D - \theta_S)_{max}$) corresponds to the distractor location that has maximum influence on the memory bump. This indicator was higher with control parameters than with DSI for all distractor durations. Remarkably, the presence of the slow mechanism resulted in a more stable $(\theta_D - \theta_S)_{max}$ (150 ms, 90 deg; 500 ms, 110 deg) than in control network (150 ms, 110 deg; 500 ms, 155 deg). Taken together these results suggest that DSI decrease the influence of all distractors regardless of their location. Moreover, it reduces the range of distractor locations that significantly deviate the memory bump. Finally, the protection against farther distractors is almost independent of their duration.

2.5 Discussion

By now it is commonly recognized that a working memory circuit should not be conceptualized in terms of rapid switches between attractor states. Instead, reverberation underlying persistent activity must be slow, likely involving the NMDAR receptors at recurrent excitatory synapses (Wang 1999b; Wang et al. 2013). Slow network dynamics enables a single microcircuit mechanism to subserve working memory and decision-making. The latter requires accumulation of information over time by virtue of slow neural transients such as quasi-linear ramping activity (Wang 2002; Wang 2008). It is noteworthy that persistent activity during a mnemonic delay period often displays slow temporal variations, as well as a rich heterogeneity across neurons (Batuev et al. 1979; Baeg et al. 2003; Miller et al. 2003; Goldman 2009; Machens et al. 2010; Barak et al. 2013; Stokes et al. 2013).

Is the slower the underlying mechanism, the better? In the present work, we investigated three biophysical mechanisms in a network model of spatial working memory. I_{CAN}, DSI and STF are present in frontal neurons and are activity-dependent. They provide positive feedback to active excitatory cells and operate on a slow timescale. Our main finding was that slow timescale has a trade-off effect. I_{CAN}, DSI and STF render working memory representation more robust. However, their slow decay leaves a lingering memory trace even after the termination of persistent firing activity, which makes it difficult to reset the circuit by brief inputs, a fundamental requirement for normal function of a working memory system.

2.5.1 Random drifts

Our study started with the premise that very slow processes are not necessary for the generation of persistent activity per se, but may play a role in determining the accuracy and robustness of a working memory circuit's behavior. It has been previously reported that, in continuous attractor networks, a mnemonic activity pattern (bump attractor) exhibits random drifts that accumulate over time and deviate the stored spatial information away from the cue location (Camperi and Wang 1998; Compte et al. 2000; Carter and Wang 2007). This decreases the accuracy of the memory readout. We found that the incorporation of DSI, I_{CAN} or STF helps to reduce random drifts of a memory trace. Moreover, we demonstrated that this stabilizing effect is dependent on the effective time constant of the mechanism considered. For I_{CAN} and DSI, the increase in τ is associated with a decrease in random drifts before reaching a plateau (approximately 1–2s). By contrast, with STF, while it also increases accuracy when compared to the control network, random drifts actually increase with τ_F. We showed that this happens because, for longer time constants, the facilitation variable F saturates around the bump, effectively removing facilitation in that part of the network.

2.5.2 Heterogeneity-induced drifts

A different type of drifts of memory trace arises from heterogeneity across neurons, which is detrimental to the realization of

a continuous family of attractors. A homeostatic mechanism that scales the excitatory synapses was shown to recover the accuracy of the remembered cue location under those conditions (Renart et al. 2003). This activity-dependent mechanism scales the excitatory synaptic weights of each cell so that the long-term average firing rate is similar for all and equal to a predetermined level. Recently, it was demonstrated using a firing-rate model that short-term facilitation slows down the velocity of drifts in the presence of synaptic heterogeneity (Itskov et al. 2011). Building upon these insights and following our successful stabilization of random drifts, we tested the effect of the three slow mechanisms on our spiking model in the presence of cellular heterogeneity. A combination of I_{CAN} and DSI effectively counteracted the tendency of a bump to drift to privileged locations, during a relatively long delay period. Likewise, short-term facilitation significantly reduced systematic drifts due to heterogeneity, strengthening the previous results with a biophysically realistic spiking network model.

2.5.3 Memory flexibility

Whereas slow biophysical mechanisms increased the accuracy of memory representation, they have the opposite implications on the flexibility to switch between dynamical states. We utilized the duration of a negative step current to the excitatory cells as a measure of the ability to reset a bump and erase memory. This analysis leads us to very similar conclusions regarding I_{CAN}, DSI and STF. The minimum duration of the pulse required to shutdown the net-

work dramatically increases with the effective time constant of the mechanism.

We also studied how a slow mechanism may help preserve the location of the memory bump against distractor stimuli. DSI limits the effects of closer distractors and protects the memory against farther ones almost independently of their duration. Whereas this effect is desirable to discard unwanted stimuli, it also uncovers the potential for inter-trial persistency. When a new cue is presented at a different location, the trace of disinhibition from the previous trial will act as a distractor and pull the location of the new bump towards the old one. Taken together, these results establish a trade-off between memory accuracy and flexibility.

2.5.4 Slow mechanisms modulate dynamics of a working memory system

The bifurcation analysis of the network model with G_{EE} as a control parameter revealed that, in the presence of DSI and I_{CAN}, the model system shows a wider multistability range and larger separation between the firing rate of persistent activity and resting states. Wider multistability range implies a higher degree of robustness because normal function is less sensitive to variations of network properties. A larger separation of firing rates implies that it is harder for spontaneous transitions between states to occur merely by noise. We also showed that the realistic range of the facilitation factor F contained a multistability range that shifts with the time

constant τ_F. These raise the possibility that, in a working memory circuit such as PFC, some modulatory mechanisms could flexibly tune slow biophysical processes for optimal behavior.

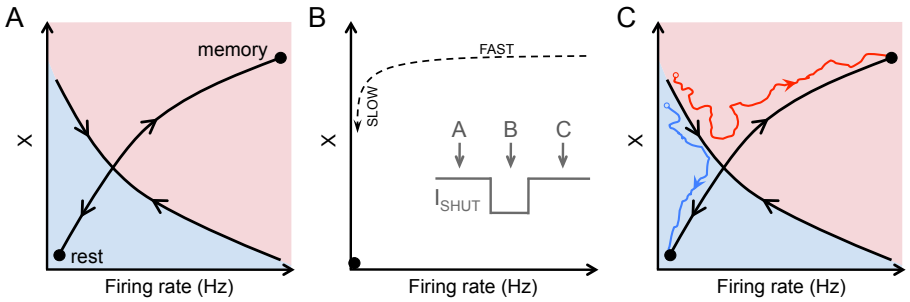

Figure 2.10. Summary phase-plane diagram of our working memory model, during three stages of a shutdown process. This scheme applies to all three slow biophysical mechanisms considered in this paper, with X representing the activation variable of I_{CAN}, DSI or STF. The inset in **B** displays the timing of the three stages according to the presentation of the negative shutdown input. **A**, the state space displays a stable manifold (line with converging arrows) and an unstable manifold (line with diverging arrows), their intersection creates a saddle point. There are two stable steady states (filled circle) representing a memory state and a rest state. at the end of delay, the system is in the memory state. **B**, during the application of the negative pulse, there is only one steady state (filled circle), with low firing rate and low X magnitude. After the quick suppression of all firing activity ("FAST"), the system moves along the direction of the exponential decay of X ("SLOW") over the duration of the pulse. **C**, the attractor landscape (**A**) is restored after the pulse offset. Depending on whether the state of the system at the offset of the shutdown input is on the left or the right side of the stable manifold, the system will revert back to the memory state (red trajectory) or reset to the resting state (blue trajectory, successful shutdown).

Fig. 2.10 offers a conceptual understanding common for all three slow mechanisms. This schematic depiction is partly deduced from the phase space plots in Fig. 2.2D and Fig. 2.6C. It shows, in a

state space, how activity of neurons engaged in working memory storage and the activation variable (X) of any of the three slow mechanisms interact with each other dynamically. Just before the shutdown pulse (Fig. 2.10A), the phase-plane consists of a stable manifold, which separates the resting and memory attractors, and an unstable manifold. The intersection between the two lines creates an unstable saddle point. During the shutdown pulse presentation (Fig. 2.10B), only the resting state exists. The negative input pulse immediately inhibits all firing activity and X decays exponentially. At the pulse offset (Fig. 2.10C), the system regains its previous landscape with both attractors. Afterwards, the network trajectory depends on the extent of X decay, which is an exponential function of the duration of the pulse. If X is below the stable manifold, the system will progress to the resting state, resulting in a successful shutdown (blue trace). Otherwise, if X decayed less and remains above the stable manifold at the pulse offset, the system will revert back to the mnemonic attractor state (red trace).

2.5.5 Accuracy-flexibility trade-off

The circuits of the prefrontal cortex that encode working memory, like all systems in the nervous system, have a rich variety of processes that modulate their performance. In this study, we considered a group of mechanisms that may be involved in the dynamical stabilization of the memory trace. The apparent conflict resulting from a trade-off between accuracy and flexibility of the memory trace may turn out to be significant for neural modulation. Accord-

ing to environmental conditions and behavioral task demands, the network may be instructed to tilt the balance in favor of increased accuracy at the expense of flexibility. Under these circumstances, I_{CAN}, DSI or STF may be strongly activated so that the memory is encoded as precisely as possible. On the other hand, when the task requires faster response to cue stimulation, the network may be tuned to decrease the activation of the slow mechanisms or shorten their time constants. This prevents the previous memory from interfering with the encoding of the new stimulus. It has been proposed that an emphasis on robust online representation of information versus rapid switching could be adjusted by dopamine signaling, with D1 (respectively D2) receptors acting in favor of robustness (respectively flexibility) (Durstewitz and Seamans 2008; Rolls et al. 2008). Our results suggest that slow processes, including those studied here, are potentially effective targets of action by dopamine or other neuromodulators, which can optimally adjust the tradeoff between robustness of memory storage and cognitive flexibility.

At the present time, there still exists a large gap between neural circuits and behavior (Carandini 2012); this wide gap must be bridged in order to achieve our goal of understanding the brain mechanisms of cognitive functions and their impairments associated with mental disorders. The present work illustrates how biophysically-based computational modeling, in interplay with experimentation, can help make progress in this direction, through elucidation of how specific cellular and synaptic processes shape network activ-

ity patterns (persistent activity) and contribute to a key functional requirement (accuracy-flexibility tradeoff) in a cognitive process.

Chapter 3

Physiological function of I_H in pyramidal cells

3.1 Abstract

The activity of the prefrontal cortex is determined by a repertoire of biophysical properties. A recent study investigated the cellular mechanisms of working memory modulation in circuits of the prefrontal cortex. According to the experimental results, a key modulator on this cognitive process is the nonselective hyperpolarized-activated H-current (I_H) found in spines of pyramidal neurons of the prefrontal cortex. I_H blockage resulted in augmented neural firing in these cells, stronger persistent activity of the network and improved working memory task performance. In a different study, I_H blockage was found to increase the number of action potentials recorded in pyramidal cells during membrane depolarization phases designated by Up states. These and other studies suggest that I_H increases the neural excitability in pyramidal cells of the prefrontal cortex. In order to understand the exact mechanisms of I_H function, we modeled this current in a single compartment model. We found that I_H alone could not account for the changes observed in experiments. We proved that I_H is a mostly depolarizing current and its blockage leads to a decrease in the generation of action potentials. We confirmed these findings in a multi compartment model that better represents the geometry of pyramidal cells. Additionally, our findings support the importance of thin dendritic spines in the electrical filtering of synaptic inputs, as shown in experiments. Furthermore, we proved that the previously proposed interaction of I_H and a M-type potassium contains serious flaws and does not provide a valid explanation for this data. Nevertheless, we demon-

strated that the latter current alone may have an important role in controlling the overall levels of activity in working memory circuits.

3.2 Introduction

The cognitive functions that depend on the prefrontal cortex are determined by an intricate assembly of molecular, synaptic and circuital mechanisms, which are under the influence of modulatory pathways. The study of how each of these processes influences behavior requires a multi-disciplinary approach, which allows to infer the connection between different levels of complexity.

Working memory function is thought to be represented by persistent activity sustained by recurrent connections between neurons, and is strongly modulated by catecholamines, including dopamine and norepinefrine (Brozoski et al. 1979; Arnsten et al. 1994; Williams and Goldman-Rakic 1995; Henze et al. 2000; Seamans et al. 2001; Durstewitz and Seamans 2002; Seamans and Yang 2004; Birnbaum et al. 2004; Ramos et al. 2005; Vijayraghavan et al. 2007). A recent work employed a variety of techniques including electrophysiology, electron microscopy and pharmacology to understand how the activation of a type of norepinephrine postsynaptic receptors, α2A-adrenoceptors (α2A-ARs) strengthens PFC networks and improves working memory (Wang et al. 2007). These authors carried out neuron recordings in area 46 of the dorsolateral PFC of monkeys performing a spatial working memory task. At the same time, through iontophoresis, they applied agonists and antagonists of the relevant mechanisms involved in this modulatory process. Their findings lead them to conclude that the activation of α2A-ARs initiates a intracellular signaling cascade, which results in the increase in the firing activity of pyramidal cells tuned for the

stimulus, during the delay period.

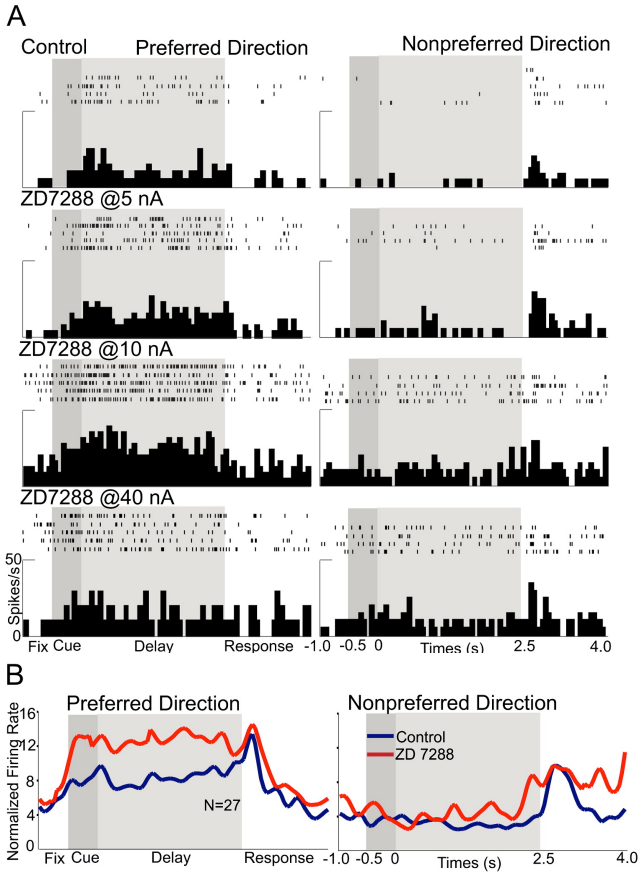

Figure 3.1. Blockage of HCN channels strengthens working memory-related firing of PFC neurons. **A**, iontophoretic application of ZD7288 caused a dose-dependent effect on delay-related firing in a neuron with weak tuning under control condition. ZD7288 at 5 nA and 10 nA enhanced delay-related activity, while a high dose (40 nA) eroded the spatial tuning. **B**, enhancing effect of ZD7288 (red) on delay related activity at the population level (27 neurons). Adapted from Wang et al. (2007).

One of the first steps in this signaling cascade is the inhibition of cyclic adenosine monophosphate (cAMP). A consequence of this inhibition was the closing of Hyperpolarization-activated Cyclic

Nucleotide-gated (HCN) channels, which are responsible for carrying the H-current (I_H). Moreover, they determined that the direct blockage of these channels with the compound ZD7288 also strengthened the pyramidal cells delay-period firing activity, and most importantly, it reversed the effect of the application of a α2A-ARs antagonist. The effect of ZD7288 was recorded both at single cell (Fig. 3.1A) and population level (Fig. 3.1B). The relationship between these cellular components was further emphasized by the discovery that the HCN channels co-localize with α2A-ARs in dendritic spines (Fig. 3.2). The pharmacological manipulation with iontophoresis is very localized and does not produce any noticeable change in the performance of the task. In order to test the behavioral effects, these authors conducted a second set of experiments where I_H was reduced in rat prelimbic PFC, either through HCN knockdown or ZD7288 infusion. This resulted in an improvement of the performance in a spatial working memory task (Wang et al. 2007).

A different type of reverberatory circuit dynamics is the low-frequency ($<$ 1Hz) oscillatory activity, which is recorded in the cortex during slow-wave sleep and anesthesia (Metherate and Ashe 1993; Steriade et al. 1993; Cowan and Wilson 1994; Contreras et al. 1996; Destexhe et al. 1999; Sanchez-Vives and McCormick 2000; Steriade et al. 2001). This activity is self sustained by recurrent dynamics and creates phases of elevated membrane potential with higher firing activity (Up states) intercalated with silent period with hyperpolarized V_m (Down states). The Up and Down

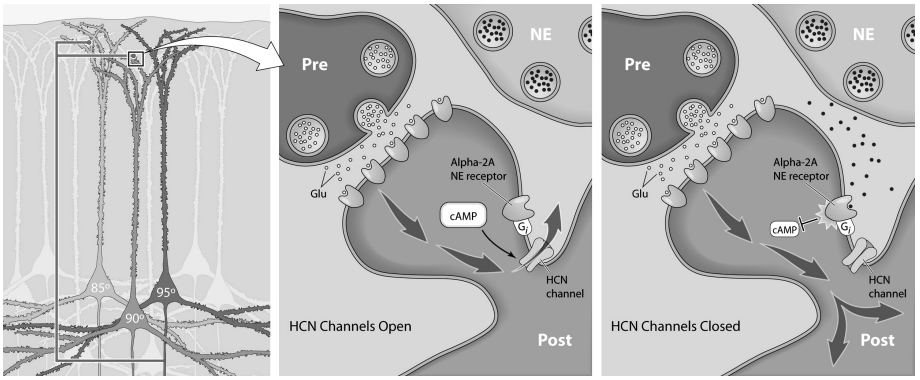

Figure 3.2. A Model of α2A-cAMP-HCN Regulation of PFC Microcircuits. HCN channel opening shunts synaptic inputs onto dendritic spines and reduces network activity. a2A-AR stimulation inhibits the production of cAMP and increases the efficacy of cortical inputs. Adapted from Wang et al. (2007).

states gradually disappear during waking, leading to a tonically depolarized state with low firing rates (Steriade et al. 1996; Steriade et al. 2001; Timofeev et al. 2001). The role of this phenomenon in cognition has not been totally understood, but it is prevalent in animals and has been the focus of much research.

It is a tremendous challenge to study these mechanisms in living animals. For this reason, several studies perform pharmacological manipulation and electrophysiological recordings in reduced preparations obtained from slices of brain tissue. A recent experimental study addressed how I_H controls Up and Down states in cortical pyramidal cells (Y Shu, A Hasenstaub, C Ghandi and D McCormick, unpublished observations). Through electrophysiological recordings of slices from the somatosensory and prefrontal cortex of ferret, they registered the effects of blocking HCN channels

with ZD7288. This blockage resulted in a hyperpolarization of the resting membrane potential during silent periods (Down states). Strikingly, it also produced an increase in the intensity of discharge of single pyramidal cells during Up states. The firing rates were elevated from 1.8±1.7 Hz in control to 9.2±4.9 Hz after bath application of ZD7288 to the slice preparation. A second result of the HCN channels blockage was the enhancement of the Up state duration (0.68±0.3 seconds to 2.3±0.3 seconds).

I_H plays a key role in the modulation of persistent activity during working memory (Wang et al. 2007) and control of duration and frequency of Up states (Shu et al, unpublished observations). This current is mediated by a nonselective flux of cations, is active at hyperpolarized membrane potentials, de-activates above the action potential threshold and operates at a relatively slow timescale (Luthi and McCormick 1998; Biel et al. 2009). I_H is carried by either of 4 subunits of HCN channels (HCN1-4). In the neocortex and hippocampus, I_H is carried by HCN1 and HCN2 with high sensitivity to cAMP (Chen et al. 2001; Ulens and Tytgat 2001). In pyramidal cells, HCN channels are located mostly on the distal dendrites with a gradual decrease in presence towards the cell body (Lorincz et al. 2002; Notomi and Shigemoto 2004).

This spatial distribution of HCN channels in the dendrites was suggested to be crucial to counteract location-dependent temporal differences of dendritic inputs (Magee 1998; Magee 1999; Williams and Stuart 2000; Berger et al. 2001; Vaidya and Johnston 2013). Due to the cable-like properties of dendrites, excitatory postsy-

naptic potentials (EPSPs) originating distally tend to reach the soma with larger widths, which increases the temporal summation of trains of inputs, compared to the ones originating in proximal dendrites. According to these studies, the mostly distal presence of I_H counteracts this effect so that all EPSPs reach the soma with the same width. Another study showed that it is the total density of HCN channels in dendrites and not the gradient that determines this normalization (Angelo et al. 2007).

The role of I_H in cellular excitability is still controversial. The main current of thought proposes that the activation of this current leads to a decrease in excitability (Poolos et al. 2002; Fan et al. 2005; Rosenkranz and Johnston 2006) and, conversely, its down-regulation should elevate the generation of action potentials (Shah et al. 2004; Kole et al. 2007; Jung et al. 2007). These effects have been explained by a decrease in the input resistance and a reduction of temporal summation when HCN channels open and vice versa. However, this view is in apparent contradiction with the accepted evidence that this inward current depolarizes the membrane potential in the subthreshold range and increases the excitability in pacemaking cells (DiFrancesco 1993; Clapham 1998) and in at least one epilepsy study (Dyhrfjeld-Johnsen et al. 2008).

In this project we studied how I_H contributes to the excitability of PFC pyramidal cells. First, we used a simple single compartment model to identity the key principles of the physiological function of I_H. Secondly, we employed a multi-compartment model of a pyramidal cell to ascertain if those rules stand true with a more realis-

tic cellular representation in terms of architecture of dendrites and spines and distribution of ionic channels. Additionally, we tested a previously proposed hypothesis based on the interaction of I_H with a M-type potassium current (George et al. 2009). Finally, we contextualize our results with the current views of the function of I_H in the neurons of the prefrontal cortex.

3.3 Materials and Methods

3.3.1 Single and multi compartment models of pyramidal cells

To simulate how an electrical signal is propagated from the synapse to other regions of a pyramidal cell we used two compartment models following the Hodgkin-Huxley formalism. The single compartment model has a length of 20 μm and diameter of 20 μm.

For the multi-compartment model we adopted the geometry of a reduced model of a neocortical pyramidal cell (Bush and Sejnowski 1993; Bush and Sejnowski 1994). This model has 8 compartments: apical tuft (length 140 μm, radius 1 μm), apical #1 (180 μm, 1.2 μm), apical trunk (35 μm, 1.25 μm), apical oblique (200 μm, 1.15 μm), soma (21 μm, 7.65 μm), basal trunk (50 μm, 1.25 μm) and a pair of basal dendrites (150 μm, 0.8 μm) (Fig. 3.3). For this study, we added a dendritic spine connected to the apical tuft. The spine structural details were obtained from electron microscopy measurements provided by Constantinos Paspalas and were represented in the model by two compartments: head (length 0.3 μm, radius 0.3 μm) and spine neck (1 μm, 35 nm). In some simulations, the radius of the spine neck was varied to change its resistance (Figs. 3.8, 3.11B).

In both models, the membrane potential for each compartment V_c follows:

$$C_m A_c \frac{dV_c}{dt} = -A_c(I_L + I_{ion}) - I_{coup} - I_{syn}$$

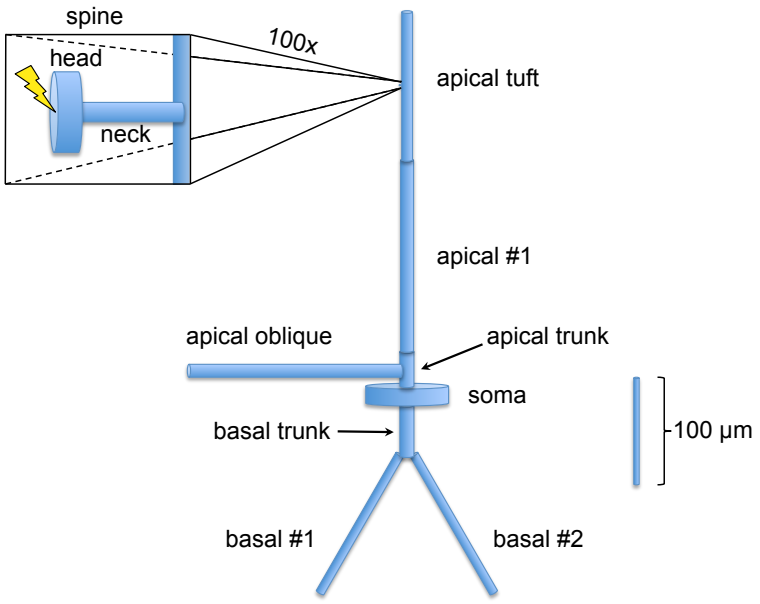

Figure 3.3. Schematic representation of the single cell compartment model of a neocortical pyramidal cell. The model comprises 10 compartments: spine head, spine neck, apical tuft, apical #1, apical trunk, apical oblique, soma, basal trunk, basal #1 and basal #2. The length (but not the radius) of each compartment was drawn according to the scale. The spine, attached to the apical tuft, was magnified 100x for better visualization. The input, modeled as an alpha-function, was applied to the spine head compartment.

where A_c is the surface area of the compartment. The specific membrane capacitance $C_m = 1\ \mu F/cm^2$ (multiplied by a scaling factor of 2.95 in the multi compartment model). The leak current $I_L = g_L(V_c - V_L)$, with $V_L = -70$ mV and $g_L = 0.3$ mS/cm^2 (single compartment) or $g_L = 0.15$ mS/cm^2 (multi compartment). I_{ion} and I_{syn} represent the ionic currents and synaptic input, respectively, that are present in that particular compartment (see below for description). I_{coup} describes the current that flows between coupled

compartments. For the single compartment model, $I_{coup} = 0$. In the complete model, each compartment c is connected to its neighbor compartments, n:

$$I_{coup} = \sum_{n} g_{cn}(V_c - V_n)$$

According to the geometry of the model (Fig. 3.3), a compartment can be connected to one (spine head, apical oblique, basals #1 and #2), two (spine neck, apical tuft, apical #1 and soma) or three neighbor compartments (apical trunk, basal trunk). g_{cn} depends on the properties of the pair of connected compartments:

$$g_{cn} = \frac{1}{\frac{r_c - r_n}{2}}$$

with r_c, r_n, the resistance of each connected compartments, described as:

$$r_x = \frac{l_x \times R_i}{A_{cross,x}}$$

with $x = c, n$, length of the compartment l_x, specific axial resistance of the cytoplasm $R_i = 200\ \Omega$cm, cross-sectional area $A_{cross,x}$.

3.3.2 Synaptic Input

I_{syn} is the synaptic current, which, in the multi-compartment model, is only applied to the spine head; all other compartments did not receive external input. The synaptic EPSP was adapted

from the NEURON software package (Carnevale and Hines 2006):

$$I_{syn} = g(V_c - V_E)$$

where $V_E = 0$ mV and g is the synaptic conductance defined by the following alpha function:

$$g = g_{max} \times \frac{t - onset}{t_{peak}} \times exp(-\frac{t - onset - t_{peak}}{t_{peak}}), \quad for\ t > onset$$

where the maximum conductance $g_{max} = 1$ nS, except otherwise noted. The onset is the time at which the change in postsynaptic conductance begins, and the peak of the conductance change occurs at $t_{peak} = 2$ ms.

In some simulations with the single compartment model, the term $-I_{syn}$ in the membrane potential expression was replaced by I_{app}, a step current.

3.3.3 Ionic currents

The ionic currents, I_{ion}, included in simulations of both models are:

$$I_{ion} = I_H + I_M$$

where I_H is the inward current mediated by the hyperpolarization-activated cyclic nucleotide-gated (HCN) channels and I_M is the outward M-type current, carried by KCNQ potassium channels.

The voltage-dependent currents are described by the Hodgkin-Huxley formalism. Thus, a gating variable g satisfies a first-order kinetics:

$$\frac{dg}{dt} = \phi_g(\alpha_g(V_m)(1-g) - \beta_g(V_m)g) = \phi_g \frac{g_\infty(V_m) - g}{\tau_g(V_m)}$$

where $\phi_g = 1$ unless specified otherwise.

I_H is given by:

$$I_H = g_H H(V_m - V_H)$$

with $V_H = -40\ mV$ and the gating variable H at steady state defined as:

$$H_\infty = \frac{1}{1 + exp(\frac{V_m+80}{10})}$$

and time constant:

$$\tau_H = \frac{200}{exp(\frac{V_m+70}{20}) + exp(-\frac{V_m+70}{20})} + 5$$

I_M is expressed as:

$$I_M = g_M m(V_m - V_K)$$

with $V_K = -80$ mV and the gating variable at steady state defined as:

$$m_\infty = \frac{1}{1 + exp(-\frac{V_m+44}{6})}$$

and time constant:

$$\tau_M = \frac{200}{exp(-\frac{V_m+44}{12}) + exp(\frac{V_m+44}{12})}$$

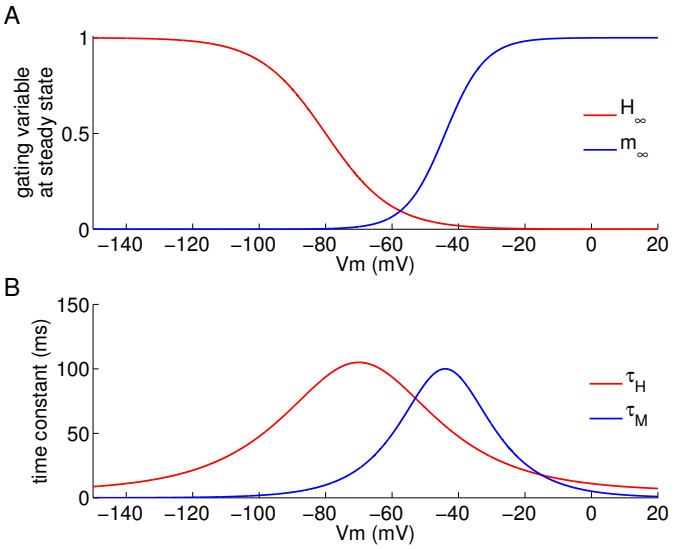

Figure 3.4. Representation of I_H and I_M kinetics. **A**, gating variables at steady state. I_H, determined by H_∞, is active at hyperpolarized membrane potentials and is mostly deactivated at V_m close to action potential generation threshold (−50 mV). Its half-activation potential is −80 mV. I_M, determined by m_∞, has the opposite functioning pattern and is half-active at −44 mV. **B**, the time constants τ_H and τ_M have similar dependency on V_m. Both have a maximum of approximately 100 ms, observed at potentials separated by 26 mV.

The maximum conductances of I_H and I_M, g_H and g_M, respec-

tively, were varied in each simulation within a biological-plausible range of values. The membrane potential dependence of the steady state activation curves and time constants is shown in Fig. 3.4.

The spike-generating currents (I_{Na} and I_K) were added to the single compartment model uniquely to obtain the f-I curve in Fig. 3.7. The sodium current is expressed as:

$$I_{Na} = g_{Na} m_\infty^3 h (V_m - V_{Na})$$

where the fast activation variable is replaced by its steady-state:

$$m_\infty = \frac{\alpha_m}{\alpha_m + \beta_m}$$

$$\alpha_m = \frac{-0.1(V_m + 31)}{exp(-0.1(V_m + 31)) - 1} \; ; \; \beta_m = 4 \; exp(-\frac{V_m + 56}{18})$$

and the inactivation variable is defined by:

$$\alpha_h = 0.07 \; exp(-\frac{V_m + 47}{20}) \; ; \; \beta_h = \frac{1}{exp(-0.1(V_m + 17)) + 1}$$

The delayed rectifier is expressed as:

$$I_K = g_K n^4 (V_m - V_K)$$

where:

$$\alpha_n = \frac{-0.01(V_m + 34)}{exp(-0.1(V_m + 34)) - 1} \; ; \; \beta_n = 0.125 \; exp(-\frac{V_m + 44}{80})$$

The parameters are: $g_{Na} = 55\,mS/cm^2$, $g_K = 15\,mS/cm^2$, $V_{Na} = 55$ mV, $V_K = -80$ mV, $\phi_h = 4$ and $\phi_n = 4$.

3.3.4 Network model of spatial working memory

The working memory results presented in this chapter were obtained with the spiking network model for the oculomotor delayed-response (ODR) task, previously described (Compte et al. 2000). The model consists of a population of excitatory pyramidal cells and a population of inhibitory interneurons. Pyramidal cells are arranged in a ring-like fashion and labeled by their preferred cue direction, from 0 to 360 degrees. The specifications for single cell properties, synaptic interactions, network connectivity and stimulus input are the same as described in sections 2.3.1, 2.3.2, 2.3.3 and 2.3.4, respectively. The only modification is the inclusion of I_M in the subthreshold membrane potential expression, with the same kinetics as described in section 3.3.3.

3.3.5 Simulation method and Analysis of data

The implementation of the compartment models and the analysis of data were done in Matlab programming language and numerical computing environment. The integration of the differential equations was done with a variable-step implicit solver.

3.4 Results

3.4.1 I_H has a depolarizing net effect on membrane potential

To test the basic kinetic properties of I_H we included it in a simple single-compartment model. For different values of g_H we applied a synaptic current and registered the resulting EPSP. We observed that the increase in H-conductance reduced the amplitude of the EPSP (peak minus resting membrane potential) but elevated its peak heigth (Fig. 3.5). This duality reveals the double action

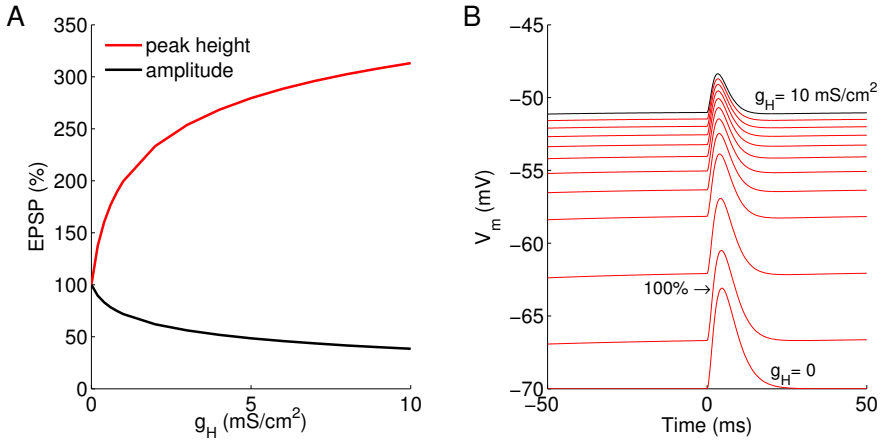

Figure 3.5. I_H in a single compartment model increases the peak height. **A**, the presence of larger g_H reduces the EPSP amplitude (black curve) but increases its peak height (red curve). These two measurements were normalized to the EPSP with no I_H (marked 100% in **B**). **B**, 12 example EPSP traces for the scenarios with g_H= 0 to g_H = 100 mS/cm^2 (in black for visibility). Even though the EPSP amplitude increases with g_H (0 mS/cm^2, 6.1 mV; 100 mS/cm^2, 2.6 mV), the peak is always higher due to the elevation of the resting membrane potential (g_H = 0, V_{rest} = -70.0 mV; g_H = 100 mS/cm^2, V_{rest} = -51.0 mV).

of I_H. On one hand, it depolarizes the membrane at rest, raising the baseline V_m. On the other hand, it reduces the membrane input resistance, which shortens the voltage deflection produced by a stimulation. The net result of the presence of I_H in our single compartment model is a depolarization that leads to an increase in the EPSP height.

To further characterize the dual effect of the H-current in the membrane potential, we decomposed I_H in two components:

$$I_H = I_{H,tonic} + I_{H,phasic}$$

with

$$I_{H,tonic} = g_H H(V_L - V_H)$$

and

$$I_{H,phasic} = g_H H(V_m - V_L)$$

The tonic component of the current, according to the expression, is always negative ($V_L - V_H$), thus depolarizing. The phasic effect acts as a leak current (reversal potential V_L). The conductances of both are naturally determined by the gating state of HCN channels. To determine the relative contributions of both components, we ran numerical simulations of the single compartment model with a constant step current (I_{app}) and different configurations of $I_{H,tonic}$, $I_{H,phasic}$ and I_L. At rest (steady state), I_{app} equals the magnitude of

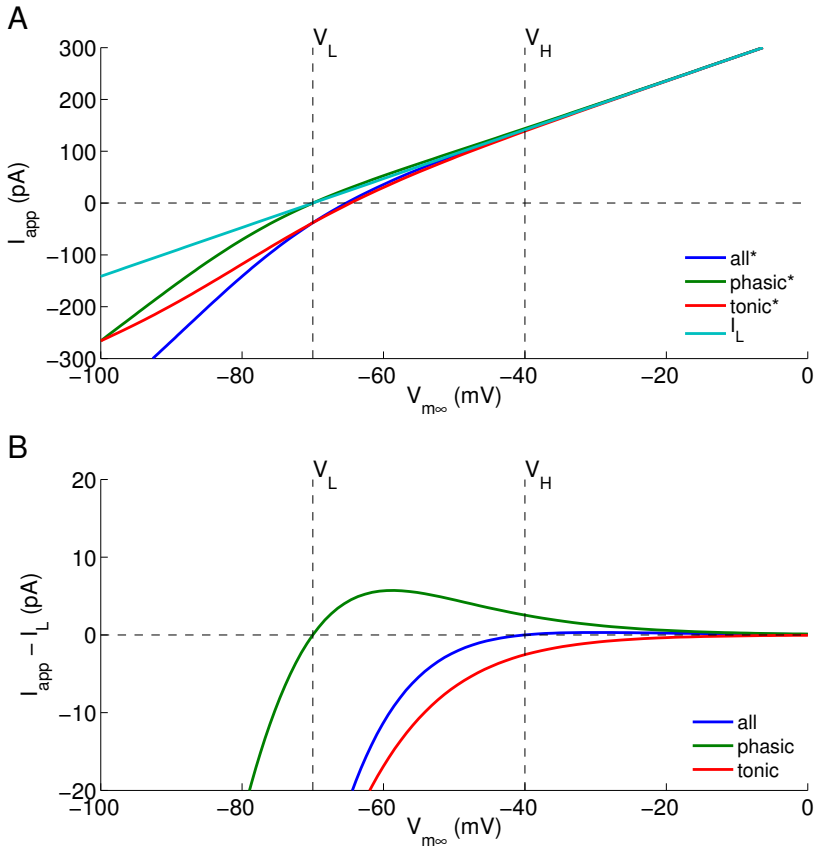

Figure 3.6. In the action potential threshold V_m range, I_H is depolarizing. Simulations of single compartment model with 3 currents: constant I_{app}, I_L and I_H (decomposed in phasic and tonic terms). Four simulations were run with different current configurations. **A**, steady state of V_m determines I_{app}, which for each simulation corresponds to either full I_H + I_L (all*), phasic term + I_L (phasic*), tonic term + I_L (tonic*) and only I_L ($g_H = 0$). **B**, for each data set, the difference between I_{app} and I_L represents the magnitude of each component of I_H. The phasic component (green) is positive (hyperpolarizing, outward current) above V_L. On the other hand, the tonic effect is always negative (depolarizing inward current). (Cont.)

Figure 3.6. (Cont.) The net current (blue) is negative below V_H, which includes the range below action potential generation. It becomes positive above the reversal potential, but the reduced level of activation of I_H at these membrane potentials (determined by H) severely diminishes its magnitude.

the other included currents (Fig. 3.6A). By subtracting I_L to I_{app}, one obtains $I_{H,phasic}$ and/or I_L. The tonic component, as expected, was always negative (Fig. 3.6B red curve). The phasic effect is only positive (outward, hyperpolarizing, Fig. 3.6B green curve) above V_H, but at this range I_H is almost deactivated. The end result is a strongly depolarizing I_H current.

These results clearly show that I_H alone can not account for the shunting of synaptic inputs at dendritc spines in pyramidal cells and the resulting decrease in neural excitability. The same conclusion was reached by another study, which proposed a new explanation for the experimental results: the interaction between I_H and another current, namely M-type potassium current (I_M) (George et al. 2009). As seen in Fig. 3.4, I_H is hyperpolarized-activated, while I_M has the opposite activation pattern. At rest, I_H elevates the membrane potential, shifting it to the region where the gating of I_M is higher. Consequently, when a synaptic input is received, I_M should be more active and promote the shunting of the EPSP. On the other hand, when the HCN blocker ZD7288 is applied, V_m stays hyperpolarized and I_M does not reach higher levels of activation, which decreases its shunting effect and results in higher EPSP peaks after synaptic inputs. It is relevant to note that for this I_H

+ I_M shunting to be effective, the input current has to be strong enough to counteract the elevation of V_{rest} with I_H. Below this strength (dependent of the conductances used), the EPSP peak is higher with I_H than without it; once above it, the opposite happens - this was referred to as the crossover effect (George et al. 2009).

However, to obtain this effect, g_M has to be very large (35 mS/cm^2). The presence of such a large outward current suggests that the generation of action potentials could be compromised, an issue that was not addressed in the original study (George et al. 2009). For this reason, we tested how the presence of both I_H and I_M influences the spiking behavior of a cell. To generate action potentials, we included the Hodgkin-Huxley-type sodium (I_{Na}) and delayed rectifier potassium (I_K) currents to our single compartment model.

As expected from the previous results with the passive model, I_H alone has a depolarizing effect, and induces an increase in the firing rate and a decrease in the threshold current needed to initiate an action potential (Fig. 3.7, dashed red trace, $g_H = 10$ mS/cm^2), compared to the control conditions (Fig. 3.7, solid red trace, null g_H and g_M). On the other hand, the presence of I_M with the large conductance required for the crossover effect ($g_M = 35$ mS/cm^2) inhibits the generation of continuous action potentials (Fig. 3.7, black traces), regardless of the inclusion of I_H. This result demonstrates that the proposed hypothesis of interplay between I_H and I_M to explain the experimental results of the HCN channels blockage is not satisfactory when the site of action potential generation has the

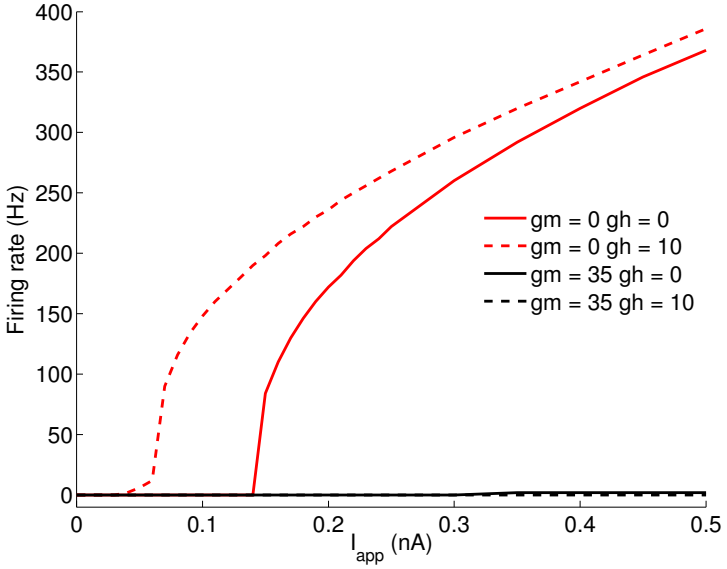

Figure 3.7. Presence of I_M inhibits generation of action potentials. f-I curves for the single compartment model for 4 different conditions (conductances in mS/cm^2). With the control condition, the threshold current needed to generate action potentials is 0.15 nA and the firing rate at 0.2 nA and 0.5 nA is 172 and 368 Hz, respectively. The presence of I_H increases the ease to fire (threshold of 0.04 nA) and increases the firing rates over the range of I_{app} (0.2 nA, 26 Hz, 0.5 nA, 386 Hz). When I_M was included there was no continuous firing. A single spike was generated for $I_{app} > 0.35$ nA. The leak conductance was doubled from the previous simulations to avoid spontaneous firing with I_H. The input was administered as a constant step current.

required channel conductances.

The single compartment model allowed us to determine the basic physiological contribution of I_H and I_M during rest, after EPSP-like perturbations of the membrane potential and in spike generation. However, several other properties of a real pyramidal cell could influence its precise mechanism of action, such as dendritic architecture, channel distribution and synaptic localization.

3.4.2 Resistance of spine neck influences electrical filtering

To further our understating of I_H within a more realistic cell representation, we built a multi-compartment model that includes a spine in the dendritic tuft, which is the site of the input. Spines are micro-structures in the dendritic branches that receive most of the excitatory chemical synapses in the pyramidal cells. They have a particular geometry that could potentially affect the transfer of electrical signal between synapses and the rest of the cell. Generally, the post-synaptic density is located at a bulbous structure called head, which is then connected to the dendrite through the neck, a tubular structure. The geometry of neocortical spines exhibits a continuum of variability and is though to be correlated with the synaptic function (Arellano et al. 2007). It was proposed that the thin long necks play a key role in the gating of synaptic inputs in the working memory (Wang et al. 2007) (see Fig. 3.2).

In our model, we considered thin dendritic spines that are present in pyramidal cells of the PFC. We based our geometric parameters on measurements obtained through high-resolution immunoelectron microscopy of superficial layers of the macaque dorsolateral PFC (Paspalas et al. 2013). We tested how the electrical resistance of the spine neck, adjusted by its radius, influences the electrical signal that flows from the spine head to the dendritic branches. The resistance is inversely proportional to the cross-sectional area, which increases with the radius. Therefore, thinner spines should confer

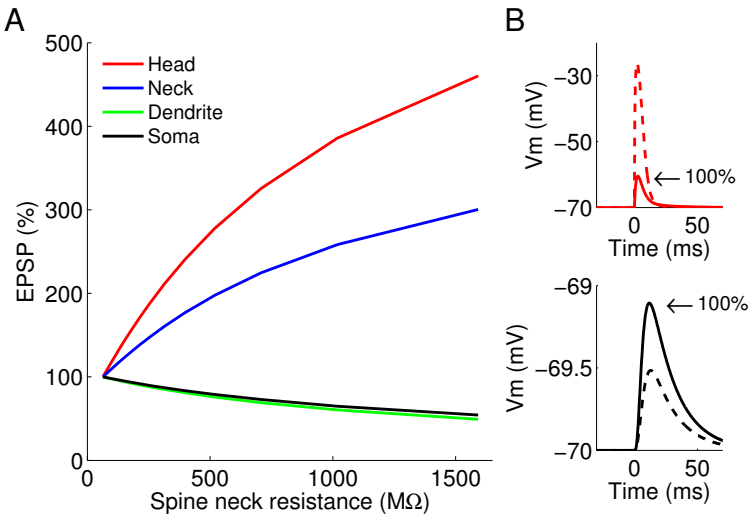

Figure 3.8. Spine resistance affects EPSP amplitude measured at 4 compartments (spine head, spine neck, spiny dendritic compartment and soma). **A**, measurements were normalized to the scenario with lower neck resistance (63.7 MΩ, marked with 100% in **B**). The reduction of the somatic and dendritic EPSPs is bigger for higher values of spine neck resistance (45.7% and 50.8% at 1591.5 MΩ, respectively). On the other hand, the EPSPs measured at the spine (head and neck) have the inverse relation (at 1591.5 MΩ: neck, 300.4%; head, 460.3%). **B**, the dendritic (upper panel, red) and somatic (lower panel, black) EPSP traces for the scenarios with smaller (solid lines) and larger (dashed lines) neck resistance. The spine neck resistance was adjusted by changing the radius in the range 0.1–0.02 μm.

more resistance to the axial propagation of the EPSP.

In our model, by raising the spine neck resistance from 63.7 to 1591.5 MΩ we obtained a dramatic increase of the EPSP measured at the spine (300.4% in neck and 460.3% in head) (Fig. 3.8). This is a clear indication that the higher neck resistance results in a larger voltage deflection at the spine, thus larger input resistance. On the other hand, the EPSP measured at the dendrite and soma

significantly decreased (amplitude reduction of 50.8% and 45.7%, respectively) suggesting that we created a bigger electrical compartmentalization between the spine and the rest of the cell. For the following work with the multi compartment model, we used a spine neck radius of 0.035 μm, which was the average determined by immunoelectron microscopy experiments (Paspalas et al. 2013) and provides a resistance of 519.7 MΩ.

3.4.3 Presence of I_H in dendrites increases the somatic EPSP peaks

Immunoelectron microscopy images show that HCN channels are present in the dendriditc spines (Wang et al. 2007). In order to address the impact of their presence on the electric filtering, we included I_H to the spiny compartments of our single cell model. Like in the single compartment model, we observed that the increase in g_H reduced the amplitude of the EPSP (Fig. 3.9A) but elevated its peak (Fig. 3.9C) in all recorded locations. The presence of I_H in the spine of our multi compartment model results in an increase of the EPSP that is transferred to the soma. Consequently, it contributes to the generation of action potentials and promotes the overall cellular excitability.

We had already demonstrated that the I_H and I_M interplay hypothesis proposed by George et al. (2009) was not satisfactory within a single compartment model because it required a high M-conductance that inhibits action potentials. However, this propo-

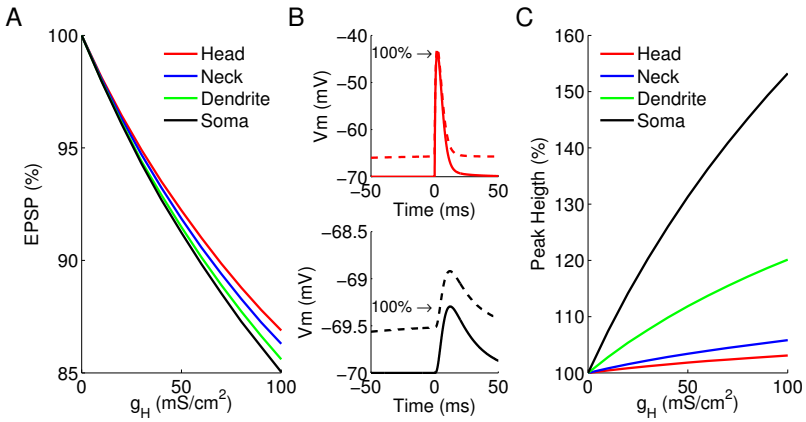

Figure 3.9. I_H on the spine reduces the EPSP amplitude (left panel) but increases the peak height (right panel) in all four recorded locations. **A**, the normalized amplitude of EPSPs measured at four locations, decreases as function of g_H. **B**, the dendritic (red) and somatic (black) EPSP traces for the scenarios with $g_H = 0$ (solid lines) and $g_H = 100$ mS/cm^2 (dashed lines). **C**, the normalized EPSPs peak heights measured at four locations, increases as function of g_H. For this figure, H conductance was only implemented on the spine (head and neck). This explains the smaller raise in resting membrane potential with high g_H at the soma.

sition could be considered if the I_M is only present closer to the synapse and the crossover effect is transferred to the spike generating-compartment. To test this idea, we simulated different channel distributions throughout the multi compartment model.

If I_H and I_M are only present on the spine (with $g_M = 35$ mS/cm^2), there is no significant difference to the previous scenario with I_H alone (Fig. 3.9C). The increase in g_H leads to higher EPSP peak in all locations and especially at the soma (Fig. 3.10A, EPSP peak increase of 153.2% with $g_H = 100$ mS/cm^2), due to the tonic increase in the resting membrane potential.

George et al. (2009) determined that the peak of the somatic

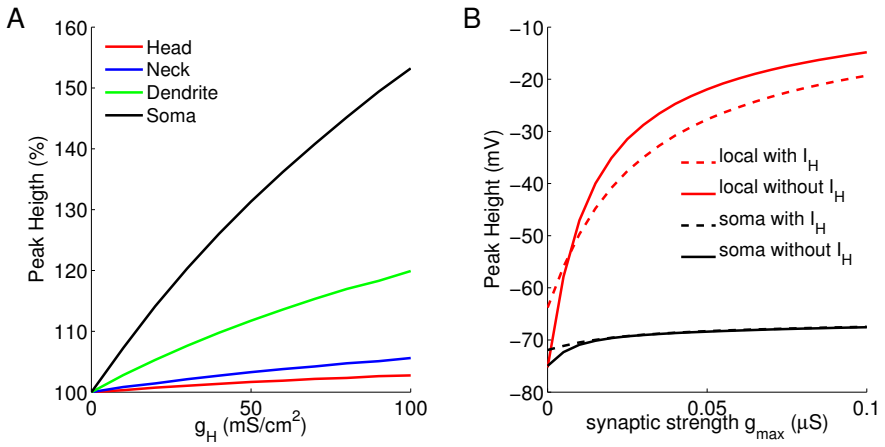

Figure 3.10. Presence of I_H and I_M increases the somatic EPSP peak height. **A**, EPSP peak height measured at four locations when I_H and I_M are present only in spine neck and head. Maintaing g_M constant, the increase of g_H results in larger depolarizations at spine, dendrites and soma. **B**, peak heights measured in a cell with constant I_M and variable I_H throughout the dendritic tree (tuft, #1, oblique and trunk) but not on the soma. The crossover effect obtained between conditions with I_H and withou I_H, which indicates a shunting outcome, is only observed where these currents are simultaneously present. There is a visible crossover at the site of input (local, red curves, −53.35 mV, 7.1 nS). However, this effect does not transfer to the soma - the curve without I_H (solid black) does not cross over the one with I_H. I_M was present with constant conductance $g_M = 35$ mS/cm^2.

post-synaptic potential decreases with g_H when both currents are present throughout the cell. With our model, we determined that if the currents are only present in the dendrites, there is no crossover effect at the soma (Fig. 3.10B). This conclusion is also obtained with the cable model used in their study (results not shown). Therefore, to decrease the somatic EPSP peak it is necessary to have an uniform presence of I_H and I_M at the synapse location in spines and

along the path to the soma. However, g_M has to be set at a very high magnitude, which, as proved above, completely inhibits the generation of action potentials.

These results demonstrate that the hypothesis of I_H and I_M interplay previously proposed has serious flaws when considered within a more biophysically realistic pyramidal cell model. Therefore, this could not be considered an acceptable explanation for the experimental results with the HCN blocker ZD7288.

3.4.4 I_M modulates cellular excitability in single neurons and working memory circuit

Even though the interaction between I_H and I_M has not been validated by our results, I_M may still play an important role in the gating of synaptic inputs. Recent unpublished results (A Arnsten's personal communication) show that blocking I_M clearly increases the excitability of the pyramidal cells tuned for the stimulus direction during a spatial working memory task. We simulated the effect of changing the conductance of I_M in the spine of our multi compartment model. By raising g_M we decreased the EPSP peaks recorded at the spine head, spine neck, dendrites and soma (Fig. 3.11A). The larger reductions were measured at the soma; with g_M of 10, 50, 100 mS/cm^2 the somatic EPSP peaks were 96.1%, 98.0% and 99.6% of the one with null g_M. (Fig. 3.11A).

A salient feature observed in simulations with the multi compartment model is that the filtering effect of I_M at the spine is more

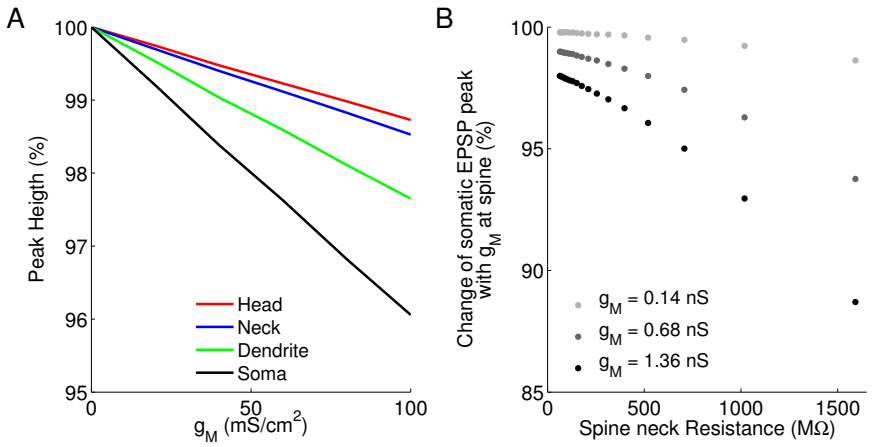

Figure 3.11. Increase of I_M and spine neck resistance reduces the EPSP peak at the soma **A**, EPSP peak height measured at four locations when I_M is present only in spine (neck and head). Raising g_M results in lower depolarizations at spine, dendrites and soma. For g_M = 10, 50 and 100 mS/cm^2 the somatic EPSP peaks (black line) are 99.6%, 98.0% and 96.1% of the scenario with no g_M, respectively. **B**, the filtering effect of I_M (shown in **A**) is potentiated by thin spine necks. Comparison of somatic EPSP peak reductions in simulations with different magnitudes of spine neck resistance and g_M. The resistance was set by changing the radius of the neck within a realistic range (0.02 – 0.1 μm). Given that this adjustment changes the area of the spine, we used absolute values of g_M, such that the magnitude of I_M is the same within each of the three data sets. M-conductances of 0.14, 0.68 and 1.36 nS correspond to specific g_M of 10, 50 and 100 mS/cm^2, respectively, in the total area of the standard spine (used in **A**, with neck radius of 0.035 μm and neck resistance of 519.7 MΩ). The most extensive EPSP reduction (11.3%) is achieved with the largest g_M (1.36 nS) and neck resistance (1591.5 MΩ).

effective with thin long necks. Fig. 3.11B shows how somatic EPSPs are further reduced by the combined effect of I_M and spine neck resistance. When the total g_M in the spine is 1.36 nS the reduction of the EPSP peak height ranges from 2.0% (neck resistance of 63.7 MΩ) to 11.3% (1591.5MΩ) (Fig. 3.11B, black data points). Smaller

absolute g_M magnitudes cause smaller EPSP reductions that are still dependent on the resistance of the spine neck (g_M= 0.14 nS, 0.2% to 1.4%, Fig. 3.11B, light gray; g_M= 0.68 nS, 1.0% to 6.2%, Fig. 3.11B, dark gray).

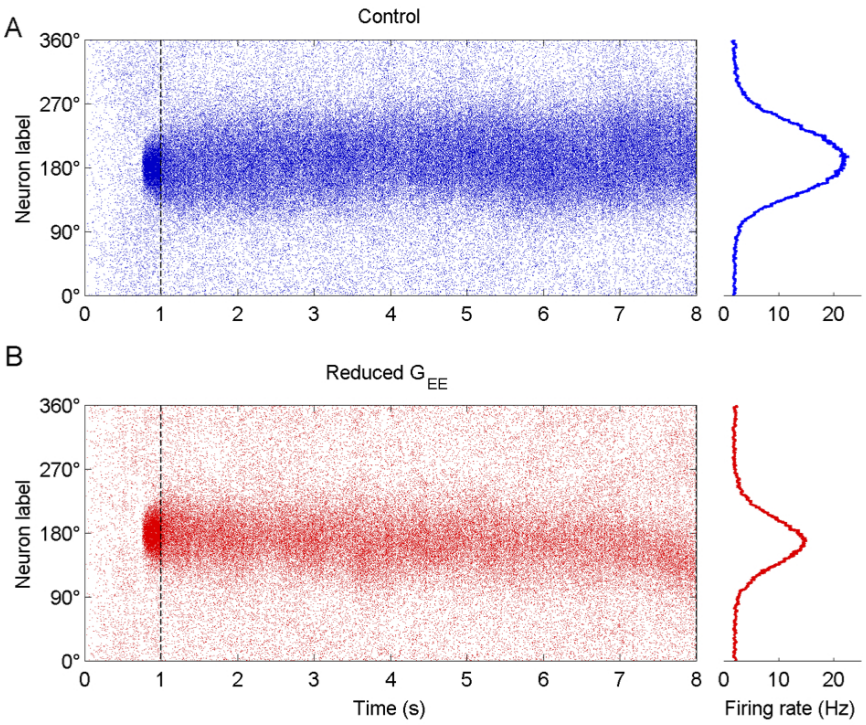

Figure 3.12. A small reduction in the excitatory drive can have a high impact on the persistent activity required to maintain information in a circuit. **A**, network rastergram with strong stable bump attractor (left panel) and the respective population profile during the delay period (right panel). **B**, network raster plot and population profile of a second simulation with 0.5% decrease in the recurrent excitatory conductance (G_{EE}) The maximum firing rate at the peak of the bump is significantly lower than in control.

While these small reductions in the synaptic input do not seem significant, they can have a critical effect when considered within

a neural circuit involved in persistent activity. These circuits comprise thousands of interconnected cells that continuously receive synaptic signals in its dendritic spines and perform the integration of that input in order to generate action potentials. We demonstrated the implications of the presence of I_M in a neural circuit with two approaches: either through a small reduction of the excitatory drive (G_{EE}) or through an increase in the total g_M available in each pyramidal cell. For both approaches, we employed our network model of spatial working memory.

In the first approach, we tested how a small filtering of synaptic input at the spine necks influences the activity at the network level. As shown before, the reductions in EPSP size can be less than 1% under certain conditions. In the network model, when the recurrent excitatory conductances between pyramidal cells (G_{EE}) were reduced by just 0.5%, the memory bump robustness and persistent firing rates weakened (Fig. 3.12B) compared to the control simulation (Fig. 3.12A). This is clearly visible in the population profiles averaged over the delay period. If G_{EE} is further reduced, the bump will lose stability and the memory will disappear (not shown).

In the alternative approach to test the role of I_M in the spatial working memory network, we increased g_M in each pyramidal excitatory cell, to the absolute values tested in the multi compartment model. When g_H is set to 0.68 nS, the action potentials generated by each cell during the delay period are slightly reduced (Fig. 3.13B), compared to the control conditions (Fig. 3.13A). If we increase g_M to 1.36 nS the persistent activity collapses, as shown in some exam-

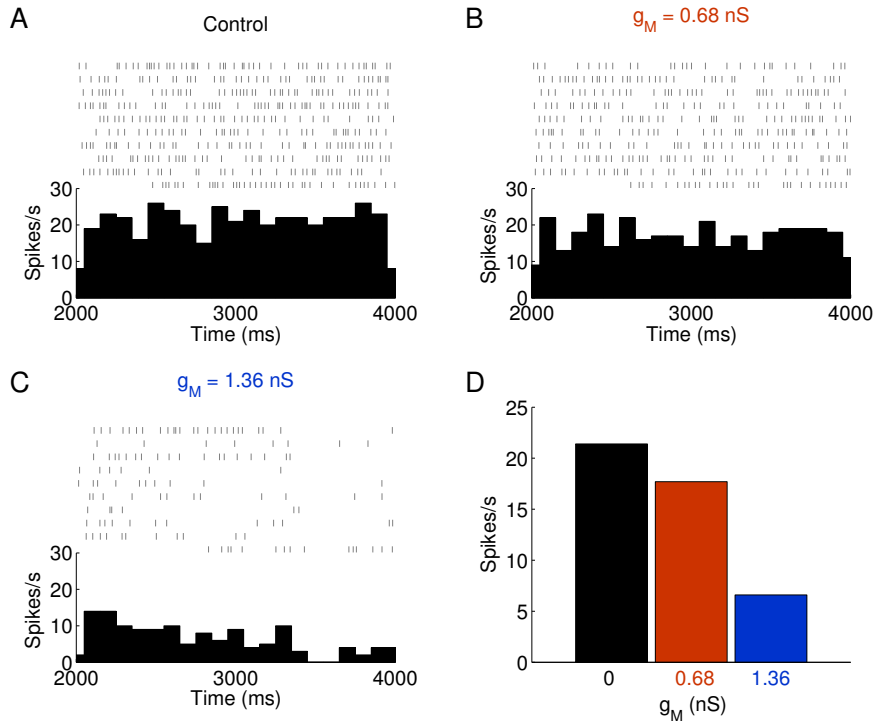

Figure 3.13. Persistent activity during a spatial working memory task depends on the magnitude of I_M in pyramidal cells of the network model. Rastergrams in the upper panels of **A**, **B** and **C** show the spike times of 10 individual cells in the center of the received stimulus cue location. The lower panels represent the instant average firing rate for those cells in each condition. When a small g_M (0.68 nS) is added to the network (**B**), the persistent firing of the preferred neurons decreases compared to those in the control network (**A**, g_M= 0 nS). If the M-conductance is further increased (**C**, 1.36 nS), the spiking of single neurons decreases substantially and the persistent activity of the network stops. **D**, the overall firing rates averaged across time are 21.4 Hz, 17.7 Hz and 6.6 Hz for M-conductance of 0 nS, 0.68 nS and 1.36 nS, respectively.

ples of Fig. 3.13C (upper panel). The average firing rates of each condition summarize the effect of I_M (Fig. 3.13D).

These results demonstrate that I_M is a powerful mechanism to

control the signal transfer and excitability within a single neuron. Moreover, when those effects are considered at the circuit level, they have the power to modulate the overall persistent activity and network readout.

3.5 Discussion

Two studies have shown that the blockage of HCN channels with ZD7288 increased the excitability of pyramidal cell of the PFC during a working memory task (Wang et al. 2007) and during Up states recorded in cortical slice preparation (Shu et al, unpublished observations). In this research project, we tested these ideas in compartment models, of different geometries, containing I_H. We determined, contrary to the commonly accepted assumption, that I_H is a mostly depolarizing current and that, when it is blocked, the neuron fires less action potentials. We also rejected the hypothesis that I_H interacts with the M-type potassium current (George et al. 2009). Nevertheless, we explored the effect of I_M in the neural excitability and found that it could act as a potent modulator of the working memory function. We found that thin long spines are the ideal structures for the electrical filtering to occur due to the large axial resistance of the spine neck.

3.5.1 I_H depolarizes membrane potential and increases excitability

The interpretation that I_H would decrease neural firing rates (Wang et al. 2007) was supported by previous studies that suggest that this current decreases neural excitability (Poolos et al. 2002; Shah et al. 2004; Fan et al. 2005; Rosenkranz and Johnston 2006; Kole et al. 2007; Jung et al. 2007). A main argument for this proposition is that I_H decreases the temporal summation of

a train of EPSPs (Magee 1998; Magee 1999; Williams and Stuart 2000; Berger et al. 2001; Angelo et al. 2007; Vaidya and Johnston 2013). This phasic phenomenon is explained by the decrease in input resistance driven by the opening of HCN channels. However, I_H is associated with a tonic property of opposing effect: it depolarizes the membrane potential during rest. This elevates the "baseline" V_m upon which synaptic EPSPs are added. The tonic effect is widely recognized in studies of pacemaking in cardiac cells (DiFrancesco 1993; Clapham 1998).

A technical aspect of some experimental slice recording papers that lead to the misrepresentation of I_H function is the adjustment of baseline membrane potential by injected current, regardless of the g_H magnitude. This methodology allows for the comparison of the size of EPSPs between conditions but effectively removes the tonic effect of I_H. If we consider a cell in a living organism, the generation of action potentials occurs when the membrane potential crosses a given threshold, regardless of how it accumulated. Therefore, the tonic contribution of I_H is an important factor that can not be discarded. For these reasons, in our study, we considered the peak height of the EPSP as a better measure to explain I_H than the EPSP amplitude. Our results lead us to conclude that the presence of I_H in spines and dendrites increases the somatic EPSP peak and thus contributes to the depolarization of the cell and not the opposite. We were able to explain this argument in more detail when we compared the magnitude of both components of I_H separately. We found that the tonic depolarization overcame

the shunting properties of the phasic effect, which resulted in an inward, depolarizing net current over the range of V_m relevant to the generation of action potentials.

3.5.2 I_M has a relevant role in working memory but does not interact with I_H

Similar conclusions regarding the depolarizing nature of I_H were recently published (George et al. 2009). This study proposed that an interaction between I_M and I_H is responsible for the effects of ZD7288 in neurons. In this work, we found that, while compelling, this explanation has serious flaws. Firstly, it absolutely requires the presence of both currents along the path between synapse and action potential-initiating region. Otherwise the shunting effect becomes subdued by the tonic effect of I_H. Secondly, the M-conductance that is required throughout the cell to obtain the crossover effect is too high and severely inhibits firing of action potentials.

Even though I_M does not help to explain experimental I_H results, it has a set of properties that can play a role in the control of persistent activity associated with working memory. It is an outward current mediated by KCNQ channels, it activates at subthreshold voltages, has slow time scale and does not inactivate. I_M has been shown to prevent repetitive neural firing (Pan et al. 2006), and control bursting in cortical neurons (Wang 1999a; Santini and Porter 2010). Furthermore, the activity of I_M is regulated by several modulatory pathways, including inhibition through stimulation

of muscarinic receptors (Delmas and Brown 2005; Cooper and Jan 2003).

We showed that the presence of I_M in the spine neck alone, decreases the size of the EPSPs that reaches the dendritic brach. This increase in filtering does not require the interaction of I_H nor a high g_H conductance close to the soma. However, it depends on the spine neck resistance. Thiner and narrower necks create a stronger barrier, in which I_M filtering is more effective. We determined a range of 0.2 to 11.3% reduction in the EPSP size in these conditions. While the magnitude of this effect seems small, it has significant consequences at the network level. When we reduced the excitatory recurrent conductances of the network model by a similar amount, we observed a decline in the persistent activity and on the memory robustness. Separately, raising g_M in the network model also leads to a decrease in the firing rate of neurons. These results show the importance of I_M in working memory function.

3.5.3 Neck resistance significantly increases electrical compartmentalization of spine

It is currently accepted that dendritic spines can act as biochemical compartments (Muller and Connor 1991; Yuste and Denk 1995; Sabatini and Svoboda 2000). However, the degree at which these structures can be electrically compartmentalized from the rest of the cell is controversial. The reported electrical attenuation from the spine head to the dendrites ranges from approximately 50% (Araya

et al. 2006) to just 15% (Palmer and Stuart 2009). One reason for this uncertainty is the difficulty in obtaining reliable recordings of the membrane potential in spines.

Our multi compartment model included a spine, which is considered to be crucial for the gating of synaptic inputs in pyramidal cells during persistent activity (Wang et al. 2007; Arnsten et al. 2010). The constriction of the spine neck radius leads to the increase in the spine neck resistance. By changing the radius from 0.1 to 0.02 μm, we decreased the EPSP size at the soma and dendrites by approximately 50%. However, we chose to use a value of 0.035 μm. The reason for this choice was twofold. First, that is the average neck radius of HCN-immunoreactive spines in layers II/III of the PFC, measured by our collaborators (Paspalas et al. 2013). Second, that measurement results in a total spine neck resistance of 519.7 MΩ, which is in line with previous studies (Palmer and Stuart 2009; Grunditz et al. 2008), even though an experimental study has shown that it can reach up to 1 GΩ (Bloodgood and Sabatini 2005).

3.5.4 Complete mechanism of ZD7288-related increase in excitability is still unknown

In this study, we were able to characterize the physiological function of I_H in neurons. However, the increase in excitability of pyramidal cells after pharmacological application of the compound ZD7288 can not be explained through a modulation of only the HCN

channels present in pyramidal cells. In order to understand these results, we will need to consider additional cellular mechanisms that may also be affected by the action of this HCN antagonist.

Chapter 4

A novel understanding of I_H function

4.1 Abstract

Ion channels play a key role in the integration of synaptic inputs that lead to the generation of action potentials. In order to understand these cellular processes it is necessary to obtain a clear physiological understanding of the currents mediated by these channels. According to our previous results, the nonselective hyperpolarized-activated current I_H promotes the depolarization of the membrane potential and significantly increases the action potential firing. This finding is at odds with experimental studies that showed that a downregulation of I_H, with the blocker ZD7288, elevates the firing rate of cortical pyramidal cells. These results were obtained in a variety of experimental procedures, which included a spatial working memory task with behaving monkeys and a ferret brain slice preparation that exhibits slow oscillatory behavior. We propose two alternative hypotheses that reconcile out theoretical findings with the experimental results, at a circuit level. The first, assumes the incorporation of an additional hyperpolarizing current, which should also be mediated by ZD7288-sensitive channels. The second hypothesis is based on presence of I_H in interneurons and the resulting implications on the excitability of pyramidal cells. We test these hypotheses in network models that simulate a PFC circuit during a spatial working memory task and in a network that exhibits slow Up and Down states. We found that both propositions are able to qualitatively account for the main experimental observations.

4.2 Introduction

The performance of neural circuits in the prefrontal cortex is determined by the cellular properties of its neurons. These cells receive constant input from thousands of synapses located on their dendrites. The stimulation patterns are then processed on the dendritic branches and reach the soma where action potentials are generated (Spruston 2008). The active currents mediated by channels present on the cell membrane are essential for this integration (Sjostrom et al. 2008). In order to comprehend and predict the input-output relation of neurons, it is crucial to understand the properties and physiological function of these currents.

The H-current (I_H) is carried by HCN channels that are expressed in several cell types (Notomi and Shigemoto 2004). These channels are activated by membrane depolarization, are permeable to sodium and potassium ions and their activation is facilitated by cAMP (Biel et al. 2009). I_H decreases the temporal summation of distal dendritic inputs that reach the soma (Magee 1998; Magee 1999; Williams and Stuart 2000; Berger et al. 2001; Vaidya and Johnston 2013). Several studies have found evidence that cellular excitability is inversely correlated with the activation of I_H (Poolos et al. 2002; Shah et al. 2004; Fan et al. 2005; Rosenkranz and Johnston 2006; Kole et al. 2007; Jung et al. 2007). Similar conclusions were obtained by our collaborators in studies of spatial working memory (Wang et al. 2007) and slow Up and Down states (Shu et al. unpublished observations). In both experimental procedures, pyramidal cells increased their firing after administration of

the HCN antagonist ZD7288.

In previous work (described in chapter 3) we demonstrated that, contrary to most views, I_H is a purely depolarizing current and should contribute to neural excitability. Accordingly, a downregulation of I_H should lead to less action potentials being generated. However, the previously mentioned experimental evidence is too reliable and consistent to be neglected. What is the missing link between I_H function and the blockage of HCN channels with ZD7288 that explains the experimental changes in excitability of the pyramidal cells?

A recent modeling paper proposed an hypothesis that accounted for some of these results (Migliore and Migliore 2012). In this study the depolarizing tonic effect of I_H is counteracted by a hyperpolarizing current. This current is still a theoretical proposition and the channel that mediates if has not been identified yet. Nevertheless, potential candidates must be voltage-independent and have a constant conductance that is proportional to the maximum conductance of I_H. With this framework they were able to replicate results of EPSP temporal summation (Magee 1999) and the reduction in firing when I_H is upregulated with the anti convulsive drug Lamotrigine (Poolos et al. 2002).

An alternative explanation for the effects of I_H on neural excitability may rely on the expression of HCN channels, not only in pyramidal cells, but also in interneurons (Maccaferri and McBain 1996; Kawaguchi and Kubota 1997; Lupica et al. 2001; Notomi and Shigemoto 2004; Wang et al. 2004; Aponte et al. 2006; Hughes

et al. 2013). This is a well-known and accepted observation but has lead to fewer research studies than the ones on pyramidal cells. The existence of I_H in interneurons suggests that ZD7288 application should hyperpolarize and silence these cells. The resulting disinhibition of pyramidal cells should lead to an augmentation of action potentials, as seen in experiments.

We tested both these hypotheses in two network models that replicate the circuit properties investigated by our collaborators: the spatial working memory model previously described and a model that exhibits slow oscillations (Sanchez-Vives and McCormick 2000; Compte et al. 2003). We incorporated I_H in both pyramidal cells and interneurons and included a version of the hyperpolarizing current (I_{HL}) proposed by Migliore and Migliore (2012). We found that I_H in interneurons and the interplay of I_H with I_{HL} could provide qualitative explanations for the experimental results.

4.3 Materials and Methods

4.3.1 Network model with slow oscillatory activity

To study the influence of I_H in the generation and rhythm of Up and Down states, we adapted a network model that exhibits oscillatory activity (Compte et al. 2003). This model has a excitatory population of 1024 pyramidal cells and an inhibitory population of 256 interneurons. The neurons are equidistantly distributed on a line and interconnected through biologically plausible synaptic dynamics.

Each pyramidal cell in the network has a somatic and a dendritic compartment (Pinsky and Rinzel 1994). The group of channels that was included in each compartment was found in cortical pyramidal cells. The soma contains the following currents: fast sodium I_{Na}, delayed rectifier potassium I_K, leak I_L, fast A-type K^+ I_A, non-inactivating slow K^+ I_{KS} and a Na^+-dependent K^+ I_{KNa}. The dendrite has a high-threshold Ca^{2+} current I_{Ca}, a Ca^{2+}-dependent K^+-current I_{KCa}, a non-inactivating (persistent) Na^+ current I_{NaP}, an inward rectifier (activated by hyperpolarization) non-inactivating K^+ current I_{AR}, an hyperpolarized-activated nonselective current I_H and an additional leak-like current, I_{HL}. The dynamical equations for the somatic voltage (V_s) and the dendritic voltage (V_d) are:

$$C_m A_s \frac{dV_s}{dt} = -A_s(I_L + I_{Na} + I_K + I_A + I_{KS} + I_{KNa}) - g_{sd}(V_s - V_d) - I_{syn,s}$$

$$C_m A_d \frac{dV_d}{dt} = -A_d(I_{Ca}+I_{KCa}+I_{NaP}+I_{AR}+I_H+I_{HL})-g_{sd}(V_d-V_s)-I_{syn,d}$$

with the membrane capacitance $C_m = 1\ \mu F/cm^2$ and the areas being $A_s = 0.015\ mm^2$ and $A_d = 0.035\ mm^2$ for the soma and dendrite, respectively. The coupling between soma and dendrite is determined by $g_{sd} = 1.75 \pm 0.1\ \mu S$ (axial resistance 0.57 MΩ, standard deviation indicates the degree to which this parameter is randomly varied from cell to cell). $I_{syn,s}$ and $I_{syn,d}$ are the synaptic currents impinging on the soma and dendrites, respectively. In our simulations, all excitatory synapses target the dendritic compartment and all inhibitory synapses are localized on the somatic compartment of postsynaptic pyramidal neurons.

Interneurons are modeled with I_{Na}, I_K, I_L, I_H and I_{HL}, in their single compartment:

$$C_m A_i \frac{dV_i}{dt} = -A_i(I_L + I_{Na} + I_K + I_H + I_{HL}) - I_{syn,i}$$

with the total neural surface area being $A_i = 0.02\ mm^2$.

I_H is modeled according to the description in section 3.3.3. I_{HL} is described below. The parameters and equations used for the remaining ionic currents, synapses and cortical network connectivity were the same as previously published (Compte et al. 2003), except the following modifications, which are required to obtain similar results when the model is implemented with the Brian simulator and python programming language (Taxidis et al. 2013). Whenever a

presynaptic spike is detected (with detection threshold at 10 mV for the membrane potential of the presynaptic cell) a fixed instantaneous increase is given in the postsynaptic cell's synaptic conductance. This increase is set to be 1/3 of the corresponding parameter α_{syn} in Compte et al. (2003) for excitatory connections and 1/2 for inhibitory ones. In the original model each synapse in a cell is modeled by an independent post-synaptic variable, whereas in this implementation each cell has one total variable for each synaptic type. This required an adjustment of the overall excitation by reducing the maximal excitatory conductances of the original model. The pyramidal-to-pyramidal AMPA and NMDA synapses were set to 4.15 nS and 0.225 nS, respectively. The pyramidal-to-interneuron AMPA and NMDA synapses were adjusted to 0.5 nS and 0.11 nS, respectively. Additionally, the GABA reversal potential was reduced from -70 to -75 mV to enhance inhibition. Finally, the maximum sodium-dependent potassium conductance g_{KNa}, in the dendritic compartment of cortical pyramidal cells was reduced to 0.5 mS/cm^2. This was done to increase the excitability of pyramidal cells, prolonging (shortening) the duration of Up (Down) states (Taxidis et al. 2013). With these modifications, the network reproduces all the basic characteristic properties of Compte et al. (2003). The slow oscillations are a result of the interplay between all currents included in the model. I_{KNa} plays a key role in determining the end of Up states and transition to Down state (Fig. 4.1).

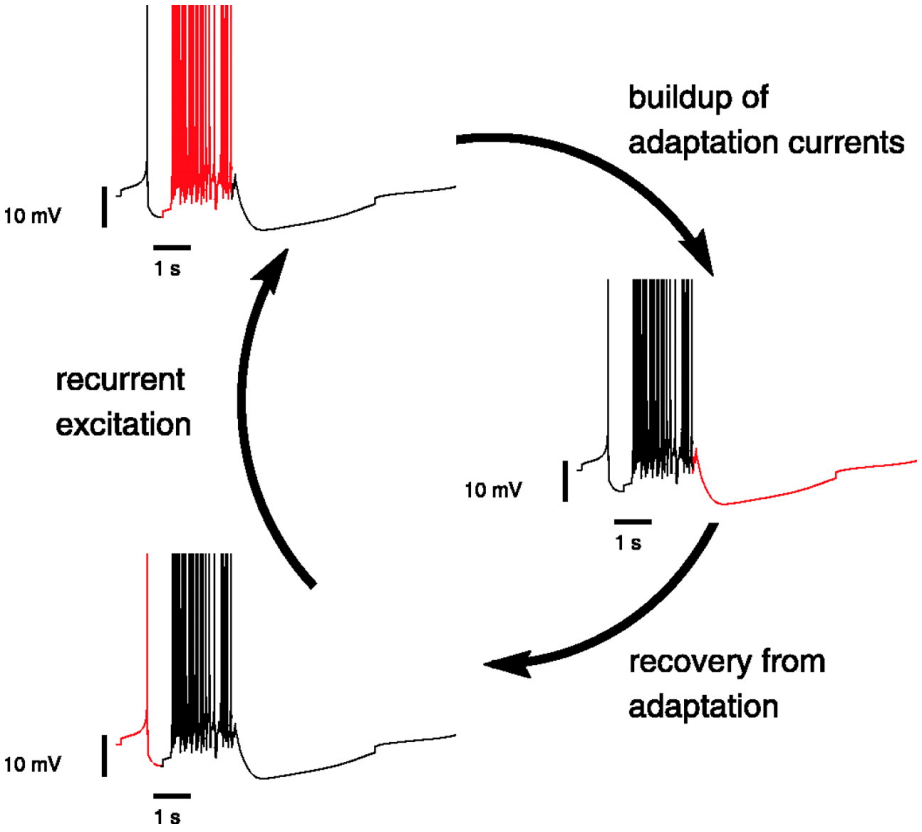

Figure 4.1. Mechanism of the slow oscillation: some neurons have slightly lower spiking threshold and fire spontaneously (bottom left). This spontaneous firing will occasionally trigger the recruitment of all the cells in a subregion of the network through recurrent excitation and bring those cells up into the firing state (top left). While neurons fire, their activity-dependent K^+ currents (especially I_{KNa}) accumulate slowly. A point is reached in which the neurons are not excitable enough to maintain this self-sustained spiking state and they revert to the silent mode (middle right). Only after the Na^+-dependent K^+ current decays can the spontaneous firing resume and eventually trigger a new discharge episode (bottom left). Adapted from Compte et al. (2003).

4.3.2 Network model of spatial working memory

The working memory results presented in this chapter were obtained with the spiking network model for the oculomotor delayed-response (ODR) task, previously described (Compte et al. 2000).The model consists of a population of excitatory pyramidal cells and a population of inhibitory interneurons. Pyramidal cells are arranged in a ring-like fashion and labeled by their preferred cue direction, from 0 to 360 degrees.

Both pyramidal cells and interneurons are modeled as leaky integrate and fire units (Tuckwell 1988). Each type of cell is characterized by total capacitance C_m, total leak conductance g_L, leak reversal potential V_L, threshold potential V_{th}, reset potential V_{res} and refractory time τ_{ref}. The values that we use in the simulations are $C_m = 0.5$ nF, $g_L = 25$ nS, $V_L = -70$ mV, $V_{th} = -50$ mV, $V_{res} = -60$ mV, and $\tau_{ref} = 2$ ms for pyramidal cells; and $C_m = 0.2$ nF, $g_L = 20$ nS, $V_L = -70$ mV, $V_{th} = -50$ mV, $V_{res} = -60$ mV, and $\tau_{ref} = 1$ ms for interneurons. The subthreshold membrane potential, V_m, follows:

$$C_m \frac{dV_m}{dt} = -g_L(V_m - V_L) - I_{ion} - I_{syn}$$

where I_{ion} is the sum of the ionic currents and I_{syn} is the total synaptic current to the cell.

The specifications for synaptic interactions, network connectivity and stimulus input are the same as described in sections 2.3.2,

2.3.3 and 2.3.4, respectively.

4.3.3 I_{HL}, a ZD7288-sensitive leak current

I_{HL} is not dependent on voltage but its magnitude is correlated with the maximum conductance of I_H:

$$I_{HL} = g_H l(V_m - V_L)$$

where l is a voltage- and time-independent parameter (Migliore and Migliore 2012) and was set to 0, except when noted.

4.3.4 Simulation method

The network models were written in python language in the Brian simulator (Goodman and Brette 2009). The equations were integrated using a second-order Runge-Kutta algorithm (timestep = 0.02 ms). The simulations were carried out in the cluster facilities of the Yale University Biomedical High Performance Computing Center.

4.4 Results

4.4.1 Network model simulates slow oscillations

Our adapted implementation of the network model with slow oscillatory activity reproduces the basic properties of the one previously published (Compte et al. 2003). In the control conditions, the alternating Up and Down states have a frequency of less than 1 Hz (Fig. 4.2). The somatic membrane potential of some excitatory cells exhibits clearly visible hyperpolarized Down states punctuated by elevated Up states, which sustain repeated action potentials (Fig. 4.2, lower panel). The spike timing of the populations of pyramidal cells (Fig. 4.2, upper panel) and interneurons (Fig. 4.2, middle panel) is highly synchronized throughout the simulation, as seen in experimental recordings. The number of generated action potentials during Up states is 5.6±1.4 Hz for pyramidal cells and 11.0±1.6 Hz for interneurons.

4.4.2 Slow oscillatory model is influenced by channel repertoire

I_H increases excitability of the network model

Next, we tested how the incorporation of I_H in pyramidal cells would affect the output of the network model. This simulates the opposite of applying the HCN blocker ZD7288. In this scenario, the network will lose the slow oscillatory output and the neurons will fire repetitively (Fig. 4.3). The activation of I_H depolarizes the

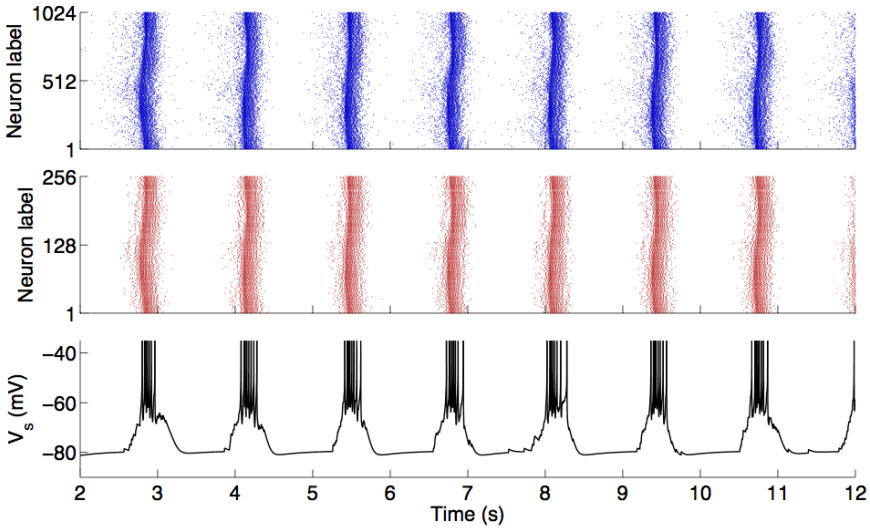

Figure 4.2. The network model reproduces the slow Up and Down states recorded in experiments. The firing of pyramidal cells (upper panel) and interneurons (middle panel) is synchronized in time. The membrane potential trace of the somatic compartment of a pyramidal cell in the network shows the hyperpolarization of the resting V_m during silent Down states intercalated with depolarized Up states that exhibit action potentials.

resting membrane potential (baseline V_m at approximately -72 mV in Fig. 4.3, lower panel, compared to -80 mV in Fig. 4.2), which promotes the generation of action potentials. These results confirm, in a circuit model, our previous findings from compartment models of single cells (chapter 3). Namely, that I_H increases the excitability of pyramidal cells of the PFC.

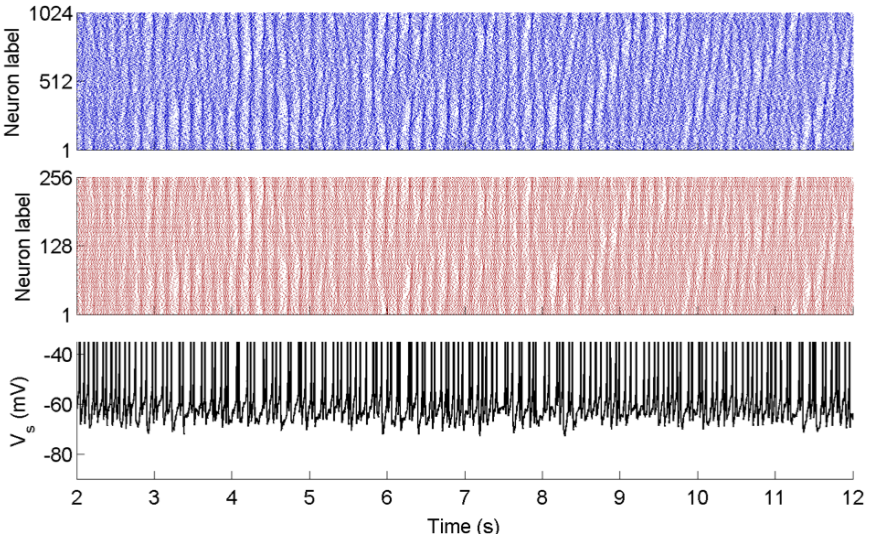

Figure 4.3. Incorporation of I_H raises resting V_m and the excitability of all neurons in the model, disrupting oscillations. The membrane potential depolarizes with the presence of I_H (lower panel). Both pyramidal cells (upper panel) and interneurons (lower panel) increase their firing activity. I_H was incorporated with a conductance of 0.1 mS/cm^2.

Simultaneous blockage of I_H and I_{HL} explains main effects of ZD7288

According to a recent study, (Migliore and Migliore 2012), the effects of ZD7288 in the excitability of pyramidal cells could be explained with the interplay of I_H with an hyperpolarizing current. We modeled this current (I_{HL}) with the reversal potential of the leak (-70 mV) and a conductance that depends on g_H. This last setting arises from the assumption that I_{HL} is mediated by channels that are also blocked by ZD7288. Therefore when I_H is blocked, so is this current.

Based on our simulations, the presence of I_H and I_{HL} in pyrami-

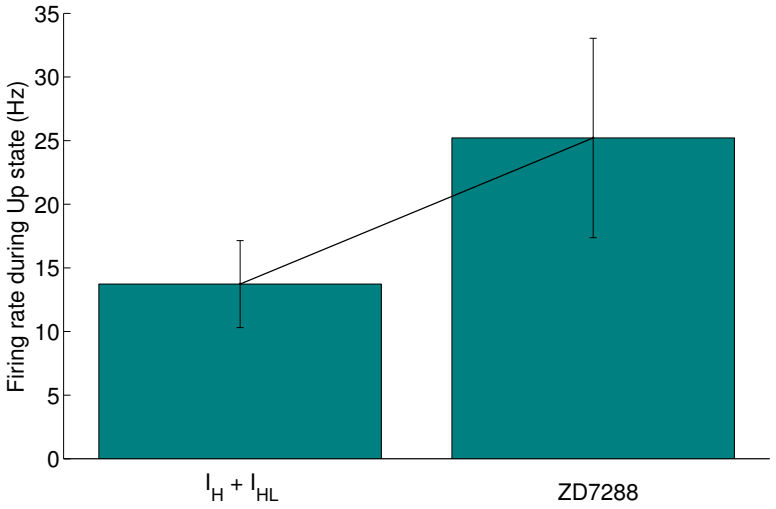

Figure 4.4. Simultaneous blockage of I_H and I_{HL} channels increases excitability. The firing rate of pyramidal cells during the Up states was increased from 13.7±3.4 Hz in a network with I_H and I_{HL} (g_H) to 25.2±7.8 Hz when those currents were blocked (ZD7288). In the I_H+ I_{HL} condition, g_H was set to 0.1 mS/cm^2 and l = 0.25, which results in a I_{HL} conductance that corresponds to 25% of g_H.

dal cells results in firing rates of 13.7±3.4 Hz in these cells during Up states (Fig. 4.4). In order to replicate the experimental results of the pharmacological blockage of HCN channels (and I_{HL} channels) we considered the network without I_H nor I_{HL} (conditions of Fig. 4.2). This leads to an increase in the firing rate of pyramidal cells to 25.2±7.8 Hz (Fig. 4.4). This increase in the frequency of action potentials during Up states is consistent with what was recorded in experiments (Shu et al. unpublished observations). Moreover, similar to what was reported in that study, the membrane potential during the Down states also decreases from approximately −62

mV with I_H and I_{HL} to −80 mV in the ZD7288-like simulations. A feature that is not significantly accounted for our model is the increase in the Up states duration with ZD7288 blockage. Our results show that Up states lasted identical periods (g_H, 0.26±0.05 seconds; ZD7288, 0.25±0.11 seconds) in conditions with and without I_H.

4.4.3 I_H in interneurons determines the working memory-related persistent activity

A major motivation for the study of I_H arose from the repercussions of its manipulation in a spatial working memory study. More specifically, why blocking HCN channels with ZD7288 elevates the firing activity of pyramidal cells of the prefrontal cortex during an ODR task (Wang et al. 2007)? An alternative explanation for the increase in firing rates with HCN antagonist is inspired by the presence of HCN channels in interneurons. This evidence allowed us to hypothesize that the application of ZD7288 in the PFC could affect local interneurons to a significant degree. According to our findings in the previous chapter, I_H increases excitability in neurons. Therefore, a blockage oh I_H would result in a decreased activity of interneurons and, consequently, a disinhibition of the pyramidal cells that establish connections with them.

In order to address this hypothesis, we incorporated modifications to our working memory model, which is designed to simulate an ODR task. Briefly, this task proceeds from cue (angle) presentation, to a delay period and finally to a memory-guided behavioral

response. In the model, the cue input activates a group of pyramidal neurons with preferred directions around the cue location. If the firing rate of this subpopulation of neurons is sufficiently elevated and mutual excitation among them is strong enough, reverberation can give rise to self-sustained persistent activity after the stimulus offset. This creates a memory bump that represents the cue during the delay period. The persistent activity by pyramidal cells is controlled by unspecific inhibition provided by the population of interneurons. If the activity of these inhibitory cells is too large, the persistent activity will not be sustainable.

To address the relevance of I_H in interneurons in working memory circuits, this current was included in the cells of both populations (excitatory and inhibitory) of our network model. We ran a set of spatial working memory simulation trials, using different magnitudes of H-conductance in interneurons and pyramidal cells. At the end of the delay, it was determined whether the system was in the spontaneous or in the memory states. These two possible outcomes of the network fell on distinct regions of the parameter space. In general, simulations that maintained memories had a higher distributions of g_H in pyramidal cells than interneurons (Fig. 4.5, red shaded area). On the other hand, a bigger presence of g_H in interneurons, resulted in failed memorizations (Fig. 4.5, gray shaded area).

The presence of I_H in both cell types, however, did not produce totally symmetrical results (Fig. 4.5, dashed line). Across almost all range it was necessary to have more g_H in pyramidal cells than

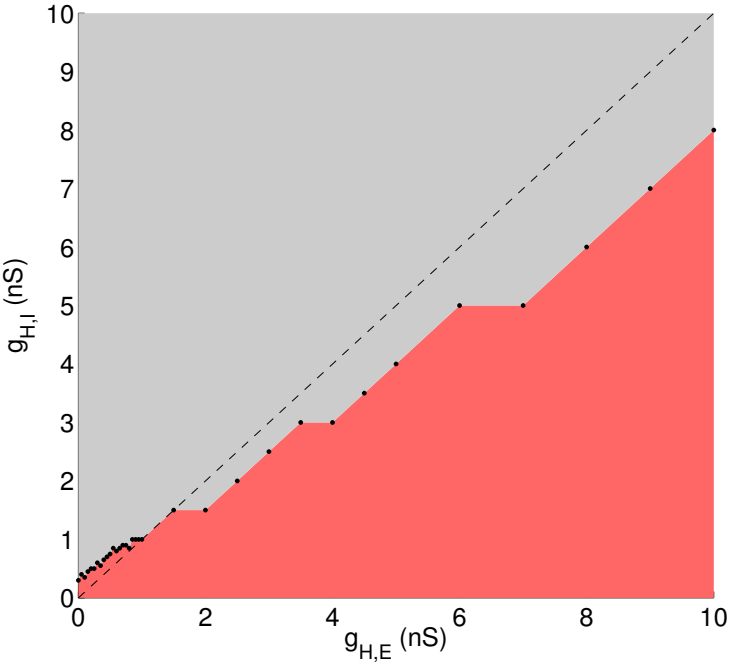

Figure 4.5. The performance of working memory in a PFC circuit depends on the magnitude of I_H in pyramidal cells and interneurons. A 2-d analysis of the dynamical state of the network model in respect to g_H in pyramidal cells ($g_{H,E}$) and in interneurons ($g_{H,I}$). The shaded regions correspond to subsets of the parameter space where the network was able to keep a memory through persistent activity (red) or remained in the spontaneous baseline state (gray).

interneurons in order to have working memory sustained by persistent activity. The opposite was only observed for lower conductances in the two populations. This break from symmetry could be crucial to understand the blockage by ZD7288. Assuming that this HCN antagonist binds equally to channels in both cell types, the resulting decrease in H-conductance shifts the system to the region where persistent activity is more immune to the presence of

I_H in interneurons. This result could explain why the application of ZD7288 increases the firing rate of pyramidal cells during working memory performance.

4.5 Discussion

The pharmacological application of the HCN channel antagonist ZD7288, leads to a consistent elevation of pyramidal cell excitability in electrophysiological recordings in working memory (Wang et al. 2007) and slow oscillatory (Shu et al. unpublished observations) studies. However, as reported in the previous chapter, the HCN-mediated current I_H has a depolarizing effect on the somatic resting membrane potential that induces an increase in the generation of action potentials. To provide an explanation for these two apparently contradictory findings, we proposed two alternative hypotheses and tested them in distinct network models. The ZD7288 may increase the neural excitability of pyramidal cells due to the interplay between I_H and an hyperpolarizing current I_{HL}, or because it blocks HCN channels that are present in interneurons.

The first of those hypotheses was influenced by a recent study that proposes the existence of an I_H-dependent hyperpolarizing current (Migliore and Migliore 2012). The conductance of this current is correlated with g_H, such that the application of ZD7288 blocks both I_H and I_{HL}. When this interplay was studied in single cell models it accounted for experimental results at the cellular level (Migliore and Migliore 2012). We took this hypothesis one step further and implemented I_H and I_{HL} in a network model of slow Up and Down states (Compte et al. 2003). We found that the firing rates of pyramidal cells during Up states increased when the network lost the presence of I_H and I_{HL}, mimicking the the effect of ZD7288 in experiments (Shu et al. unpublished observations). This hypothesis

accounts for the modulation of excitability in a way that is only dependent on g_H. In conditions where this conductance is large, I_{HL} is also very active and overcomes the depolarizing effect of I_H. When g_H is blocked by ZD7288, I_{HL} is equally reduced. Even though this mechanism provides a qualitative explanation for a physiological result, the identity of this current and the channels that carry it are still undetermined.

The second hypothesis put forward in this project considers the presence of HCN channels in interneurons (Maccaferri and McBain 1996; Kawaguchi and Kubota 1997; Lupica et al. 2001; Notomi and Shigemoto 2004; Aponte et al. 2006; Hughes et al. 2013). This proposition assumes that the local application of ZD7288 to a region of the PFC may affect, not only pyramidal cells, but also local inhibitory neurons. This is likely because cortical neurons are densely distributed and the pharmacological administration of an antagonist should reach all cells in the targeted area. We tested this hypothesis in the spatial working memory network, by incorporating I_H in both populations of neurons. Lowering I_H leads to less depolarization and decreased cellular excitability in the interneurons. The resulting disinhibition of pyramidal cells should promote an increase in their firing. However, the HCN channels of pyramidal cells should also be blocked, which causes the opposite effect. To determine which effect is stronger, we performed a 2-d analysis with a range of g_H in both cell types. We found that when the combined conductances are similarly reduced, as should happen with ZD7288, the system evolves to a region of the parameter space where per-

sistent activity is sustainable and working memory can be encoded. These findings are in accordance with the data from (Wang et al. 2007) and may explain the improvement of working function when I_H is blocked.

Although these two alternative hypotheses were tested in different models, there is no evidence to suggests that the blockage of and I_H and I_{HL} would not increase the persistent firing in the spatial working memory model. Likewise, we are lead to believe that the blockage of I_H present in interneurons of a slow oscillatory network would increase the generation of action potentials during the Up states. Further modeling analysis is required to fully test these assumptions.

These two hypotheses can successfully explain how an I_H blocker may increase the excitability of pyramidal neurons. Moreover, they provide testable predictions regarding the currently unknown mechanisms. A combination of iontophoresis, electrophysiology and microscopy experiments could test the range of a ZD7288 application and record the membrane potential from interneurons. Moreover, the precise characterization of the HCN subunits in these interneurons would be particularly relevant. If they differ from those in pyramidal cells, specific antagonists could block them differentially. This would allow the results of our 2-d analysis to be replicated in experiments and to infer the importance of interneurons in the overall network activity. Similarly, it would be relevant to test the presence of a current with the properties of I_{HL} in pyramidal cells, namely being mediated by ZD7288-sensitive channels and having a

low reversal potential.

Our theoretical approach based on experimental data contributed to unravel the role of I_H in the excitability of pyramidal cells in the context of working memory. This current has a strong modulatory effect, influences some of the most relevant cognitive functions in the prefrontal cortex and a complete characterization of its function would make a relevant contribution to the understanding of brain activity.

Chapter 5

Concluding remarks

As demonstrated in the previous chapters, a common theme in the planning and execution of the work described in this dissertation was to make the functional connection between biophysical processes, neural network performance and ultimately behavior. The cellular and synaptic processes that were studied influence circuit dynamics and cognitive functions. While diverse in nature, they are part of the global neural apparatus that gives rise to cognition in the brain. In this work, we focused on the working memory function as seen through the paradigm of the oculomotor delayed-response task. According to the currently accepted framework, the basis for this cognitive function lies in neural circuits of the prefrontal cortex that store and maintain information through persistent activity sustained by recurrent excitation between pyramidal cells. This concept depends on the excitability of these neurons, i.e., the ability to generate action potentials from the synaptic signals they receive. Therefore, any mechanism that affects this input-output

transfer is highly relevant to working memory performance.

In the second chapter of this dissertation, we tackled the problem of the relative lack of robustness observed when working memory was solely supported by N-methyl-D-aspartate-receptor-mediated recurrent excitation. This problem is created when the network suffers the influence of external perturbations, such has noise or distractors, or internal heterogeneity properties. In order to address this issue, we explored the variety of known biophysical mechanisms present in the PFC to find possible candidates that may counteract the disruptive effects of these perturbations in the working memory trace. The main requirements were to operate at slow time scales and to be activity dependent. We realized that depolarization-induced suppression of inhibition, calcium-dependent nonspecific cationic current and short-term facilitation matched these criteria. When included in the network model, these three slow mechanisms conferred stability to the memory trace but at the expense of harder transitions between memory and resting states. The trade-off between robustness and flexibility became the major proposition in this work and we postulated that it could be adjusted by the neural regulatory pathways according to the behavioral task demands. We hope that these model observations and analysis may be tested by experimental investigators in order to validate their importance in working memory.

The implications of the presence of these slow processes in PFC circuits may not be relevant only for working memory. As shown for DSI and I_{CAN}, these mechanisms have a slow time course of

activation. Could this property be a neural substrate for other cognitive functions? Decision-making requires slow accumulation of information over time, which can be encoded by slow ramping of activity in a cortical circuit (Wang 2002; Wang 2008). In theory, DSI, STF or I_{CAN} would allow such ramping to be extended for the longer periods required to reach decisions. While our results only provide an intuition regarding this subject, it would be worth exploring in future research.

The project described in the third and fourth chapter resulted from a back-and-forth collaboration with experimental investigators. They previously published a thorough study describing the sequential steps in one of the intracellular signaling pathway that controls pyramidal excitability. The activation of the catecholamine receptors, α2A-adrenoceptors, resulted in the improvement of working memory function. They demonstrated that a key intermediate step in this cascade is the reduction of H-current activity, which seemingly lead to a decrease in the neurons excitability. Inspired by this study, we built a single cell and network models designed to simulate their findings. However, our modeling research suggested that there were still some missing components in our collaborators description - but did not refute the conclusions of their work. The main disagreement was that I_H alone could not account for the decrease in firing activity seen in recordings. In order to explain those results, we suggested two alternative hypotheses that successfully account for their observations.

This work contributes to shown the growing importance of the

computational and theoretical approaches to the understanding of biological processes and, more specifically, cognitive functions. The implementation of biophysically realistic models helps unravel neural mechanisms that are unreachable by laboratory procedures. Moreover, computational simulations allow a very large number of conditions to be tested in a short amount of time; something that would be very cumbersome to achieve otherwise. Nevertheless, it is crucial to define models constrained by biological data. The testable predictions proposed by the study of this type of models have a higher probability to be accepted for scrutiny by experimentalists.

Most of the findings put forth in this dissertation could be tested experimentally by a combination of methodologies, including electrophysiology, pharmacology, anatomy and microscopy. If anything, this work illustrates the importance of studying neural mechanisms by cross-examining distinct levels of abstraction; from molecules to circuits to behavior; from neurons to networks.

Bibliography

Abbott, L. F. and W. G. Regehr (2004). Synaptic computation. *Nature 431*, 796–803.

Amari, S.-i. (1977). Dynamics of pattern formation in lateral-inhibition type neural fields. *Biol Cybern 27*, 77–87.

Amit, D. J. (1995). The hebbian paradigm reintegrated: Local reverberations as internal representations. *Behav Brain Sci 18*, 617–626.

Amit, D. J. and N. Brunel (1997). Model of global spontaneous activity and local structured activity during delay periods in the cerebral cortex. *Cereb Cortex 7*, 237–252.

Amit, D. J., N. Brunel, and M. V. Tsodyks (1994). Correlations of cortical hebbian reverberations: theory versus experiment. *J Neurosci 14*, 6435–6445.

Angelo, K., M. London, S. R. Christensen, and M. Hausser (2007). Local and global effects of ih distribution in dendrites of mammalian neurons. *J Neurosci 27*, 8643–8653.

Aponte, Y., C.-C. Lien, E. Reisinger, and P. Jonas (2006). Hyperpolarization-activated cation channels in fast-spiking interneurons of rat hippocampus. *J Physiol 574*, 229–243.

Araya, R., J. Jiang, K. B. Eisenthal, and R. Yuste (2006). The spine neck filters membrane potentials. *Proc Natl Acad Sci U S A 103*, 17961–17966.

Arellano, J. I., R. Benavides-Piccione, J. DeFelipe, and R. Yuste (2007). Ultrastructure of dendritic spines: Correlation between synaptic and spine morphologies. *Front Neurosci 1*, 131–143.

Arnsten, A. F., C. D. Paspalas, N. J. Gamo, Y. Yang, and M. Wang (2010). Dynamic network connectivity: A new form of neuroplasticity. *Trends Cogn Sci 14*, 365–375.

Arnsten, A. F. T., J. X. Cai, B. L. Murphy, and P. S. Goldman-Rakic (1994). Dopamine d1 receptor mechanisms in the cognitive performance of young adult and aged monkeys. *Psychopharmacology (Berl) 116*, 143–151.

Baeg, E., Y. Kim, K. Huh, I. Mook-Jung, H. Kim, and M. Jung (2003). Dynamics of population code for working memory in the prefrontal cortex. *Neuron 40*, 177–188.

Barak, O., D. Sussillo, R. Romo, M. Tsodyks, and L. Abbott (2013). From fixed points to chaos: Three models of delayed discrimination. *Prog Neurobiol 103*, 214–222.

Batuev, A. S., A. A. Pirogov, and A. A. Orlov (1979). Unit activity of the prefrontal cortex during delayed alternation performance in monkey. *Acta Physiol Acad Sci Hung 53*, 345–353.

Ben-Yishai, R., R. L. Bar-Or, and H. Sompolinsky (1995). Theory of orientation tuning in visual cortex. *Proc Natl Acad Sci U S A 92*, 3844–3848.

Berger, T., M. E. Larkum, and H.-R. Luscher (2001). High ih channel density in the distal apical dendrite of layer v pyramidal cells increases bidirectional attenuation of EPSPs. *J Neurophysiol 85*, 855–868.

Biel, M., C. Wahl-Schott, S. Michalakis, and X. Zong (2009). Hyperpolarization-activated cation channels: From genes to function. *Physiol Rev 89*, 847–885.

Birnbaum, S. G., P. X. Yuan, M. Wang, S. Vijayraghavan, A. K. Bloom, D. J. Davis, K. T. Gobeske, J. D. Sweatt, H. K. Manji, and A. F. T. Arnsten (2004). Protein kinase c overactivity impairs prefrontal cortical regulation of working memory. *Science 306*, 882–884.

Bloodgood, B. L. and B. L. Sabatini (2005). Neuronal activity regulates diffusion across the neck of dendritic spines. *Science 310*, 866–869.

Brozoski, T. J., R. M. Brown, H. E. Rosvold, and P. S. Goldman (1979). Cognitive deficit caused by regional depletion of dopamine in prefrontal cortex of rhesus monkey. *Science 205*, 929–932.

Brunel, N. and X.-J. Wang (2001). Effects of neuromodulation in a cortical network model of object working memory dominated by recurrent inhibition. *J Comput Neurosci 11*, 63–85.

Bush, P. C. and T. J. Sejnowski (1993). Reduced compartmental models of neocortical pyramidal cells. *J Neurosci Methods 46*, 159–166.

Bush, P. C. and T. J. Sejnowski (1994). Effects of inhibition and dendritic saturation in simulated neocortical pyramidal cells. *J Neurophysiol 71*, 2183 –2193.

Camperi, M. and X.-J. Wang (1998). A model of visuospatial working memory in prefrontal cortex: Recurrent network and cellular bistability. *J Comput Neurosci 5*, 383–405.

Carandini, M. (2012). From circuits to behavior: a bridge too far? *Nat Neurosci 15*, 507–509.

Carnevale, N. and M. Hines (2006). *The NEURON Book*. Cambridge (UK): Cambridge University Press.

Carter, E. and X.-J. Wang (2007). Cannabinoid-mediated disinhibition and working memory: Dynamical interplay of multiple feedback mechanisms in a continuous attractor model of prefrontal cortex. *Cereb Cortex 17*, i16–26.

Chafee, M. V. and P. S. Goldman-Rakic (1998). Matching patterns of activity in primate prefrontal area 8a and parietal area 7ip neu-

rons during a spatial working MemoryTask. *J Neurophysiol 79*, 2919 –2940.

Chen, S., J. Wang, and S. A. Siegelbaum (2001). Properties of hyperpolarization-activated pacemaker current defined by coassembly of HCN1 and HCN2 subunits and basal modulation by cyclic nucleotide. *J Gen Physiol 117*, 491–504.

Clapham, D. E. (1998). Not so funny anymore: Pacing channels are cloned. *Neuron 21*, 5–7.

Compte, A., N. Brunel, P. S. Goldman-Rakic, and X.-J. Wang (2000). Synaptic mechanisms and network dynamics underlying spatial working memory in a cortical network model. *Cereb Cortex 10*, 910–923.

Compte, A., M. V. Sanchez-Vives, D. A. McCormick, and X.-J. Wang (2003). Cellular and network mechanisms of slow oscillatory activity (<1 hz) and wave propagations in a cortical network model. *J Neurophysiol 89*, 2707–2725.

Constantinidis, C. and P. S. Goldman-Rakic (2002). Correlated discharges among putative pyramidal neurons and interneurons in the primate prefrontal cortex. *J Neurophysiol 88*, 3487–3497.

Constantinidis, C. and X.-J. Wang (2004). A neural circuit basis for spatial working memory. *Neuroscientist 10*, 553–565.

Contreras, D., I. Timofeev, and M. Steriade (1996). Mechanisms of long-lasting hyperpolarizations underlying slow sleep oscillations in cat corticothalamic networks. *J Physiol 494*, 251–264.

Cooper, E. and L. Jan (2003). M-channels: Neurological diseases, neuromodulation, and drug development. *Arch Neurol 60*, 496–500.

Cowan, R. L. and C. J. Wilson (1994). Spontaneous firing patterns and axonal projections of single corticostriatal neurons in the rat medial agranular cortex. *J Neurophysiol 71*, 17–32.

Delmas, P. and D. A. Brown (2005). Pathways modulating neural KCNQ/M (kv7) potassium channels. *Nat Rev Neurosci 6*, 850–862.

Destexhe, A., D. Contreras, and M. Steriade (1999). Spatiotemporal analysis of local field potentials and unit discharges in cat cerebral cortex during natural wake and sleep states. *J Neurosci 19*, 4595–4608.

DiFrancesco, D. (1993). Pacemaker mechanisms in cardiac tissue. *Annu Rev Physiol 55*, 455–472.

Durstewitz, D., M. Kelc, and O. Gunturkun (1999). A neurocomputational theory of the dopaminergic modulation of working memory functions. *J Neurosci 19*, 2807–2822.

Durstewitz, D. and J. K. Seamans (2002). The computational role of dopamine d1 receptors in working memory. *Neural Netw 15*, 561–572.

Durstewitz, D. and J. K. Seamans (2008). The dual-state theory of prefrontal cortex dopamine function with relevance to catechol-o-methyltransferase genotypes and schizophrenia. *Biol Psychiatry 64*, 739–749.

Durstewitz, D., J. K. Seamans, and T. J. Sejnowski (2000a). Dopamine-mediated stabilization of delay-period activity in a network model of prefrontal cortex. *J Neurophysiol 83*, 1733–1750.

Durstewitz, D., J. K. Seamans, and T. J. Sejnowski (2000b). Neurocomputational models of working memory. *Nat Neurosci 3*, 1184–1191.

Dyhrfjeld-Johnsen, J., R. J. Morgan, C. Foldy, and I. Soltesz (2008). Upregulated h-current in hyperexcitable CA1 dendrites after febrile seizures. *Front Cell Neurosci 2*, 2.

Egorov, A. V., B. N. Hamam, E. Fransen, M. E. Hasselmo, and A. A. Alonso (2002). Graded persistent activity in entorhinal cortex neurons. *Nature 420*, 173–178.

Faber, E., P. Sedlak, M. Vidovic, and P. Sah (2006). Synaptic activation of transient receptor potential channels by metabotropic glutamate receptors in the lateral amygdala. *Neuroscience 137*, 781–794.

Fan, Y., D. Fricker, D. H. Brager, X. Chen, H.-C. Lu, R. A. Chitwood, and D. Johnston (2005). Activity-dependent decrease of excitability in rat hippocampal neurons through increases in ih. *Nat Neurosci 8*, 1542–1551.

Fisher, S. A., T. M. Fischer, and T. J. Carew (1997). Multiple overlapping processes underlying short-term synaptic enhancement. *Trends Neurosci 20*, 170–177.

Fransén, E., B. Tahvildari, A. V. Egorov, M. E. Hasselmo, and A. A. Alonso (2006). Mechanism of graded persistent cellular activity of entorhinal cortex layer v neurons. *Neuron 49*, 735–746.

Funahashi, S., C. J. Bruce, and P. S. Goldman-Rakic (1989). Mnemonic coding of visual space in the monkey's dorsolateral prefrontal cortex. *J Neurophysiol 61*, 331–349.

Fuster, J. M. (1997). *The prefrontal cortex: anatomy, physiology, and neuropsychology of the frontal lobe*. Philadelphia: Lippincott-Raven.

Fuster, J. M. and G. E. Alexander (1971). Neuron activity related to short-term memory. *Science 173*, 652–654.

George, M. S., L. F. Abbott, and S. A. Siegelbaum (2009). HCN hyperpolarization-activated cation channels inhibit EPSPs by interactions with M-type K^+ channels. *Nat Neurosci 12*, 577–584.

Georgopoulos, A. P., J. F. Kalaska, R. Caminiti, and J. T. Massey (1982). On the relations between the direction of two-dimensional

arm movements and cell discharge in primate motor cortex. *J Neurosci 2*, 1527–1537.

Gnadt, J. and R. Andersen (1988). Memory related motor planning activity in posterior parietal cortex of macaque. *Exp Brain Res 70*, 216–220.

Goldman, M. S. (2009). Memory without feedback in a neural network. *Neuron 61*, 621–634.

Goldman-Rakic, P. (1995). Cellular basis of working memory. *Neuron 14*, 477–485.

Goodman, D. F. M. and R. Brette (2009). The brian simulator. *Front Neurosci 3*, 192–197.

Gross, S. A., G. A. Guzmán, U. Wissenbach, S. E. Philipp, M. X. Zhu, D. Bruns, and A. Cavalié (2009). TRPC5 is a Ca^{2+}-activated channel functionally coupled to Ca^{2+}-selective ion channels. *J Biol Chem 284*, 34423–34432.

Grunditz, A., N. Holbro, L. Tian, Y. Zuo, and T. G. Oertner (2008). Spine neck plasticity controls postsynaptic calcium signals through electrical compartmentalization. *J Neurosci 28*, 13457 –13466.

Gutkin, B. S., C. R. Laing, C. L. Colby, C. C. Chow, and G. B. Ermentrout (2001). Turning on and off with excitation: The role of spike-timing asynchrony and synchrony in sustained neural activity. *J Comput Neurosci 11*, 121–134.

Haj-Dahmane, S. and R. Andrade (1998). Ionic mechanism of the slow afterdepolarization induced by muscarinic receptor activation in rat prefrontal cortex. *J Neurophysiol 80*, 1197–1210.

Hansel, D. and G. Mato (2013). Short-term plasticity explains irregular persistent activity in working memory tasks. *J Neurosci 33*, 133–149.

Hebb, D. O. (1949). *The organization of behavior: a neuropsychological theory*. New York: Wiley.

Hempel, C. M., K. H. Hartman, X.-J. Wang, G. G. Turrigiano, and S. B. Nelson (2000). Multiple forms of short-term plasticity at excitatory synapses in rat medial prefrontal cortex. *J Neurophysiol 83*, 3031–3041.

Henze, D. A., G. R. Gonzalez-Burgos, N. N. Urban, D. A. Lewis, and G. Barrionuevo (2000). Dopamine increases excitability of pyramidal neurons in primate prefrontal cortex. *J Neurophysiol 84*, 2799–2809.

Hubel, D. H. and T. N. Wiesel (1968). Receptive fields and functional architecture of monkey striate cortex. *J Physiol 195*, 215–243.

Hughes, D. I., K. A. Boyle, C. M. Kinnon, C. Bilsland, J. A. Quayle, R. J. Callister, and B. A. Graham (2013). HCN4 subunit expression in fast-spiking interneurons of the rat spinal cord and hippocampus. *Neuroscience 237*, 7–18.

Itskov, V., D. Hansel, and M. Tsodyks (2011). Short-term facilitation may stabilize parametric working memory trace. *Front Comput Neurosci 5*, 1–19.

Jahr, C. E. and C. F. Stevens (1990). Voltage dependence of NMDA-activated macroscopic conductances predicted by single-channel kinetics. *J Neurosci 10*, 3178–3182.

Jung, S., T. D. Jones, J. N. Lugo, A. H. Sheerin, J. W. Miller, R. D'Ambrosio, A. E. Anderson, and N. P. Poolos (2007). Progressive dendritic HCN channelopathy during epileptogenesis in the rat pilocarpine model of epilepsy. *J Neurosci 27*, 13012–13021.

Kalmbach, B. E., R. A. Chitwood, N. C. Dembrow, and D. Johnston (2013). Dendritic Generation of mGluR-Mediated Slow Afterdepolarization in Layer 5 Neurons of Prefrontal Cortex. *J Neurosci 33*, 13518–13532.

Katona, I., B. Sperlágh, A. Sik, A. Käfalvi, E. S. Vizi, K. Mackie, and T. F. Freund (1999). Presynaptically located CB1 cannabinoid receptors regulate GABA release from axon terminals of specific hippocampal interneurons. *J Neurosci 19*, 4544–4558.

Kawaguchi, Y. and Y. Kubota (1997). GABAergic cell subtypes and their synaptic connections in rat frontal cortex. *Cereb Cortex 7*, 476–486.

Kole, M. H. P., A. U. Brauer, and G. J. Stuart (2007). Inherited cortical HCN1 channel loss amplifies dendritic calcium electrogen-

esis and burst firing in a rat absence epilepsy model. *J Physiol 578*, 507–525.

Kritzer, M. F. and P. S. Goldman-Rakic (1995). Intrinsic circuit organization of the major layers and sublayers of the dorsolateral prefrontal cortex in the rhesus monkey. *J Comp Neuro 359*, 131–143.

Kulkarni, M., K. Zhang, and A. Kirkwood (2011). Single-cell persistent activity in anterodorsal thalamus. *Neurosci Lett 498*, 179–184.

Laing, C. R. and C. C. Chow (2001). Stationary bumps in networks of spiking neurons. *Neural Comput 13*, 1473–1494.

Levitt, J. B., D. A. Lewis, T. Yoshioka, and J. S. Lund (1993). Topography of pyramidal neuron intrinsic connections in macaque monkey prefrontal cortex (areas 9 and 46). *J Comp Neuro 338*, 360 – 376.

Lim, S. and M. S. Goldman (2013). Balanced cortical microcircuitry for maintaining information in working memory. *Nat Neurosci 16*, 1306–1314.

Liu, Y.-H. and X.-J. Wang (2001). Spike-frequency adaptation of a generalized leaky integrate-and-fire model neuron. *J Comput Neurosci 10*, 25–45.

Llano, I., N. Leresche, and A. Marty (1991). Calcium entry increases the sensitivity of cerebellar purkinje cells to applied GABA and decreases inhibitory synaptic currents. *Neuron 6*, 565–574.

Lorincz, A., T. Notomi, G. Tamas, R. Shigemoto, and Z. Nusser (2002). Polarized and compartment-dependent distribution of HCN1 in pyramidal cell dendrites. *Nat Neurosci 5*, 1185–1193.

Lupica, C. R., J. A. Bell, A. F. Hoffman, and P. L. Watson (2001). Contribution of the hyperpolarization-activated current (i h) to membrane potential and GABA release in hippocampal interneurons. *J Neurophysiol 86*, 261–268.

Luthi, A. and D. A. McCormick (1998). H-current: Properties of a neuronal and network pacemaker. *Neuron 21*, 9–12.

Maccaferri, G. and C. J. McBain (1996). The hyperpolarization-activated current (ih) and its contribution to pacemaker activity in rat CA1 hippocampal stratum oriens-alveus interneurones. *J Physiol 497*, 119–130.

Machens, C. K., R. Romo, and C. D. Brody (2005). Flexible control of mutual inhibition: A neural model of two-interval discrimination. *Science 307*, 1121–1124.

Machens, C. K., R. Romo, and C. D. Brody (2010). Functional, but not anatomical, separation of "what" and "when" in prefrontal cortex. *J Neurosci 30*, 350–360.

Magee, J. C. (1998). Dendritic hyperpolarization-activated currents modify the integrative properties of hippocampal CA1 pyramidal neurons. *J Neurosci 18*, 7613–7624.

Magee, J. C. (1999). Dendritic ih normalizes temporal summation in hippocampal CA1 neurons. *Nat Neurosci 2*, 508–514.

Major, G. and D. Tank (2004). Persistent neural activity: prevalence and mechanisms. *Curr Opin Neurobiol 14*, 675–684.

Marder, E. and J.-M. Goaillard (2006). Variability, compensation and homeostasis in neuron and network function. *Nat Rev Neurosci 7*, 563–574.

Marsicano, G. and B. Lutz (1999). Expression of the cannabinoid receptor CB1 in distinct neuronal subpopulations in the adult mouse forebrain. *Eur J Neurosci 11*, 4213–4225.

Matveev, V. and X.-J. Wang (2000). Differential short-term synaptic plasticity and transmission of complex spike trains: to depress or to facilitate? *Cereb Cortex 10*, 1143–1153.

Metherate, R. and J. H. Ashe (1993). Ionic flux contributions to neocortical slow waves and nucleus basalis- mediated activation: whole-cell recordings in vivo. *J Neurosci 13*, 5312–5323.

Migliore, M. and R. Migliore (2012). Know your current ih: Interaction with a shunting current explains the puzzling effects of its pharmacological or pathological modulations. *PLoS ONE 7*, e36867.

Miller, E. K. and J. D. Cohen (2001). An integrative theory of prefrontal cortex function. *Annu Rev Neurosci 24*, 167–202.

Miller, E. K., C. A. Erickson, and R. Desimone (1996). Neural mechanisms of visual working memory in prefrontal cortex of the macaque. *J Neurosci 16*, 5154–5167.

Miller, G. A. (1960). *Plans and the structure of behavior*. Holt, Rinehart and Winston, Inc., New York.

Miller, P., C. D. Brody, R. Romo, and X.-J. Wang (2003). A recurrent network model of somatosensory parametric working memory in the prefrontal cortex. *Cereb Cortex 13*, 1208–1218.

Miyashita, Y. and H. S. Chang (1988). Neuronal correlate of pictorial short-term memory in the primate temporal cortex. *Nature 331*, 68–70.

Mongillo, G., O. Barak, and M. Tsodyks (2008). Synaptic theory of working memory. *Science 319*, 1543–1546.

Muller, W. and J. A. Connor (1991). Dendritic spines as individual neuronal compartments for synaptic ca2+ responses. *Nature 354*, 73–76.

Murray, J. D., A. Anticevic, M. Gancsos, M. Ichinose, P. R. Corlett, J. H. Krystal, and X.-J. Wang (2012). Linking microcircuit dysfunction to cognitive impairment: Effects of disinhibition associated with schizophrenia in a cortical working memory model. *Cereb Cortex*, doi: 10.1093/cercor/bhs370.

Notomi, T. and R. Shigemoto (2004). Immunohistochemical localization of ih channel subunits, HCN1-4, in the rat brain. *J Comp Neurol 471*, 241–276.

Ohno-Shosaku, T., T. Maejima, and M. Kano (2001). Endogenous cannabinoids mediate retrograde signals from depolarized postsynaptic neurons to presynaptic terminals. *Neuron 29*, 729–738.

Palmer, L. M. and G. J. Stuart (2009). Membrane potential changes in dendritic spines during action potentials and synaptic input. *J Neurosci 29*, 6897–6903.

Pan, Z., T. Kao, Z. Horvath, J. Lemos, J.-Y. Sul, S. D. Cranstoun, V. Bennett, S. S. Scherer, and E. C. Cooper (2006). A common ankyrin-g-based mechanism retains KCNQ and NaV channels at electrically active domains of the axon. *J Neurosci 26*, 2599–2613.

Partridge, L. D. and C. F. Valenzuela (1999). Ca^{2+} store-dependent potentiation of Ca^{2+}-activated nonselective cation channels in rat hippocampal neurones in vitro. *J Physiol 521*, 617–627.

Paspalas, C. D., M. Wang, and A. F. T. Arnsten (2013). Constellation of HCN channels and cAMP regulating proteins in dendritic spines of the primate prefrontal cortex: Potential substrate for working memory deficits in schizophrenia. *Cereb Cortex 23*, 1643–1654.

Pinsky, P. F. and J. Rinzel (1994). Intrinsic and network rhythmogenesis in a reduced traub model for CA3 neurons. *J Comput Neurosci 1*, 39–60.

Pitler, T. A. and B. E. Alger (1992). Postsynaptic spike firing reduces synaptic GABAA responses in hippocampal pyramidal cells. *J Neurosci 12*, 4122–4132.

Poolos, N. P., M. Migliore, and D. Johnston (2002). Pharmacological upregulation of h-channels reduces the excitability of pyramidal neuron dendrites. *Nat Neurosci 5*, 767–774.

Ramos, B. P., L. Colgan, E. Nou, S. Ovadia, S. R. Wilson, and A. F. Arnsten (2005). The beta-1 adrenergic antagonist, betaxolol, improves working memory performance in rats and monkeys. *Biol Psychiatry 58*, 894–900.

Renart, A., P. Song, and X.-J. Wang (2003). Robust spatial working memory through homeostatic synaptic scaling in heterogeneous cortical networks. *Neuron 38*, 473–485.

Rolls, E. T., M. Loh, G. Deco, and G. Winterer (2008). Computational models of schizophrenia and dopamine modulation in the prefrontal cortex. *Nat Rev Neurosci 9*, 696–709.

Romo, R., C. D. Brody, A. Hernández, and L. Lemus (1999). Neuronal correlates of parametric working memory in the prefrontal cortex. *Nature 399*, 470–473.

Rosenkranz, J. A. and D. Johnston (2006). Dopaminergic regulation of neuronal excitability through modulation of ih in layer v entorhinal cortex. *J Neurosci 26*, 3229–3244.

Sabatini, B. L. and K. Svoboda (2000). Analysis of calcium channels in single spines using optical fluctuation analysis. *Nature 408*, 589–593.

Sanchez-Vives, M. V. and D. A. McCormick (2000). Cellular and network mechanisms of rhythmic recurrent activity in neocortex. *Nat Neurosci 3*, 1027–1034.

Santini, E. and J. T. Porter (2010). M-type potassium channels modulate the intrinsic excitability of infralimbic neurons and regulate fear expression and extinction. *J Neurosci 30*, 12379–12386.

Seamans, J. K., D. Durstewitz, B. R. Christie, C. F. Stevens, and T. J. Sejnowski (2001). Dopamine D1/D5 receptor modulation of excitatory synaptic inputs to layer v prefrontal cortex neurons. *Proc Natl Acad Sci U S A 98*, 301–306.

Seamans, J. K. and C. R. Yang (2004). The principal features and mechanisms of dopamine modulation in the prefrontal cortex. *Prog Neurobiol 74*, 1–58.

Shah, M. M., A. E. Anderson, V. Leung, X. Lin, and D. Johnston (2004). Seizure-induced plasticity of h channels in entorhinal cortical layer III pyramidal neurons. *Neuron 44*, 495–508.

Sidiropoulou, K., F.-M. Lu, M. A. Fowler, R. Xiao, C. Phillips, E. D. Ozkan, M. X. Zhu, F. J. White, and D. C. Cooper (2009). Dopamine modulates an mGluR5-mediated depolarization underlying prefrontal persistent activity. *Nat Neurosci 12*, 190–199.

Sjostrom, P. J., E. A. Rancz, A. Roth, and M. Hausser (2008). Dendritic excitability and synaptic plasticity. *Physiol Rev 88*, 769 –840.

Spruston, N. (2008). Pyramidal neurons: dendritic structure and synaptic integration. *Nat Rev Neurosci 9*, 206–221.

Steriade, M., F. Amzica, and D. Contreras (1996). Synchronization of fast (30-40 hz) spontaneous cortical rhythms during brain activation. *J Neurosci 16*, 392–417.

Steriade, M., A. Nunez, and F. Amzica (1993). A novel slow ($<$ 1 hz) oscillation of neocortical neurons in vivo: depolarizing and hyperpolarizing components. *J Neurosci 13*, 3252–3265.

Steriade, M., I. Timofeev, and F. Grenier (2001). Natural waking and sleep states: A view from inside neocortical neurons. *J Neurophysiol 85*, 1969–1985.

Stokes, M. G., M. Kusunoki, N. Sigala, H. Nili, D. Gaffan, and J. Duncan (2013). Dynamic coding for cognitive control in prefrontal cortex. *Neuron 78*, 364–375.

Strübing, C., G. Krapivinsky, L. Krapivinsky, and D. E. Clapham (2001). TRPC1 and TRPC5 form a novel cation channel in mammalian brain. *Neuron 29*, 645–655.

Szatmary, B. and E. M. Izhikevich (2010). Spike-timing theory of working memory. *PLoS Comput Biol 6*, e1000879.

Taxidis, J., K. Mizuseki, R. Mason, and M. R. Owen (2013). Influence of slow oscillation on hippocampal activity and ripples through cortico-hippocampal synaptic interactions, analyzed by a cortical-CA3-CA1 network model. *Front Comput Neurosci 7*, 3.

Tegnér, J., A. Compte, and X.-J. Wang (2002). The dynamical stability of reverberatory neural circuits. *Biol Cybern 87*, 471–481.

Timofeev, I., F. Grenier, and M. Steriade (2001). Disfacilitation and active inhibition in the neocortex during the natural sleep-wake cycle: An intracellular study. *Proc Natl Acad Sci U S A 98*, 1924–1929.

Trettel, J. and E. S. Levine (2003). Endocannabinoids mediate rapid retrograde signaling at interneuron pyramidal neuron synapses of the neocortex. *J Neurophysiol 89*, 2334–2338.

Tsodyks, M. and T. Sejnowski (1995). Associative memory and hippocampal place cells. *Int J Neural Syst 6*, 81–86.

Tsodyks, M. V. and H. Markram (1997). The neural code between neocortical pyramidal neurons depends on neurotransmitter release probability. *Proc Natl Acad Sci U S A 94*, 719–723.

Tuckwell, H. (1988). *Introduction to theoretical neurobiology*. Cambridge (UK): Cambridge University Press.

Ulens, C. and J. Tytgat (2001). Functional heteromerization of HCN1 and HCN2 pacemaker channels. *J Biol Chem 276*, 6069–6072.

Vaidya, S. P. and D. Johnston (2013). Temporal synchrony and gamma-to-theta power conversion in the dendrites of CA1 pyramidal neurons. *Nat Neurosci 16*, 1812–1820.

Vijayraghavan, S., M. Wang, S. G. Birnbaum, G. V. Williams, and A. F. T. Arnsten (2007). Inverted-u dopamine D1 receptor actions on prefrontal neurons engaged in working memory. *Nat Neurosci 10*, 376–384.

Wang, M., B. P. Ramos, C. D. Paspalas, Y. Shu, A. Simen, A. Duque, S. Vijayraghavan, A. Brennan, A. Dudley, E. Nou, J. A. Mazer, D. A. McCormick, and A. F. Arnsten (2007). alpha2A-Adrenoceptors strengthen working memory networks by inhibiting cAMP-HCN channel signaling in prefrontal cortex. *Cell 129*, 397–410.

Wang, M., Y. Yang, C.-J. Wang, N. J. Gamo, L. E. Jin, J. A. Mazer, J. H. Morrison, X.-J. Wang, and A. F. T. Arnsten (2013).

NMDA receptors subserve persistent neuronal firing during working memory in dorsolateral prefrontal cortex. *Neuron 77*, 736–749.

Wang, X.-J. (1999a). Fast burst firing and short-term synaptic plasticity: A model of neocortical chattering neurons. *Neuroscience 89*, 347–362.

Wang, X.-J. (1999b). Synaptic basis of cortical persistent activity: the importance of NMDA receptors to working memory. *J Neurosci 19*, 9587–9603.

Wang, X.-J. (2001). Synaptic reverberation underlying mnemonic persistent activity. *Trends Neurosci 24*, 455–463.

Wang, X.-J. (2002). Probabilistic decision making by slow reverberation in cortical circuits. *Neuron 36*, 955–968.

Wang, X.-J. (2008). Decision making in recurrent neuronal circuits. *Neuron 60*, 215–234.

Wang, X.-J. (2013). The prefrontal cortex as a quintessential "cognitive-type" neural circuit. In D. T. Stuss and R. T. Knight (Eds.), *Principles of Frontal Lobe Function*, pp. 226–248. Oxford University Press.

Wang, X.-J., J. Tegner, C. Constantinidis, and P. S. Goldman-Rakic (2004). Division of labor among distinct subtypes of inhibitory neurons in a cortical microcircuit of working memory. *Proc Natl Acad Sci U S A 101*, 1368 –1373.

Wang, Y., H. Markram, P. H. Goodman, T. K. Berger, J. Ma, and P. S. Goldman-Rakic (2006). Heterogeneity in the pyramidal network of the medial prefrontal cortex. *Nat Neurosci 9*, 534–542.

Wei, Z., X.-J. Wang, and D.-H. Wang (2012). From distributed resources to limited slots in multiple-item working memory: A spiking network model with normalization. *J Neurosci 32*, 11228–11240.

Williams, G. V. and P. S. Goldman-Rakic (1995). Modulation of memory fields by dopamine dl receptors in prefrontal cortex. *Nature 376*, 572–575.

Williams, S. R. and G. J. Stuart (2000). Site independence of EPSP time course is mediated by dendritic ih in neocortical pyramidal neurons. *J Neurophysiol 83*, 3177–3182.

Wilson, R. I., G. Kunos, and R. A. Nicoll (2001). Presynaptic specificity of endocannabinoid signaling in the hippocampus. *Neuron 31*, 453–462.

Wilson, R. I. and R. A. Nicoll (2001). Endogenous cannabinoids mediate retrograde signalling at hippocampal synapses. *Nature 410*, 588–592.

Yoshida, M. and M. E. Hasselmo (2009). Persistent firing supported by an intrinsic cellular mechanism in a component of the head direction system. *J Neurosci 29*, 4945–4952.

Yuste, R. and W. Denk (1995). Dendritic spines as basic functional units of neuronal integration. *Nature 375*, 682–684.

Zhang, K. (1996). Representation of spatial orientation by the intrinsic dynamics of the head-direction cell ensemble: a theory. *J Neurosci 16*, 2112–2126.

Zucker, R. S. (1989). Short-term synaptic plasticity. *Annu Rev Neurosci 12*, 13–31.

ITQB-UNL | Av. da República, 2780-157 Oeiras, Portugal
Tel (+351) 214 469 100
Fax (+351) 214 411 277

www.itqb.unl.pt